

國立交通大學

電子工程學系電子研究所

博士論文

氮化鎵異質結構場效電晶體

GaN-based Heterostructure Field-Effect Transistors

研究生：李建騏

指導教授：李建平博士

中華民國九十三年六月

# 氮化鎵異質結構場效電晶體

## GaN-based Heterostructure Field Effect Transistors

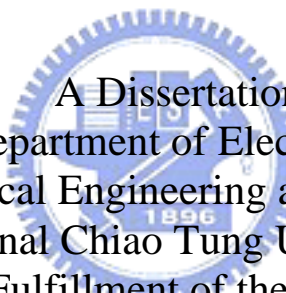
研究生：李建騏

Student: Chien-Chi Lee

指導教授：李建平博士

Advisor: Dr. Chien-Ping Lee

國立交通大學  
電子工程學系電子研究所  
博士論文



A Dissertation  
Submitted to Department of Electronics Engineering  
College of Electrical Engineering and Computer Science  
National Chiao Tung University  
in Partial Fulfillment of the Requirements  
for the degree of  
Doctor of Philosophy  
in  
Electronics Engineering  
June 2004  
Hsinchu, Taiwan, Republic of China

中華民國九十三年六月

# 氮化鎵異質結構場效電晶體

學生：李建騏

指導教授：李建平 博士

國立交通大學

電子工程系 電子研究所

## 摘要

本論文的研究目標為開發高性能氮化鎵場效電晶體。研究課題包括元件製程技術的開發及元件基本問題的探討。在元件製程技術的開發部份，我們成功的開發出製作氮化鎵場效電晶體所需的製程技術。這些製程技術包括電感耦合電漿蝕刻、電漿處理的低阻值歐姆接觸及窄T型閘極製作。在電感耦合電漿蝕刻部分，在適當的蝕刻條件下，我們可以製作出具有平坦及垂直側壁的絕緣平台。在元件歐姆接觸部分，我們利用不同條件的電漿處理得到低阻值的歐姆接觸 ( $\sim 1 \times 10^{-6} \Omega \cdot \text{cm}^2$ )。此外，我們也進一步證明其具有很好熱穩定性。在窄T型閘極製作部份，我們利用低加速電壓的電子束來製作窄T型閘。我們設計適當的圖形來有效地改善低加速電壓下的正向散射效應，最小的閘極長度可縮小至40 nm。

在元件基本問題的探討部分，我們研究元件的極化效應及熱效應。在元件的極化效應部分，我們做了廣泛的研究。我們設計幾種不同的元件結構，探討其表面型態、電子傳輸性質及元件特性，並實驗證明極化效應對電子傳輸性質及元件特性皆扮演了關鍵性的角色。對於undoped結構，極化效應可導致高濃度二維電子氣 ( $\sim 1 \times 10^{13} \text{ cm}^{-2}$ ) 在AlGaIn/GaN界面形成。因此AlGaIn/GaN元件具有很大的輸出電流。在元件的熱效應部分，我們探討在不同溫度下，不同的元件結構其通道中電子的傳輸性質及元件特性。我

們利用活化能的分析，成功的解釋調變摻雜結構的元件在不同的溫度下通道中電子濃度變化的原因。此外，我們也對不同結構的元件在不同的溫度下的特性作比較，並觀察到具調變摻雜結構的元件在不同的溫度下的特性都比undoped結構的元件好。我們成功的製作出具有大輸出電流 (undoped ~ 700 mA/mm; modulation-doped ~ 1000 mA/mm)、高崩潰電壓 (undoped ~ 100 V; modulation-doped ~ 53 V) 及高操作頻率 (undoped ~ 32 GHz; modulation-doped ~ 75 GHz) 的氮化鎵場效電晶體。這些優異的元件特性也充分的證明氮化鎵異質結構場效電晶體的確是非常好的微波高功率元件。



# GaN-based Heterostructure Field-Effect Transistors

Student: Chien-Chi Lee

Advisor: Dr. Chien-Ping Lee

Department of Electronics Engineering & Institute of Electronics

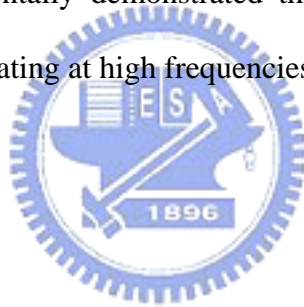
National Chiao Tung University

## Abstract

In this dissertation, we investigated AlGaIn/GaN heterostructure field-effect transistors (HFETs) to develop high-performance AlGaIn/GaN HFETs. The research topics cover the development of basic device processing technologies and fundamental device issues. We successfully developed the technologies required for the fabrication of high-performance AlGaIn/GaN HFETs, including the ICP etching of GaN, low resistance ohmic contacts to n-GaN and the narrow T-gate fabrication. A proper etching rate together with the vertical sidewall profile and smooth surface can be obtained in the ICP etching of GaN. Plasma-treated ohmic contacts exhibit low contact resistances ( $\sim 1 \times 10^{-6} \Omega \cdot \text{cm}^2$ ) and excellent thermal stability. A low accelerating voltage of 15 kV was used to perform the narrow T-gate fabrication. With the specially designed writing patterns, the forward scattering effects associated with a low accelerating voltage can be effectively improved. Narrow T-gates with the foot width of 40 nm were obtained.

In addition, we studied the polarization effect and the thermal effect of AlGaIn/GaN HFETs. The polarization effect plays a crucial role in both the electron transport properties and device characteristics of AlGaIn/GaN HFETs. The strong polarization effect in the undoped AlGaIn/GaN heterostructures leads to the formation of high-concentration 2DEG at

the AlGaN/GaN interface ( $\sim 1 \times 10^{13} \text{ cm}^{-2}$ ) and thus large output current can be obtained. The thermal effect is particularly important for the high-temperature application of devices. We found that in addition to the commonly known problem in the thermal conductivity of substrate, the device structure also plays a significant role in the temperature-dependent electron transport properties and the high-temperature performance of the device. Furthermore, we successfully fabricated high-performance submicron AlGaN/GaN HFETs. Both the undoped and the modulation-doped  $\text{Al}_{0.3}\text{Ga}_{0.7}\text{N}/\text{GaN}$  HFETs exhibited very high output currents (undoped  $\sim 700 \text{ mA/mm}$ ; modulation-doped  $\sim 1000 \text{ mA/mm}$ ), high breakdown voltages (undoped  $\sim 100 \text{ V}$ ; modulation-doped  $\sim 53 \text{ V}$ ) and high cut-off frequencies (undoped  $\sim 32 \text{ GHz}$ ; modulation-doped  $\sim 75 \text{ GHz}$ ). These excellent device characteristics obtained experimentally demonstrated that AlGaN/GaN HFETs are indeed excellent high power devices operating at high frequencies.



## Acknowledgements


首先，非常感謝我的指導教授-李建平博士。和老師討論問題是很有趣的，雖然有時讓人倍感壓力。此外，老師非常尊重每個學生的興趣，給予寬廣的學習空間並鼓勵大家積極研究創新。I like such style.

其次，非常感謝一起參與研究工作的夥伴。我的學弟-葉孟欣及石正楓，及提供磊晶試片的朋友們- 連威磊晶曾堅信博士及郭正達博士，以及工研院光電所祁錦雲主任、涂如欽博士及卓昌正博士。你們的貢獻很大。因為你們的熱心參與，我們的研究工作才能順利的來推動。

再來，非常感謝MBE實驗室的全體成員，包括已畢業的或在學的學長、學弟及學妹們。你們的貢獻也很大。你們是我在學習上的好夥伴及生活上歡樂的泉源。此外，交大奈米中心及國家奈米元件實驗室在實驗設備上的提供，更是不可或缺的要素。

最後，非常感謝家人的支持及鼓勵。你們是我的最終的依靠。

# Contents

<b>Abstract (Chinese)</b>	i
<b>Abstract (English)</b>	iii
<b>Acknowledgement</b>	v
<b>Contents</b>	vi
<b>Table captions</b>	x
<b>Figure captions</b>	xii
<b>Chapter 1 Introduction</b>	1
1-1 Overview and research motivation	1
1-2 Thesis organization	4
References	5
	
<b>Chapter 2 GaN-based materials and heterostructure field-effect transistors</b>	6
2-1 Fundamental material properties of GaN	6
2-2 Polarization effect	8
2-2-1 Crystal structure and polarity	8
2-2-2 Spontaneous and piezoelectric polarizations	9
2-2-3 Strain relaxation	13
2-2-4 Sheet charge concentration of 2DEG	14
2-3 AlGa <sub>N</sub> /Ga <sub>N</sub> HFETs	15
2-3-1 Important issues in the growth of AlGa <sub>N</sub> /Ga <sub>N</sub> heterostructures	16
2-3-2 Device operation principle	17
2-3-3 Device fabrication	17



References	19
<b>Chapter 3 Inductively coupled plasma etching of GaN</b>	<b>28</b>
3-1 Introduction	28
3-2 Experiment	29
3-3 Results and discussion	29
3-3-1 Ni mask fabrication	29
3-3-2 ICP etching	30
3-4 Conclusion	32
References	34
<b>Chapter 4 Low resistance Ohmic contact to n-GaN</b>	<b>43</b>
4-1 Introduction	43
4-2 Experiment	44
4-3 Results and discussion	45
4-3-1 Plasma treatments	45
4-3-2 Thermal stability issue	48
4-3-3 Forming gas ambient treatments	50
4-4 Conclusion	51
References	53
<b>Chapter 5 Narrow T-gate fabrication on GaN</b>	<b>64</b>
5-1 Introduction	64
5-2 Experiment	65
5-3 Results and discussion	66



5-3-1 Writing pattern design	66
5-3-2 40 nm narrow T-gate fabrication	66
5-4 Conclusion	69
References	70
<b>Chapter 6 Polarization effect in AlGaIn/GaN HFETs</b>	<b>75</b>
6-1 Introduction	75
6-2 Experiment	76
6-3 Results and discussion	78
6-3-1 Surface morphology	78
6-3-2 Electron transport properties	79
6-3-3 Device characteristics	84
6-4 Conclusion	88
References	90
<b>Chapter 7 Thermal effect of AlGaIn/GaN HFETs</b>	<b>107</b>
7-1 Introduction	107
7-2 Experiment	108
7-3 Results and discussion	110
7-3-1 Electron transport properties	110
7-3-2 Device high-temperature performance	113
7-4 Conclusion	118
References	120
<b>Chapter 8 Conclusion and proposed future work</b>	<b>130</b>



8-1 Conclusion	130
8-2 Proposed future work	131
References	133
<b>Vita</b>	136
<b>Publication list</b>	137



## Table captions

### Chapter 2

Table 2-1 Fundamental material properties of several important semiconductors [1].

Table 2-2 Structural properties of GaN-based materials, sapphire and SiC substrates.

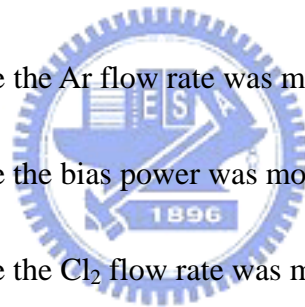
Table 2-3 Spontaneous polarization, piezoelectric and dielectric constants of AlN, GaN and InN [5].

### Chapter 3

Table 3-1 Etching condition where the Ar flow rate was modulated.

Table 3-2 Etching condition where the bias power was modulated.

Table 3-2 Etching condition where the Cl<sub>2</sub> flow rate was modulated.



### Chapter 4

Table 4-1 Etching conditions and TLM data.

Table 4-2 The conditions of the plasma treatment.

### Chapter 8

Table 8-1 A comparison on the device performance of AlGaIn/GaN HFETs on sapphire substrates.

Table 8-2 A comparison on the device performance of AlGaIn/GaN HFETs on SiC substrates.



## Figure captions

### Chapter 2

Fig. 2-1 Schematic diagrams of the crystal structure and the polarity of the Ga-face and N-face GaN crystals [5].

Fig. 2-2 Polarization-induced sheet charge and directions of the spontaneous and piezoelectric polarization in the Ga-face and N-face strained and relaxed AlGa<sub>x</sub>N/GaN heterostructures [5].

Fig. 2-3 Critical thickness of AlGa<sub>x</sub>N grown on relaxed GaN calculated using the models of Matthews and Blakeslee or Fischer *et al.* as a function of Al composition. AlGa<sub>x</sub>N layers with different thickness and Al composition grown pseudomorphically on GaN by MOCVD and MBE are marked by black symbols. Partially relaxed AlGa<sub>x</sub>N layers (white symbols) are separated from the pseudomorphic heterostructures by a dash line [7].

Fig. 2-4 Calculated total polarization induced sheet charge for pseudomorphically grown AlGa<sub>x</sub>N/GaN heterostructures under different degree of relaxation and Al compositions [7].

Fig. 2-5 Calculated maximum sheet carrier concentration for pseudomorphic (dashed lines) and partially relaxed (solid lines) Ga-face AlGa<sub>x</sub>N/GaN heterostructures with a barrier thickness of 200 Å [7].

Fig. 2-6 The schematic diagram of typical AlGaIn/GaN heterostructure field-effect transistors.

Fig. 2-7 The process procedures for the fabrication of AlGaIn/GaN HFETs.

### Chapter 3

Fig. 3-1 Optical microscope (OM) images of the Ni metal masks. This is done after lift-off process was performed.

Fig. 3-2 Optical microscope (OM) images of the Ni metal mask, where the black parts represent the etched Ni mask and the outer transparent parts represent photoresists.

This is done by wet etching process.

Fig. 3-3 Etching rates under different Ar flow rates.

Fig. 3-4 SEM images of the sidewall profile after ICP etching was performed under different Ar flow rates.

Fig. 3-5 Etching rate under different bias powers.

Fig. 3-6 SEM images of the sidewall profile after ICP etching was performed under different bias power.

Fig. 3-7 Etching rate under different Cl<sub>2</sub> flow rate.

Fig. 3-8 SEM images of the sidewall profile after ICP etching was performed under different Cl<sub>2</sub> flow rates.

## Chapter 4

Fig. 4-1 Current-voltage characteristics of the as-deposited ohmic contacts treated with Ar plasma at different Ar flow rate.

Fig. 4-2 The dependence of contact resistance and specific contact resistance of the as-deposited ohmic contacts on Ar flow rate.

Fig. 4-3 Current-voltage characteristics of the alloyed ohmic contacts under different Ar flow rate.

Fig. 4-4 The dependence of contact resistance and specific contact resistance of the alloyed ohmic contacts on Ar flow rate.

Fig. 4-5 Current-voltage characteristics of the as-deposited ohmic contacts under different Ar treatment time.



Fig. 4-6 Current-voltage characteristics of the alloyed ohmic contacts under different Ar treatment time.

Fig. 4-7 The dependence of contact resistance and specific contact resistance of the alloyed ohmic contacts on Ar treatment time.

Fig. 4-8 Aging test results of contact resistance in  $N_2$  ambient for samples with  $Cl_2/Ar$  plasma treatment.

Fig. 4-9 Aging test results of specific contact resistance in  $N_2$  ambient for samples with  $Cl_2/Ar$  plasma treatment.



Fig. 4-10 Aging test results of specific contact resistance in  $N_2$  ambient for samples with Ar plasma treatment.

Fig. 4-11 Aging test results of specific contact resistance in air ambient.

Fig. 4-12 Current-voltage characteristics of the ohmic contacts annealed in forming gas ambient.

Fig. 4-13 A comparison of specific contact resistance of the ohmic contacts annealed in  $N_2$  gas and in forming gas ambient.

## Chapter 5

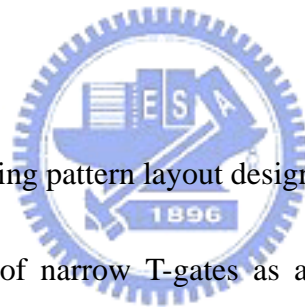


Fig. 5-1 The schematic of the writing pattern layout designed for narrow T-gate fabrication.

Fig. 5-2 The average footwidth of narrow T-gates as a function of the central dose. The average footwidth is 50 nm.

Fig. 5-3 The resist profile after development. A very good undercut profile and a narrow foot opening with dimensions of about 60 nm were obtained.

Fig. 5-4 A 40 nm narrow T-gate on a GaN substrate after metal deposition and lift-off.

## Chapter 6

Fig. 6-1 The schematic of undoped structure (sample No. 1), where Al composition is 0.17 and the top AlGaIn layer thickness is 18 nm.

Fig. 6-2 The schematic of undoped structure (sample No. 2), where Al composition is 0.17 and the top AlGa<sub>N</sub> layer thickness is 50 nm.

Fig. 6-3 The schematic of undoped structure (sample No. 3), where Al composition is 0.3 and the top AlGa<sub>N</sub> layer thickness is 28 nm.

Fig. 6-4 The schematic of modulation-doped structure (sample No. 4), where Al composition is 0.3 and the AlGa<sub>N</sub> layer consists of a 3 nm undoped AlGa<sub>N</sub> spacer, a 20 nm AlGa<sub>N</sub> with Si doping concentration of  $5 \times 10^{18} \text{ cm}^{-3}$  and a 5 nm undoped AlGa<sub>N</sub> cap layer.

Fig. 6-5 The surface morphology of undoped structure (sample No. 1), where Al composition is 0.17 and the top AlGa<sub>N</sub> layer thickness is 18 nm.

Fig. 6-6 The surface morphology of undoped structure (sample No. 2), where Al composition is 0.17 and the top AlGa<sub>N</sub> layer thickness is 50 nm.

Fig. 6-7 The surface morphology of undoped structure (sample No. 3), where Al composition is 0.3 and the top AlGa<sub>N</sub> layer thickness is 28 nm.

Fig. 6-8 The surface morphology of modulation-doped structure (sample No. 4), where Al composition is 0.3 and the total AlGa<sub>N</sub> layer thickness is 28 nm.

Fig. 6-9 A comparison on the electron concentration, where blank square (□) represents the sample with Al=0.17 (sample No. 1) and circle (●) represent the sample with Al=0.3 (sample No. 3).

Fig. 6-10 A comparison on the electron mobility, where blank square ( $\square$ ) represents the sample with Al=0.17 (sample No. 1) and circle ( $\bullet$ ) represent the sample with Al=0.3 (sample No. 3).

Fig. 6-11 A comparison on electron concentration, where blank square ( $\square$ ) represents the sample with AlGa<sub>N</sub> thickness of 18 nm (sample No. 1) and circle ( $\bullet$ ) represents the sample with AlGa<sub>N</sub> thickness of 50 nm (sample No. 2).

Fig. 6-12 A comparison on electron mobility, where blank square ( $\square$ ) represents the sample with AlGa<sub>N</sub> thickness of 18 nm (sample No. 1) and circle ( $\bullet$ ) represents the sample with AlGa<sub>N</sub> thickness of 50 nm (sample No. 2).

Fig. 6-13 A comparison on electron concentration, where blank circle ( $\square$ ) represents the undoped structure (sample No. 3) and circle ( $\bullet$ ) represents modulation-doped structure (sample No. 4).

Fig. 6-14 A comparison on electron mobility, where blank circle ( $\square$ ) represents the undoped structure (sample No. 3) and circle ( $\bullet$ ) represents modulation-doped structure (sample No. 4).

Fig. 6-15 Carrier profile of the undoped structure (sample No. 3) by C-V measurement. The dash line represents the location of AlGa<sub>N</sub>/Ga<sub>N</sub> interface.

Fig. 6-16 Carrier profile of the modulation-doped structure (sample No. 4) by C-V measurement. The dash line represents the locations of AlGa<sub>N</sub>/Ga<sub>N</sub> interface and

undoped AlGaN spacer/Si-doped AlGaN interface, respectively.

Fig. 6-17 The SEM images of an undoped  $\text{Al}_{0.3}\text{Ga}_{0.7}\text{N}/\text{GaN}$  HFET with a gate length of 0.15  $\mu\text{m}$  (top) and the enlarged picture of a 0.15  $\mu\text{m}$  long narrow T-gate.

Fig. 6-18 Current-voltage characteristics of the undoped  $\text{Al}_{0.3}\text{Ga}_{0.7}\text{N}/\text{GaN}$  HFET. The gate length is 0.15  $\mu\text{m}$  and the device width is 75  $\mu\text{m}$ .

Fig. 6-19 DC transfer characteristics of the undoped  $\text{Al}_{0.3}\text{Ga}_{0.7}\text{N}/\text{GaN}$  HFET. The gate length is 0.15  $\mu\text{m}$  and the device width is 75  $\mu\text{m}$ .

Fig. 6-20 Breakdown characteristics of the undoped  $\text{Al}_{0.3}\text{Ga}_{0.7}\text{N}/\text{GaN}$  HFET. Its gate length is 0.15  $\mu\text{m}$  and device width is 75  $\mu\text{m}$ .

Fig. 6-21 Forward Schottky I-V characteristics of the undoped  $\text{Al}_{0.3}\text{Ga}_{0.7}\text{N}/\text{GaN}$  HFET. Its gate length is 0.15  $\mu\text{m}$  and device width is 75  $\mu\text{m}$ .

Fig. 6-22 Small-signal characteristics of the undoped  $\text{Al}_{0.3}\text{Ga}_{0.7}\text{N}/\text{GaN}$  HFET. Its gate length is 0.15  $\mu\text{m}$  and device width is 75  $\mu\text{m}$ .

Fig. 6-23 Current-voltage characteristics of the modulation-doped  $\text{Al}_{0.3}\text{Ga}_{0.7}\text{N}/\text{GaN}$  HFET. The gate length is 0.15  $\mu\text{m}$  and the device width is 75  $\mu\text{m}$ .

Fig. 6-24 DC transfer characteristics of the modulation-doped  $\text{Al}_{0.3}\text{Ga}_{0.7}\text{N}/\text{GaN}$  HFET. The gate length is 0.15  $\mu\text{m}$  and the device width is 75  $\mu\text{m}$ .

Fig. 6-25 Breakdown characteristics of the modulation-doped  $\text{Al}_{0.3}\text{Ga}_{0.7}\text{N}/\text{GaN}$  HFET. Its gate length is 0.15  $\mu\text{m}$  and device width is 75  $\mu\text{m}$ .

Fig. 6-26 Forward Schottky I-V characteristics of the modulation-doped  $\text{Al}_{0.3}\text{Ga}_{0.7}\text{N}/\text{GaN}$  HFET. Its gate length is  $0.15\ \mu\text{m}$  and device width is  $75\ \mu\text{m}$ .

Fig. 6-27 Small-signal characteristics of the modulation-doped  $\text{Al}_{0.3}\text{Ga}_{0.7}\text{N}/\text{GaN}$  HFET. Its gate length is  $0.15\ \mu\text{m}$  and device width is  $75\ \mu\text{m}$ .

Fig. 6-28 The gate length dependence of the cut-off frequency for the undoped and modulation-doped  $\text{Al}_{0.3}\text{Ga}_{0.7}\text{N}/\text{GaN}$  HFETs.

## Chapter 7

Fig. 7-1 Temperature dependence of the electron concentration of the undoped and modulation-doped structures.

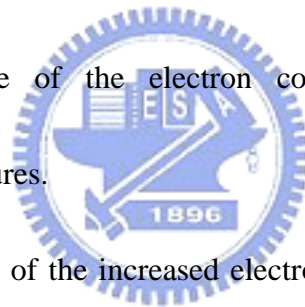


Fig. 7-2 Temperature dependence of the increased electron concentration due to the thermal activation process and the activation energy,  $E_d$ , of Si donors in  $\text{Al}_{0.3}\text{Ga}_{0.7}\text{N}$ .

Fig. 7-3 Temperature dependence of the electron mobility of the undoped and modulation-doped structures.

Fig. 7-4 Current-voltage characteristics of the undoped  $\text{Al}_{0.3}\text{Ga}_{0.7}\text{N}/\text{GaN}$  HFETs at room temperature and  $200^\circ\text{C}$ . ( $V_{\text{gs, top}} = 2\ \text{V}$  and step =  $-1\ \text{V}$ ).

Fig. 7-5 DC transfer characteristics of the undoped  $\text{Al}_{0.3}\text{Ga}_{0.7}\text{N}/\text{GaN}$  HFETs at drain bias  $V_{\text{ds}} = 5\ \text{V}$  under different temperatures.

Fig. 7-6 Forward Schottky gate I-V characteristics of undoped  $\text{Al}_{0.3}\text{Ga}_{0.7}\text{N}/\text{GaN}$  HFETs at

room temperature and 200°C.

Fig. 7-7 Current-voltage characteristics of the modulation-doped  $\text{Al}_{0.3}\text{Ga}_{0.7}\text{N}/\text{GaN}$  HFETs at room temperature and 200°C. ( $V_{\text{gs, top}} = 2 \text{ V}$  and step = -1 V).

Fig. 7-8 DC transfer characteristics of the modulation-doped  $\text{Al}_{0.3}\text{Ga}_{0.7}\text{N}/\text{GaN}$  HFETs at drain bias  $V_{\text{ds}} = 5 \text{ V}$  under different temperatures.

Fig. 7-9 Forward Schottky gate I-V characteristics of modulation-doped  $\text{Al}_{0.3}\text{Ga}_{0.7}\text{N}/\text{GaN}$  HFETs at room temperature and 200°C.

Fig. 7-10 A comparison on the temperature dependence of the maximum drain current ( $I_{\text{d, max}}$ ) of the undoped and modulation-doped  $\text{Al}_{0.3}\text{Ga}_{0.7}\text{N}/\text{GaN}$  HFETs.

Fig. 7-11 A comparison on the temperature dependence of the maximum extrinsic transconductance of the undoped and modulation-doped  $\text{Al}_{0.3}\text{Ga}_{0.7}\text{N}/\text{GaN}$  HFETs.

Fig. 7-12 A comparison on the temperature dependence of current gain cut-off frequency ( $f_T$ ) of the undoped and modulation-doped  $\text{Al}_{0.3}\text{Ga}_{0.7}\text{N}/\text{GaN}$  HFETs.

# Chapter 1

## Introduction

### 1-1 Overview and research motivation [1-4]

Gallium nitride has a colorful recent history. In the 1990s, Shuji Nakamura, then at Nichia Chemical Industries, used the GaN to fabricate the first green, blue, violet and white light-emitting diodes (LEDs) and the first blue-light semiconductor laser. This significant achievement turned Nakamura, now a professor of electrical engineering at the University of California at Santa Barbara, into a folk hero and Nichia into the world's largest manufacturer of LEDs. Today, blue LEDs are so ubiquitous that you probably see them every day, in handsets, traffic lights, colorful video billboard, children's toys, even flashlights. Nakamura's success did more than trigger a revolution in optoelectronics. It also helped direct attention and funding to work on high-power, high frequency GaN transistors.

With the rapid progress in the wireless communication, the future wireless network hopes to let people to tap into high-speed streams of data using their cell phones, personal digital assistants (PDAs) or some other pocket consoles to capture video or high-quality sound. Such amazing desire requires that cellular base-station amplifiers will deal with the huge data streams so that anyone can download full-motion video at any time anywhere. These present amplifiers using a silicon-based technology are already being pushed to their

limits due to the low efficiency of around 10 percent. The most power that goes into the transistors is transformed into heat. Thus powerful fans must continually blast this heat away from the amplifiers, which must also be outfitted with complex circuits.

GaN transistors, with the unique material properties, could double or triple the efficiency of base-station amplifiers. Thus a given area could be covered by fewer base stations or, more likely, be flooded with more data at much higher rates. Free from the powerful fans and correction circuits, it might even be possible to shrink an entire base station to the size of small refrigerator, which would not take up expensive space in a telephone company central office. Additionally, the characteristics of speed, high-power handling capability and heat resistance would suit the GaN transistors to countless other uses. Hybrid electric vehicles, for instance, depend on circuits that convert current from their batteries to an alternating current capable of running an electric motor. GaN transistors would be ideal for such application.

In the military applications, radar and satellite communication links, which operate at frequencies ranging from hundreds of megahertz to tens of gigahertz, often have high-power amplification requirements and would therefore benefit tremendously from GaN. Many of the transmitters of the radar systems and the satellite communication links still use traveling-wave tubes amplifiers (TWTAs), a World War II era technology. The reason is that no semiconductor widely available today can cope with the frequencies and power levels involved. GaN transistors, however, would work in many of these applications, conferring on



them the solid-state advantages of ruggedness and portability.

With so many potential uses in both commercial and military applications, GaN has become one of the most active and robust trusts in semiconductor research and development. Some dazzling results have been achieved over the years. The first AlGaIn/GaN high electron mobility transistors (HEMTs) were demonstrated by Khan *et al.* in 1994 [5]. By the year of 2001, the research groups at Cornell University and the University of California at Santa Barbara both fabricated GaN transistors capable of sustaining power densities of above 10 W/mm at frequencies of around 10 GHz. For comparison, ordinary Si-based transistors can efficiently amplify signals only up to 2-3 GHz. GaAs transistors can handle 10 GHz, but withstand a power density of less than 1W/mm at that frequency. SiGe devices can handle even higher frequencies, but, like GaAs, cannot withstand high power. SiC devices can also deliver very high power density of above 7 W/mm, but at frequencies not higher than 3.5 GHz.

In this work, we systematically investigated GaN heterostructure field-effect transistors (HFETs). The research topics include the development of basic device processing technologies and fundamental device issues. We successfully developed the technologies required for the fabrication of high-performance AlGaIn/GaN HFETs, including the ICP etching of GaN, low resistance Ohmic contacts to n-GaN and the narrow T-gate fabrication. In addition, we studied the polarization effect and the thermal effect of AlGaIn/GaN HFETs.

Furthermore, we successfully fabricated high-performance submicron AlGa<sub>0.3</sub>N/GaN HFETs. Both the undoped and the modulation-doped Al<sub>0.3</sub>Ga<sub>0.7</sub>N/GaN HFETs exhibited very high output currents, high breakdown voltages and high cut-off frequencies. These excellent device characteristics obtained experimentally demonstrated that AlGa<sub>0.3</sub>N/GaN HFETs are indeed excellent high power devices operating at high frequencies.

## 1-2 Thesis organization

In chapter 2, the fundamental material properties of GaN, and the AlGa<sub>0.3</sub>N/GaN heterostructures and HFETs are briefly reviewed. In chapter 3, the inductively couple plasma (ICP) etching of GaN for the mesa isolation of devices is reported. Chapter 4 and Chapter 5 cover the low resistance Ohmic contacts to GaN by various plasma treatments. In chapter 6, a simple narrow T-gate fabrication technology using a 15 KV acceleration voltage is given. Chapter 7 deals with the orientation effect of unpassivated AlGa<sub>0.3</sub>N/GaN HFETs. In chapter 8, a comprehensive investigation of the polarization effect on the AlGa<sub>0.3</sub>N/GaN heterostructures and HFETs is detailed. In chapter 9, a thorough study on the thermal effect of AlGa<sub>0.3</sub>N/GaN HFETs including the temperature-dependent electron transport properties and device high temperature performance is presented. Finally, a conclusion and the proposed future work for this study are given in chapter 10.

## References

[1] S. Keller, Y. F. Wu, G. Parish, N. Ziang, J. J. Xu, B. P. Keller, S. P. DenBaars and U. K.

Mishra, IEEE Trans. Electron Devices **48**, 552 (2001).

[2] L. F. Eastman and U. K. Mishra, IEEE spectrum, **May**, 28 (2002).

[3] U. K. Mishra, P. Parikh and Y. F. Wu, Proc. of the IEEE **90**, 1022 (2002).

[4] S. Nuttinck, E. Gebara, J. Laskar and M. Harris, IEEE microwave magazine, **March**, 80

(2002).

[5] M. Asif. Khan, J. N. Kuznia, D. T. Olson, W. J. Schaff, J. W. Burm, M. S. Shur, Appl. Phys.

Lett., **65**, 1121 (1994).



## Chapter 2

### GaN-based materials and heterostructure field-effect transistors

#### 2-1 Fundamental material properties of GaN

Table 2-1 shows a comparison on the fundamental material properties of several important semiconductors [1]. Compared to other commonly used semiconductor materials, GaN has the largest bandgap at room temperature,  $\sim 3.4$  eV. Such a wide bandgap means that much fewer intrinsic carriers are available than other semiconductor materials at room temperature or even higher temperatures, suggesting the excellent thermal stability. In addition, GaN has the highest critical breakdown field,  $\sim 3$  MV/cm. The reason is the strong bonding energy between Ga and nitrogen atoms. A high breakdown field is desirable since it means that a device made out of this material can withstand higher voltages over smaller dimensions. Thus GaN-based electronic devices can operate at much higher voltages than conventional Si, GaAs- and InP-based devices and have the ability to withstand high power levels. The electron transport properties play a crucial role in the device characteristics. The AlGaN/GaN heterostructures show a room temperature electron mobility of around  $1500$   $\text{cm}^2/\text{Vs}$ , which is lower than the traditional AlGaAs/InGaAs or InAlAs/InGaAs heterostructures. However, GaN has a very high electron saturation velocity of  $\sim 3 \times 10^7$  cm/s, suggesting the high-speed potential of GaN-based devices. In the thermal properties, GaN has

a comparable thermal conductivity of around 1.5 W/cm·K to Si, which is higher than the commonly used compound semiconductor materials. From the superior material properties of GaN, such as high breakdown field, high saturation velocity and wide bandgap, GaN-based electronic devices are indeed good candidates in the high-power, high-temperature and high-speed applications.

Table 2-2 lists the structural properties of GaN-based materials, sapphire and SiC substrates. GaN-based materials have the wurtzite crystal structure, which consists of two hexagonal closely packed (HCP) sublattices, group III and nitrogen atoms. The lattice parameters for GaN are 3.186 in  $a$  axis and 5.178 Å in  $c$  axis. Compared to GaN, the AlN has smaller lattice parameters, while the InN has larger lattice constants.

Up to now, the most widely used substrate materials are sapphire and SiC. The reason is that in the early stage there is no suitable substrate material with perfect lattice match to GaN available for the epitaxial growth of GaN-based materials. Currently, although the GaN substrate can be obtained, the available size now is still too small, as compared to the sapphire and SiC substrates.

The very large lattice mismatch (14.8%) and the difference in the thermal expansion coefficient between the GaN and sapphire substrate, however, cause huge challenges in the material growth of nitrides. Amano *et al.* proposed to grow a thin AlN nucleation layer at low temperatures and successfully obtained atomically smooth GaN layers in 1986 [2]. Later,

Nakamura *et al.* used a GaN nucleation layer grown at low temperatures and obtained the GaN layers with even higher electron mobility [3-4]. On the other hand, the SiC substrates have a much smaller lattice mismatch to GaN and a smaller difference in the thermal expansion coefficients with GaN, so it is much easier to grow GaN-based materials using the SiC substrates. However, the expensive price and the lack of substrates with larger dimensions limit the use of SiC substrates for practical applications. In contrast, the much cheaper price and the availability of substrates with larger sizes enable sapphire substrates to become a very popular substrate material for nitrides.

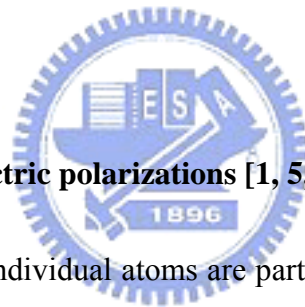


## **2-2 Polarization effect**

### **2-2-1 Crystal structure and polarity**

Nitride-based materials have the wurtzite crystal structure, which consists of two, group III and nitrogen, interpenetrating hexagonal closely packed (HCP) sublattices, as shown in Fig. 2-1. In general, noncentrosymmetric compound crystals exhibit two different sequences of the atom layering in the two opposing directions parallel to certain crystallographic axes, and thus crystallographic polarity along the axes can be observed. In the epitaxial growth of GaN and GaN-based heterostructures, the most common growth direction is normal to the  $\{0001\}$  basal plane, where the atoms are arranged in bilayers. It is noted that the  $[0001]$  direction is given by a vector pointing from a Ga atom to a nearest-neighbor nitrogen atom. As can be seen, if

the gallium atoms are on the top position of the bilayers (left side), it is called the Ga-face structure, corresponding to the  $[0001]$  polarity. On the other hand, if the nitrogen atoms are located on the surface of the  $\{0001\}$  bilayers (right side), it is the N-face structure, corresponding to the  $[000\bar{1}]$  polarity. Crystal structures with different crystallographic polarities exhibit different physical and chemical properties [5]. Usually, the layers grown by metalorganic chemical vapor deposition (MOCVD) are Ga-face structures. The layers grown by molecular beam epitaxy (MBE) are either Ga-face or N-face, depending on the nucleation layer used during material growth [6].



### **2-2-2 Spontaneous and piezoelectric polarizations [1, 5, 7]**

Inside the GaN crystal, the individual atoms are partially ionized, and the large Ga atom and small N atom are arranged somewhat irregularly with respect to each other because of the difference in atomic size. This combination of ionization and irregularity leads to a spontaneous electrical polarization within the GaN crystal. Due to the sensitive dependence of the spontaneous polarization on the structure parameters, the increasing nonideality of the crystal structure going from GaN to AlN further enhances the spontaneous polarization, as shown in Table 2-3. In particular, all the calculated spontaneous coefficients are negative [8]. Here, we consider the polarization along the  $[0001]$  direction. Thus the spontaneous polarization along the  $c$ -axis of the wurtzite crystal structure is

$$P_{SP} = P_{SP} \mathbf{z}. \quad (1)$$

In the case of AlGa<sub>N</sub>/Ga<sub>N</sub> heterostructures, the strain produced at the interface due to the lattice mismatch between the Ga<sub>N</sub> and AlGa<sub>N</sub> layers gives rise to an electrically charged region by the piezoelectric polarization. From a microscopic point of view, a strain parallel or perpendicular to the *c* axis produces an internal displacement of the metal sublattice with respect to the nitrogen ones. The measured polarization is due to the effect of the change of the lattice constants and the associated change in the length of the bond parallel to the *c* axis. The piezoelectric polarization can be calculated as follows.

$$P_{PE} = e_{33}\epsilon_z + e_{31}(\epsilon_x + \epsilon_y), \quad (2)$$

where  $e_{33}$  and  $e_{31}$  are the piezoelectric coefficients,  $\epsilon_z = (c-c_0)/c_0$  is the strain along the *c*-axis and the in-plane strain,  $\epsilon_x = \epsilon_y = (a-a_0)/a_0$ , is assumed to be isotropic.  $a_0$  and  $c_0$  are lattice parameters. The relation between the lattice constants of the hexagonal AlGa<sub>N</sub> system is

$$\frac{c - c_0}{c_0} = -2 \frac{C_{13}}{C_{33}} \frac{a - a_0}{a_0}, \quad (3)$$

where  $C_{13}$  and  $C_{33}$  are elastic constants. Using the Eqs (2) and (3), the amount of the piezoelectric polarization in the *c*-axis direction can be determined as

$$P_{PE} = 2 \frac{a - a_0}{a_0} (e_{31} - e_{33} \frac{C_{13}}{C_{33}}). \quad (4)$$

Since the term  $e_{31} - e_{33}(C_{13}/C_{33}) < 0$  for AlGa<sub>N</sub> over the whole Al composition, the piezoelectric polarization is negative for tensile and positive for compressive strained AlGa<sub>N</sub> layer.



Next, we determine the total polarization at the AlGa<sub>N</sub>/Ga<sub>N</sub> interface. The spontaneous polarization for Ga<sub>N</sub> and Al<sub>N</sub> was negative, meaning that for Ga-face heterostructures the spontaneous polarization points towards the substrate. Thus, the alignment in the direction of the piezoelectric polarization and the spontaneous polarization is parallel in the case of the tensile strained AlGa<sub>N</sub> layer, and is anti-parallel in the case of compressively strained cap AlGa<sub>N</sub> layer. On the other hand, if the crystal polarity changes from Ga-face to N-face material, the spontaneous and the piezoelectric polarization change the sign, as shown in Fig. 2-2. Furthermore, if the polarization-induced sheet charge is positive, free electrons will tend to compensate the polarization-induced sheet charge. Also, these free electrons will form a two-dimensional electron gas (2DEG) at the AlGa<sub>N</sub>/Ga<sub>N</sub> interface. In contrast, the negative polarization-induced sheet charge will cause the accumulation of holes at the interface.

For Ga(Al)-face AlGa<sub>N</sub>/Ga<sub>N</sub> heterostructures, the polarization-induced sheet charge is positive in the case of the tensile strained AlGa<sub>N</sub> [Fig. 2-2 (a)]. Even if the heterostructure is relaxed in case that the AlGa<sub>N</sub> thickness > 65 nm, the polarization-induced sheet charge is still positive because of the large difference in the spontaneous polarization of Ga<sub>N</sub> and Al<sub>N</sub> [Fig. 2-2 (b)]. The piezoelectric polarization due to the tensile strain at the interface will further enhance the difference in the total polarization between the AlGa<sub>N</sub> and Ga<sub>N</sub>, and thus the positive polarization induced sheet charge density and the 2DEG concentration increase accordingly. For N-face AlGa<sub>N</sub>/Ga<sub>N</sub> heterostructures, the spontaneous and piezoelectric

polarizations have opposite directions to the Ga-face heterostructures. It is therefore that the polarization induced sheet charge is negative and the accumulation of holes forms at the interface [Fig. 2-2 (d) and (e)]. From the above argument, it is therefore obvious that why a 2DEG can be observed by Hall effect measurement and the capacitance–voltage (C-V) profiling technique for the Ga(Al)-face AlGaN/GaN heterostructures.

Here, we consider the heterostructures where the AlGaN barriers are grown on the GaN buffer layers and are therefore under tensile strain. In this case, since the spontaneous and piezoelectric polarizations point in the same direction, the value of the total polarization is the sum of the spontaneous and piezoelectric polarizations.

$$P = P_{PE} + P_{SP}, \quad (5)$$

Associated with the polarization field is a polarization induced charge density given by

$$\rho_P = -\nabla \cdot \mathbf{P}, \quad (6)$$

At the interface of AlGaN/GaN heterostructures where AlGaN layer is the top layer, the polarization-induced sheet charge density is defined by

$$\begin{aligned} & \sigma(P_{SP} + P_{PE}) \\ &= P(\text{bottom}) - P(\text{top}) \\ &= [P_{SP}(\text{bottom}) + P_{PE}(\text{bottom})] - [P_{SP}(\text{top}) + P_{PE}(\text{top})] \\ &= [P_{SP}(\text{bottom}) - P_{SP}(\text{top})] + [P_{PE}(\text{bottom}) - P_{PE}(\text{top})] \\ &= \sigma(P_{SP}) + \sigma(P_{PE}). \end{aligned} \quad (7)$$

### 2-2-3 Strain relaxation [7]

As the AlGa<sub>N</sub> thickness is increased to a critical value, the critical thickness, we need to consider the strain relaxation effect on the piezoelectric and the total polarization. Calculation of the critical thickness of AlGa<sub>N</sub> grown on relaxed GaN based on the models proposed by Matthews and Blakeslee (M-B) and Fischer is shown in Fig. 2-3. For a typical barrier thickness of about 300 Å, the strain relaxation and thus the reduction in piezoelectric polarization has to be expected for Al composition of above 0.14 for the M-B model or 0.25 for the Fischer model. The experimental data, however, shows that the strain relaxation was observed for the critical thickness well above the calculated ones over a wide range of alloy composition. The strain relaxation for a 300 Å thick AlGa<sub>N</sub> barrier was experimentally observed at Al composition of about 0.38.

To analyze the reduction of piezoelectric polarization and the total polarization induced sheet charge due to strain relaxation, the degree of relaxation is defined by

$$r(x) = \frac{a(x) - a(\text{GaN})}{a_0(x) - a(\text{GaN})}, \quad (8)$$

and the measured degree of relaxation was approximately by

$$r(x) = \begin{cases} 0 & 0 \leq x < 0.38 \\ 3.5x - 1.33 & 0.38 \leq x \leq 0.67, \text{ for } d(\text{AlGaN}) \approx 30\text{nm}. \\ 1 & 0.67 \leq x < 1 \end{cases} \quad (9)$$

Thus, the piezoelectric polarization for partially relaxed AlGa<sub>N</sub> barriers can be determined

from the measured degree of relaxation by

$$P_{PE}(x) = 2\{r(x) - 1\} \left\{ \frac{a(x) - a(0)}{a(x)} \right\} \left\{ e_{31}(x) - e_{33}(x) \frac{C_{13}(x)}{C_{33}(x)} \right\}. \quad (10)$$

Fig. 2-4 shows the calculated total polarization induced sheet charge under different degrees of relaxation and Al composition. By taking the difference in the spontaneous polarization of GaN and AlGaN into account, the total polarization as well as the corresponding calculated sheet charge decreases with the increasing degree of relaxation.

#### 2-2-4 Sheet carrier concentration of 2DEG [5, 7]

With a basic understanding of the polarization induced sheet charge, we now wish to predict the sheet charge carrier concentration of a 2DEG and its dependence on the Al composition for strained AlGaN/GaN heterostructures. Free electrons tend to compensate the positive polarization induced sheet charge bound at the lower AlGaN/GaN interface for Ga(Al)-face heterostructures or at the upper GaN/AlGaN interface for N-face heterostructures. For undoped Ga-face AlGaN/GaN heterostructures, the sheet carrier concentration of 2DEG can be calculated by using the total polarization induced sheet charge and the following equation [9]:

$$n_S(x) = \frac{\sigma(x)}{e} - \left( \frac{\varepsilon_0 \varepsilon_S(x)}{d_{AlGaN} e^2} \right) [e\phi_B(x) + E_F(x) - \Delta E_C(x)], \quad (11)$$

where  $\varepsilon(x)$  is the relative dielectric constant of  $Al_xGa_{1-x}N$ ,  $d_{AlGaN}$  is the AlGaN barrier

thickness,  $e\phi_B(x)$  is the Schottky barrier of the gate contact on AlGaN,  $E_F(x)$  is the Fermi level respective to the GaN conduction-band-edge energy and  $\Delta E_C(x)$  is the conduction band offset at the AlGaN/GaN interface. For undoped AlGaN/GaN heterostructures and assuming that the background free carrier concentration can be neglected ( $< 10^{16} \text{ cm}^{-3}$ ), it is found from Eq. (11) that the value of the 2DEG sheet carrier concentration is dominated by the total polarization induced sheet charge, which can be controlled by the alloy composition of the AlGaN barrier.

Fig. 2-5 shows a detailed comparison of calculated and measured sheet carrier concentrations of Ga-face AlGaN/GaN heterostructures with AlGaN thickness of about 200 Å and Al composition up to 0.6. As can be seen, a good agreement between the calculated and experimentally determined highest sheet carrier concentration for the undoped and doped heterostructures can be observed. It is thus evident that the measured sheet carrier concentration for undoped structures are higher than the calculated sheet carrier concentration by only the piezoelectric polarization. Therefore, the spontaneous polarization is real and has to be taken into account in the determination of the total polarization sheet charge and 2DEG sheet carrier concentration. Moreover, the predicted sheet carrier concentration induced by the total polarization is more than twice as high as the sheet carrier concentration induced just by the piezoelectric effect.

### 2-3 AlGaN/GaN HFETs

### 2-3-1 Important issues in the growth of AlGa<sub>N</sub>/Ga<sub>N</sub> heterostructures

Fig. 2-6 shows the schematic diagram of typical AlGa<sub>N</sub>/Ga<sub>N</sub> heterostructure field-effect transistors. In general, a thin AlGa<sub>N</sub> barrier layer with thickness of around 20- 30 nm is pseudomorphically grown on the Ga<sub>N</sub> buffer layer. The Ga<sub>N</sub> buffer layer with both good crystal quality and high resistivity is highly desirable in the fabrication of AlGa<sub>N</sub>/Ga<sub>N</sub> HFETs. The crystal quality of the Ga<sub>N</sub> buffer layer is crucial to the electron transport properties of the AlGa<sub>N</sub>/Ga<sub>N</sub> heterostructures. Also, the high-resistivity buffer layer is a necessity for the microwave devices in order to effectively reduce the parasitic capacitances. However, the huge lattice mismatch between the Ga<sub>N</sub> buffer layer and the sapphire substrate causes the formation of very high-density dislocations ( $\sim 10^8$ - $10^9$  cm<sup>-2</sup>) in the epitaxial layers. In order to obtain high-quality Ga<sub>N</sub> buffer layers, the Ga<sub>N</sub> buffer layer is usually very thick, around 2-3  $\mu$ m. The thicker Ga<sub>N</sub> buffer layer can effectively reduce the defect density and improve the interface roughness of AlGa<sub>N</sub>/Ga<sub>N</sub> heterostructures, which in turn significantly improves the electron transport properties [10].

In addition, several problems arise in the growth of AlGa<sub>N</sub> [11]. It is not easy to obtain atomically smooth surfaces, especially for layers with high Al compositions. Also, the local variation in the alloy composition has been observed. As the Al mole fraction is above 0.2, the strain in the AlGa<sub>N</sub> due to the lattice mismatch between the AlGa<sub>N</sub> and Ga<sub>N</sub> may cause the formation of structural defects and transition into the island growth mode, and will also

influence the electrical properties of heterostructures.

### **2-3-2 Device operation principles**

Similar to the configurations of conventional field-effect transistors (FETs), the alloyed Ohmic contacts using Ti/Al-based contact metals act as the source and drain electrodes and the Schottky gates with either Pt/Au or Ni/Au are employed to control the input gate voltage signals. In the operation of FETs, a voltage signal applied to the gate electrode controls the current flow between the source and the drain electrodes. The small voltage changes on the gate are thus amplified into much larger changes in an external circuit.

Particularly, the strong spontaneous and piezoelectric polarization that exists naturally in the AlGa<sub>N</sub> layer leads to the formation of high-density 2DEG at the interface of the undoped AlGa<sub>N</sub>/Ga<sub>N</sub> heterostructures. It is therefore that the channel doping or the modulation doping, which is necessary for conventional heterostructure FETs, becomes unnecessary for the nitride HFETs.

### **2-3-3 Device fabrication**

Fig. 2-7 shows the process procedures developed for the fabrication of AlGa<sub>N</sub>/Ga<sub>N</sub> HFETs. The fabrication processes begin with the mesa isolation, followed by the Ohmic contact and the Schottky gate fabrication. Mesa isolation was performed with Cl<sub>2</sub>/Ar plasma

using an inductively couple plasma (ICP) system. Contact metals including Ti/Al/Ti/Au were then deposited to form the source and drain contact pads. With proper rapid thermal annealing in nitrogen ambient, low resistance Ohmic contacts were obtained. Pt or Ni is used as the Schottky metal because of the larger Schottky barrier height on nitrides. In particular, Ni is the preferred Schottky metal for the submicron T-gate fabrication due to its better adhesion to the underlying nitrides, although the Schottky barrier of Ni is slightly lower than Pt.





## References

- [1] L. F. Eastman and U. K. Mishra, IEEE spectrum, **May**, 28 (2002).
- [2] H. Amano, N. Sawaki, I. Akasaki and Y. Toyoda, Appl. Phys. Lett., **48**, 353 (1986).
- [3] S. Nakamura, Jpn. J. Appl. Phys., **30**, L1705 (1991).
- [4] S. Nakamura, T. Mukai and M. Senoh, J. Appl. Phys. **71**, 5543 (1992).
- [5] O. Ambacher, J. Smart, J. R. Shealy, N. G. Weimann, K. Chu, M. Murphy, W. J. Schaff, L. F. Eastman, R. Dimitrova, L. Wittmer, M. Stutzmann, W. Rieger and J. Hilsenback, J. Appl. Phys., **85**, 3222 (1999).
- [6] R. Dimitrova, M. Murphy, J. Smart, W. J. Schaff, J. R. Shealy, L. F. Eastman, O. Ambacher and M. Stutzmann, J. Appl. Phys., **87**, 3375 (2000).
- [7] O. Ambacher, B. Foutz, J. Smart, J. R. Shealy, N. G. Weimann, K. Chu, M. Murphy, A. J. Sierakowski, W. J. Schaff, L. F. Eastman, R. Dimitrova, A. Mitchell and M. Stutzmann, J. Appl. Phys., **87**, 334 (2000).
- [8] F. Bernardini, V. Fiorentini and D. Vanderbilt, Phys. Rev. B, **56**, R10024 (1997).
- [9] E. T. Yu, G. J. Sullivan, P. M. Asbeck, C. D. Wang, D. Qiao and S. S. Lau, Appl. Phys. Lett., **71**, 2794 (1997).
- [10] L. F. Eastman, V. Tilak, J. Smart, B. M. Green, E. M. Chumbes, R. Dimitrova, H. Kim, O. Ambacher, N. Weimann, T. Prunty, M. Murphy, W. J. Schaff and J. R. Shealy, IEEE Trans. Electron Devices, **48**, 479 (2001).

[11] S. Keller, G. Parish, P. T. Fini, S. Heikman, C. H. Chen, N. Zhang, S. P. DenBaars, U. K.

Mishra and Y. F. Wu, J. Appl. Phys., **86**, 5850 (1999).



Table 2-1 Fundamental material properties of several important semiconductors [1].

**● Where Gallium Nitride Outstrips Other Semiconductor Materials**

Semiconductor (commonly used compounds)			Gallium arsenide (AlGaAs/InGaAs)	Indium phosphide (InAlAs/InGaAs) <sup>a</sup>	Silicon carbide	Gallium nitride (AlGaN/GaN)
Characteristic	Unit	Silicon				
Bandgap	eV	1.1	1.42	1.35	3.26	3.49
Electron mobility at 300 K	cm <sup>2</sup> /Vs	1500	8500	5400	700	1000-2000
Saturated (peak) electron velocity	X10 <sup>7</sup> cm/s	1.0 (1.0)	1.3 (2.1)	1.0 (2.3)	2.0 (2.0)	1.3 (2.1)
Critical breakdown field	MV/cm	0.3	0.4	0.5	3.0	3.0
Thermal conductivity	W/cm•K	1.5	0.5	0.7	4.5	>1.5
Relative dielectric constant	ε <sub>r</sub>	11.8	12.8	12.5	10.0	9.0

<sup>a</sup> The compounds are loosely known as indium-based.



Table 2-2 Structural properties of GaN-based materials, sapphire and SiC substrates.

Crystalline properties	GaN	AlN	InN	Sapphire	6H-SiC
Lattice parameter(Å) a	3.186	3.1114	3.5446	4.758	3.081
Lattice parameter(Å) c	5.178	4.9792	5.7034	12.991	15.092
Lattice parameter(Å) c/a	1.6252	1.6003	1.6090	2.730	1.633
Lattice mismatch with sapphire	14.8%	12.5%	25.4%	-	11.5%
Lattice mismatch with SiC	3.3%	1.0%	14.0%	-11.5%	-
Lattice mismatch with GaN	-	-2.4%	10.6%	-14.8%	-3.3%
Thermal expansion coefficient. (×10 <sup>-6</sup> C <sup>-1</sup> ) a	5.59	4.2	5.7	7.5	4.2
Thermal expansion coefficient. (×10 <sup>-6</sup> C <sup>-1</sup> ) c	3.17	5.3	3.7	8.5	4.68

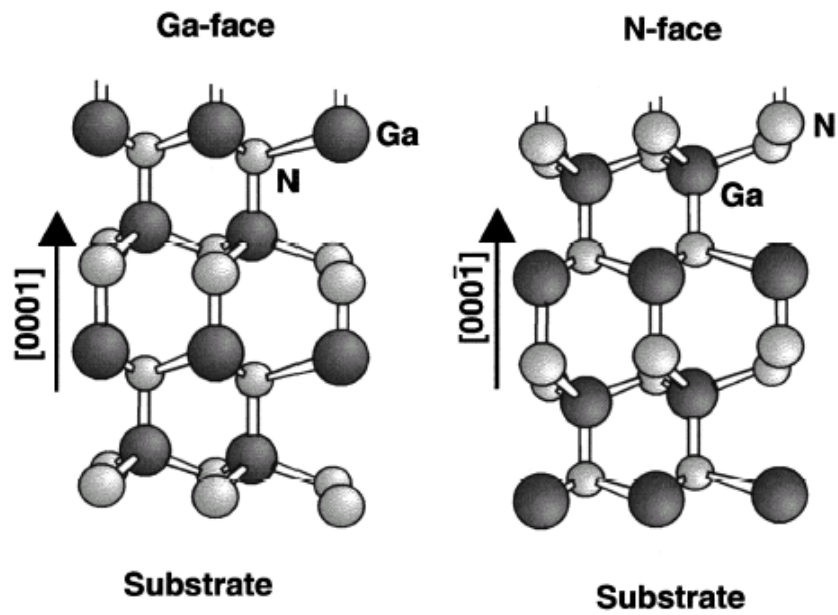


Fig. 2-1 Schematic diagrams of the crystal structure and the polarity of the Ga-face and N-face GaN crystals [5].



Table 2-3 Spontaneous polarization, piezoelectric and dielectric constants of AlN, GaN and InN [5].

wurtzite	AlN	GaN	InN
$P_{SP} [C/m^2]$	-0.081	-0.029	-0.032
$e_{33} [C/m^2]$	1.46 <sup>a</sup>	0.73 <sup>a</sup>	0.97 <sup>a</sup>
$e_{31} [C/m^2]$	1.55 <sup>b</sup>	1 <sup>c</sup>	
$e_{15} [C/m^2]$		0.65 <sup>d</sup>	
		0.44 <sup>e</sup>	
	-0.60 <sup>a</sup>	-0.49 <sup>a</sup>	-0.57 <sup>a</sup>
	-0.58 <sup>b</sup>	-0.36 <sup>c</sup>	
		0.33 <sup>d</sup>	
		-0.22 <sup>e</sup>	
	-0.48 <sup>b</sup>	-0.3 <sup>c</sup>	
		-0.33 <sup>d</sup>	
		-0.22 <sup>e</sup>	
$\epsilon_{11}$	9.0 <sup>b</sup>	9.5 <sup>f</sup>	
$\epsilon_{33}$	10.7 <sup>b</sup>	10.4 <sup>f</sup>	

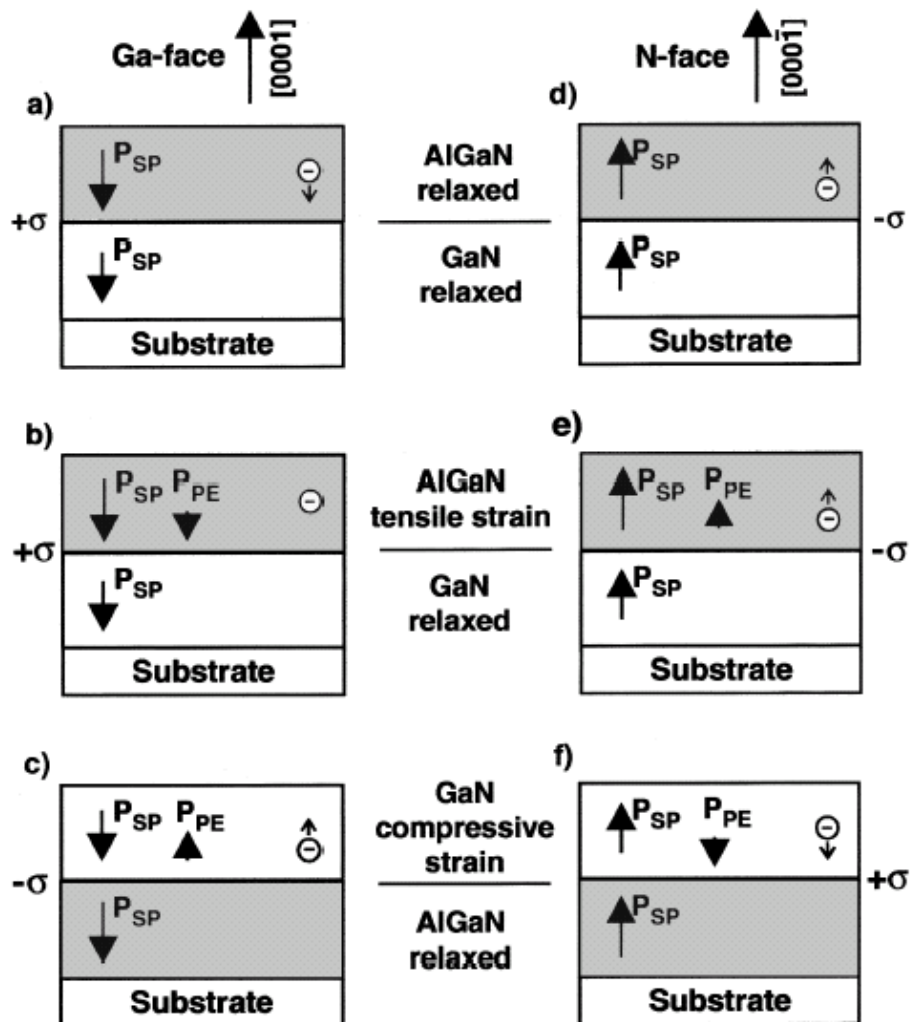


Fig. 2-2 Polarization-induced sheet charge and directions of the spontaneous and piezoelectric polarization in the Ga-face and N-face strained and relaxed AlGaN/GaN heterostructures [5].

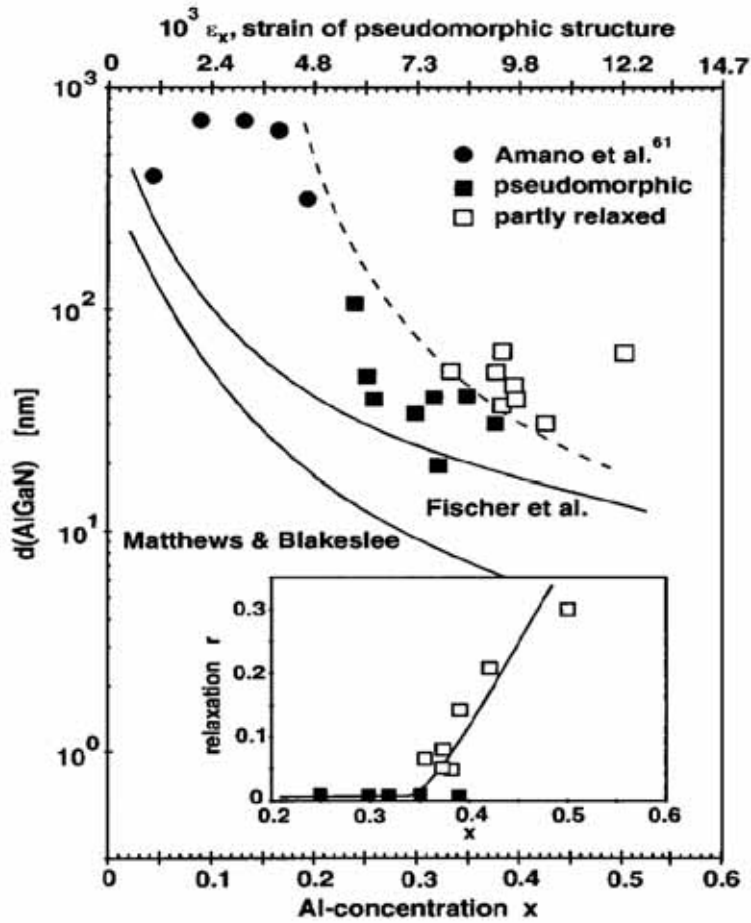


Fig. 2-3 Critical thickness of AlGa<sub>x</sub>N grown on relaxed GaN calculated using the models of Matthews and Blakeslee or Fischer *et al.* as a function of Al composition. AlGa<sub>x</sub>N layers with different thickness and Al composition grown pseudomorphically on GaN by MOCVD and MBE are marked by black symbols. Partially relaxed AlGa<sub>x</sub>N layers (white symbols) are separated from the pseudomorphic heterostructures by a dash line [7].

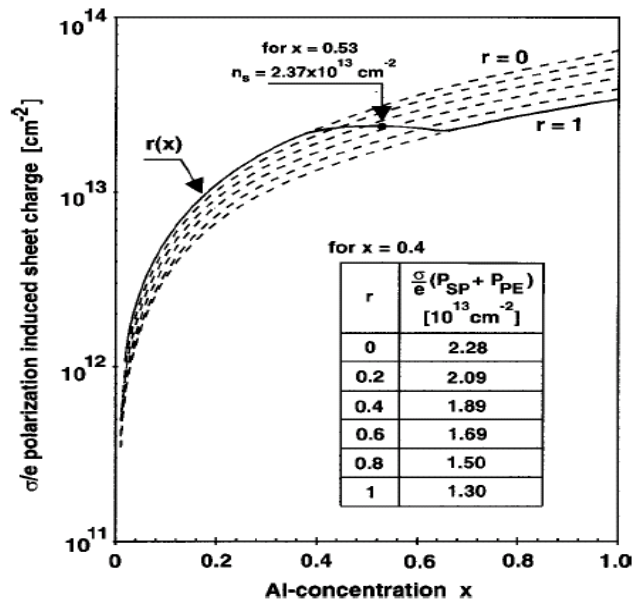


Fig. 2-4 Calculated total polarization induced sheet charge for pseudomorphically grown AlGa<sub>x</sub>N/GaN heterostructures under different degrees of relaxation and Al compositions [7].

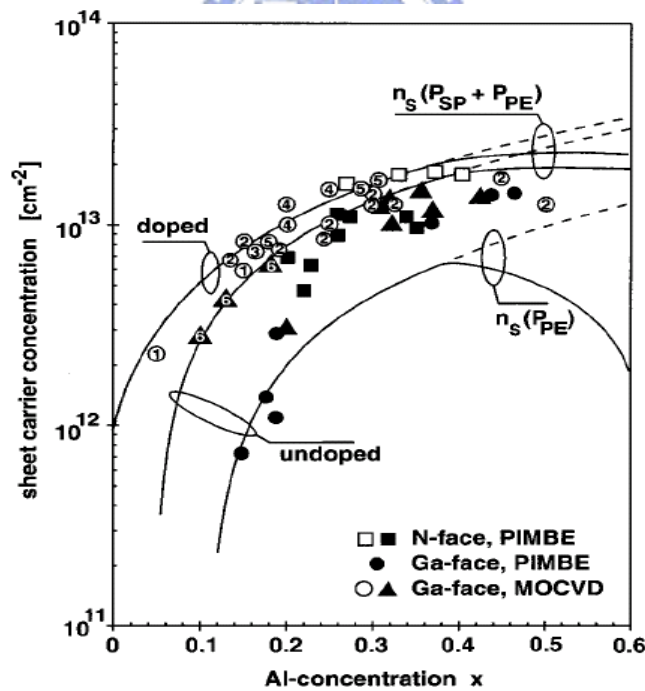


Fig. 2-5 Calculated maximum sheet carrier concentration for pseudomorphic (dashed lines) and partially relaxed (solid lines) Ga-face AlGa<sub>x</sub>N/GaN heterostructures with a barrier thickness of 200 Å [7].

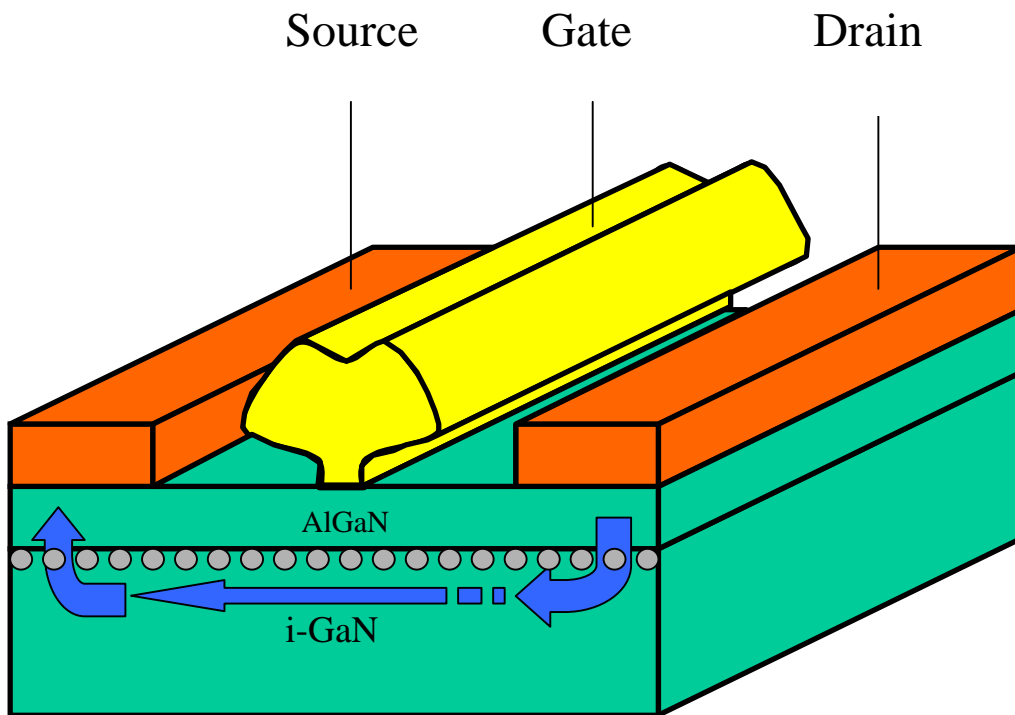
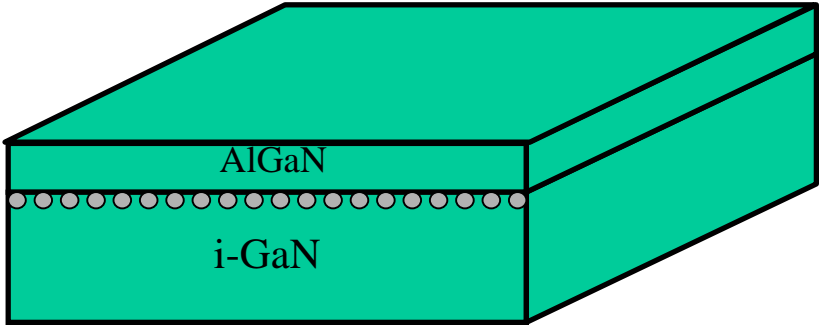


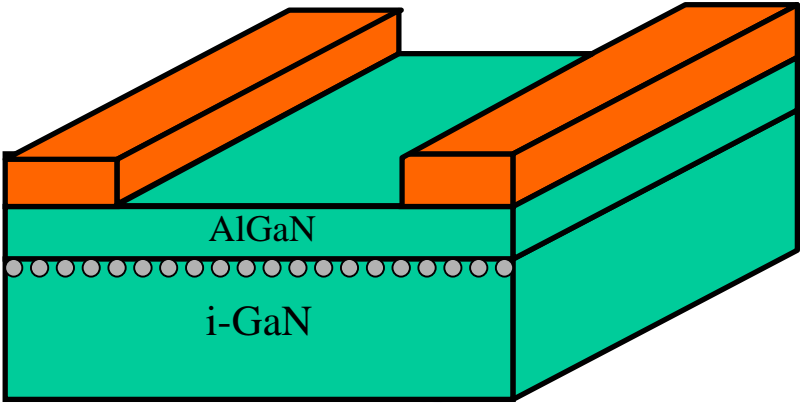
Fig. 2-6 The schematic diagram of typical AlGaN/GaN heterostructure field-effect transistor.



(a) Mesa isolation



(b) Ohmic contacts



(c) Schottky gate

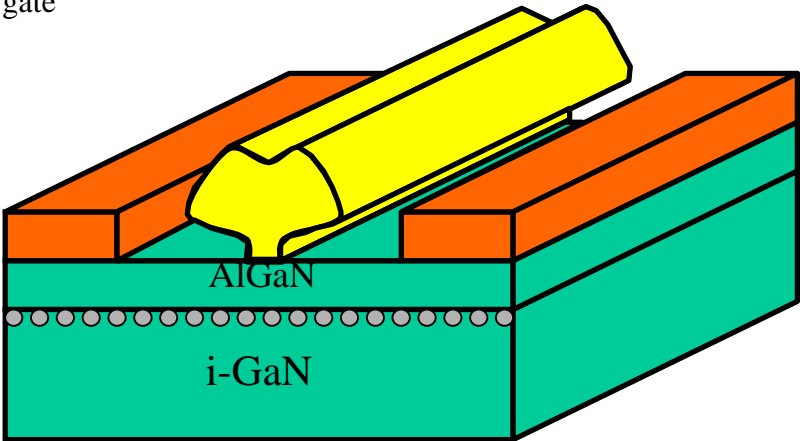


Fig. 2-7 The process procedures for the fabrication of AlGaN/GaN HFETs.

## Chapter 3

### Inductively Coupled Plasma Etching of GaN

#### 3-1 Introduction

Nitride-based electronic devices, such as heterostructure field-effect transistors (HFETs) and heterostructure bipolar transistors (HBTs), are potentially very useful for high-power and high-temperature applications. To realize these devices, device isolation is a necessity. Usually device isolation is done by mesa isolation or implantation isolation. Nitride-based materials, due to the inert chemical nature and the strong bonding energies, are not easy to be etched by conventional approaches including the wet chemical etching and the reactive-ion etching (RIE) [1]. In recent years, several new etching techniques such as high-density plasma (HDP) etching, chemically assisted ion beam etching (CAIBE), reactive ion beam etching (RIBE), low electron energy enhanced etching (LE4) and photoassisted dry etching were developed in an attempt to perform etching on the nitride-based materials. Compared with the conventional RIE, the HDP etcher has a much higher plasma density and the capability to more efficiently decouple the ion energy and ion density. Thus, the HDP etching, such as the inductively coupled plasma (ICP) etching, the electron cyclotron resonance (ECR) etching or the magnetron RIE (MRIE), has gradually become a popular approach. In this work, we systematically investigated the inductively coupled plasma etching of GaN. We studied the

dependence of the etching parameters, including the bias power, the Ar flow rate and the Cl<sub>2</sub> flow rate, on the etching rate and the etched sidewall profile of GaN. A proper etching rate together with the vertical sidewall profile and smooth surface developed in this work are applicable in the fabrication of GaN-based electronic devices.

### **3-2 Experiments**

The 2- $\mu\text{m}$ -thick undoped GaN films for this study were grown by metalorganic chemical vapor deposition (MOCVD) on c-plane sapphire substrates. After layer growth, mesa patterns for etching tests were defined by photolithography. Ni metal mask of around 2000 Å was then deposited using e-beam evaporation to form the etching mask. The samples were etched by Cl<sub>2</sub>/Ar plasma using an inductive coupled plasma (ICP) system under different etching conditions. After dry etching, the Ni mask was removed using the solution HNO<sub>3</sub>: H<sub>2</sub>O= 1:1. After etching, the etching depth, sidewall profile and the surface morphology were characterized.

### **3-3 Results and Discussion**

#### **3-3-1 Ni mask fabrication**

Usually, aggressive etching conditions were required in the dry etching of nitrides because of the inert chemical nature and strong bonding energies. Photoresist, Ni metal mask

and SiO<sub>2</sub> oxide mask can be used as the masking materials. In this work, we choose Ni metal as the etching mask due to its excellent masking ability.

Wet etching and lift-off process were employed to fabricate Ni masks. The mesa patterns in Ni formed by a lift-off process were shown to be much better than those by the wet etching process. Fig. 3-1 shows the Ni patterns after lift-off. Smooth edges and sharp profiles were obtained. In contrast, if the mesa patterns are defined by the wet chemical etching, rough edges will result, as shown in Fig. 3-2.

### 3-3-2 ICP etching

A couple of etching conditions were used to investigate the ICP etching of GaN, as summarized in Tables 3-1 to 3-3. The chemical species used here is Cl<sub>2</sub>. Ar is used to assist the etching process. Table 3-1 is for etching under different Ar flow rates, Table 3-2 is for etching under different bias powers and Table 3-3 is for etching under different Cl<sub>2</sub> flow rates.

Figure 3-3 shows the etching rates as a function of the Ar flow rate. The ICP power, the bias power, the chamber pressure and the Cl<sub>2</sub> flow rate used here were 300 W, 30 W, 15 mtorr and 50 sccm, respectively. The Ar flow rate ranged from 5 to 25 sccm. Etching rates of around 3300 Å/min. to 3400 Å/min. were obtained. A slight increase in the etching rate was observed in the cases where the Ar flow rate was increased from 5 to 15 sccm. With a higher Ar flow rate of above 15 sccm, the etching rate decreases. Fig. 3-4 shows the SEM images of the

sidewall profile and the surface morphology after etching. As a whole, the surface morphology of the etched surface is very smooth for all etching conditions used. For the samples treated with the Ar flow rate of 5 to 20 sccm, vertical sidewall profiles were obtained. The sample etched with an Ar flow rate of 25 sccm showed a slight undercut sidewall profile. Part of the samples showed slightly rough edge, such as Fig. 3-2 (b) and (d), which was attributed to the poor Ni mask edge profile.

In general, a higher Ar flow rate can enhance the physical ion bombardment, leading to more efficient bond breaking and the desorption of etched products. Thus the increase in the Ar flow rate can enhance the etching rate. As can be seen, a slight increase in the etching rate was obtained for samples with Ar flow rate below 15 sccm. On the other hand, a higher Ar flow rate may cause the decrease in the  $\text{Cl}_2/\text{Ar}$  flow rate ratio, leading to the decrease in the etching rate. In addition, a higher Ar flow rate can enhance the vertical etching, resulting in vertical sidewall profiles. The sidewall profiles obtained are vertical for most samples except the sample with Ar flow rate of 25 sccm.

Figure 3-5 shows the etching rate as a function of the bias power. An ICP power of 300 W, a chamber pressure of 15 mtorr, a  $\text{Cl}_2$  flow rate of 50 sccm and a Ar flow rate of 5 sccm were used. The etching rate increased with the bias power. When the bias power was reduced to 5 W, a very slow etching rate of around 100 Å/min was obtained. Figure 3-6 shows the SEM images of the etched sidewall profile. As a whole, vertical sidewall profile and smooth

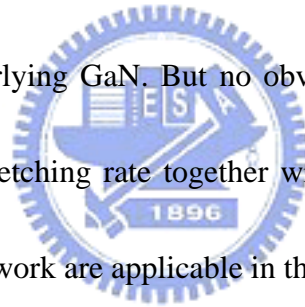
etched surface were obtained for most samples. The sample treated with a bias power of 20 W showed a slight undercut sidewall. The rough edge obtained in Fig. 3-4 (b) is due to the rough edge of the Ni metal mask. The rough etched surface shown in Fig. 3-4 (d) is mainly attributed to the poor surface treatment before dry etching.

Similar to the cases in Ar flow rate, the increase in the bias power can increase the kinetic energies of the incident ions and thus enhance physical ion bombardments. Therefore, higher etching rate can be obtained. The increase in the bias power can also enhance the vertical sidewall profile as a result of the stronger physical ion bombardments.

Figure 3-7 shows the etching rate under different  $\text{Cl}_2$  flow rates. The  $\text{Cl}_2$  flow rate ranged from 10 to 50 sccm. The other dry etching parameters such as the ICP power, the bias power, the chamber pressure and the Ar flow rate were fixed, as shown in Table 3-3. The etching rate increased with the  $\text{Cl}_2$  flow rate. This is because more reactive Cl radicals were generated to participate in the surface chemical reaction as a higher  $\text{Cl}_2$  flow rate was employed. Fig. 3-8 shows the SEM images of the sidewall profile and the surface morphology. Very sharp sidewall profile and very smooth surface were observed in all samples, indicating that the change in the  $\text{Cl}_2$  flow rate does not have a significant influence on the etched sidewall profile and surface morphology.

### 3-4 Conclusions

We systematically investigated the ICP etching of GaN. We studied the process for the Ni mask fabrication. Ni masks fabricated by the lift-off process have very smooth edge and excellent dimension control. In addition, the dependence of the etching rate and the etched sidewall profile of GaN on the etching parameters, such as the bias power, the Ar flow rate and the Cl<sub>2</sub> flow rate, were studied. A larger bias power can enhance the etching rate and the vertical sidewall profiles as a result of the stronger physical ion bombardments. Proper adjustment in the Ar flow rate also enhances the etching rate and the vertical sidewall profiles. The increase in the Cl<sub>2</sub> flow rate increases the etching rate since more reactive Cl radicals are generated to react with the underlying GaN. But no obvious change in the etched sidewall profiles was observed. A proper etching rate together with the vertical sidewall profile and smooth surface developed in this work are applicable in the fabrication of GaN-based devices.



## References

- [1] S. J. Pearton, J. C. Zolper, R. J. Shul and F. Ren, J. Appl. Phys. **86**, 1 (1999).





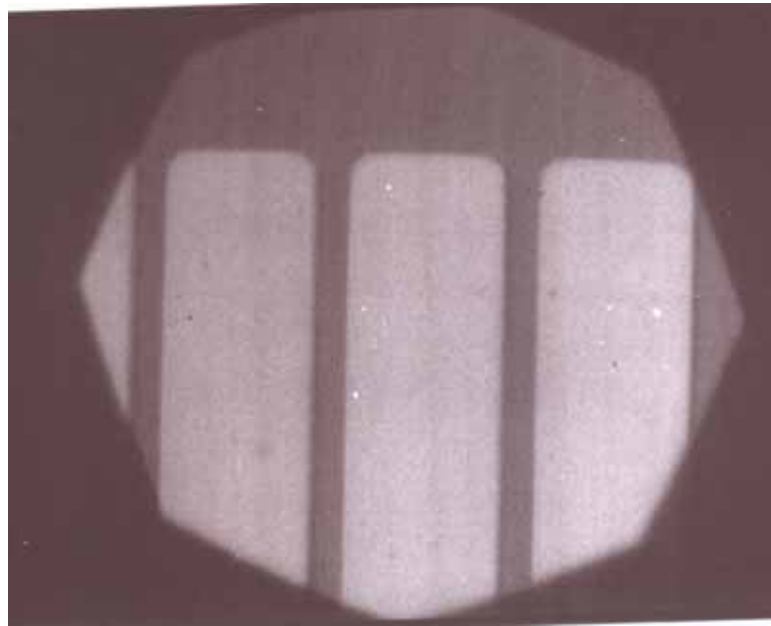


Fig. 3-1 Optical microscope (OM) images of the Ni metal masks. This is done after lift-off process was performed.

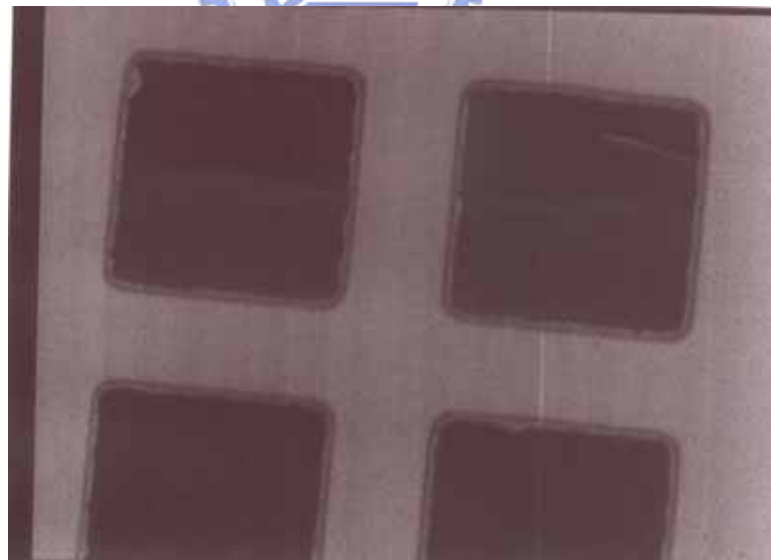


Fig. 3-2 Optical microscope (OM) images of the Ni metal mask, where the black parts represent the etched Ni mask and the outer transparent parts represent photoresists. This is done by the wet etching process.

Table 3-1 Etching condition where the Ar flow rate was modulated.

No.	1	2	3	4	5
ICP power (w)	300	300	300	300	300
Bias power (w)	30	30	30	30	30
Pressure (mtorr)	15	15	15	15	15
Cl <sub>2</sub> flow (sccm)	50	50	50	50	50
Ar flow (sccm)	5	10	15	20	25
Time (min.)	4	4	4	4	4
Etch depth (Å)	13531	13552	13467		13384
	13013		13765		13127
Etch rate (Å/min.)	3318	3338	3404	3333	3314

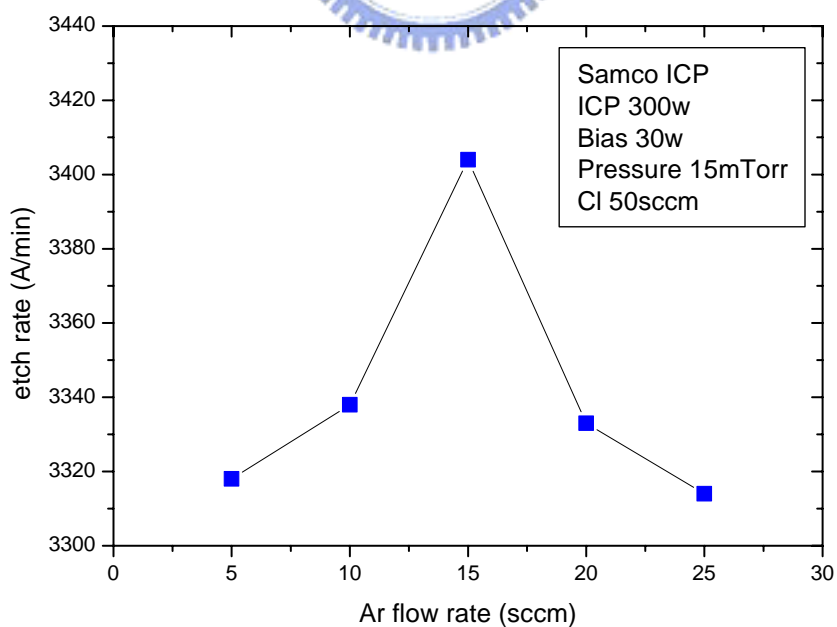
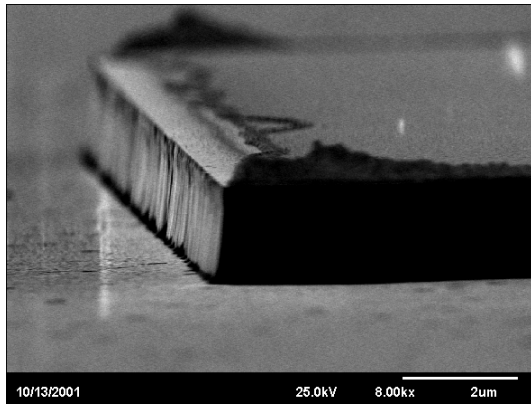
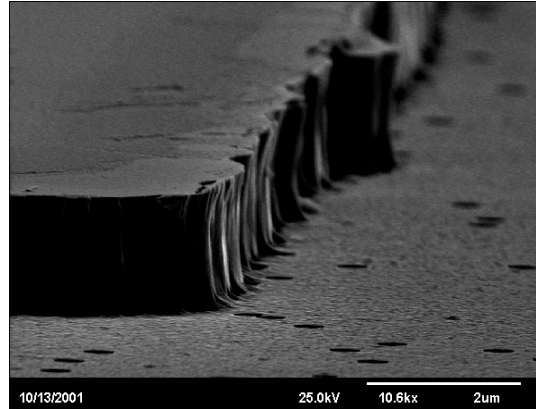


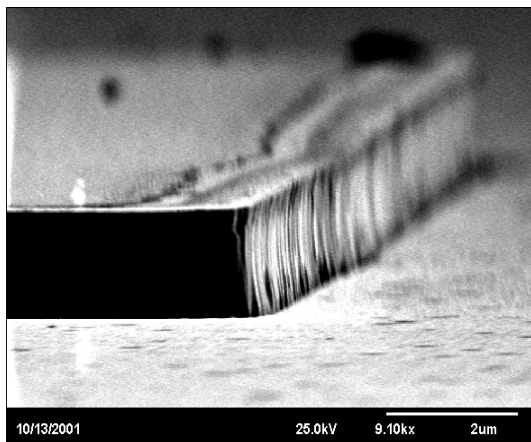
Fig. 3-3 Etching rates under different Ar flow rates.



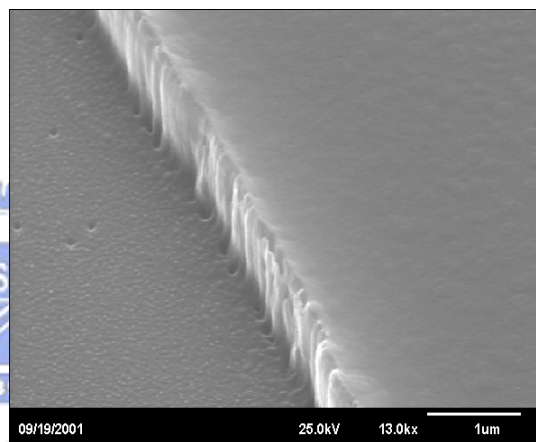
(a) Ar flow: 5 sccm



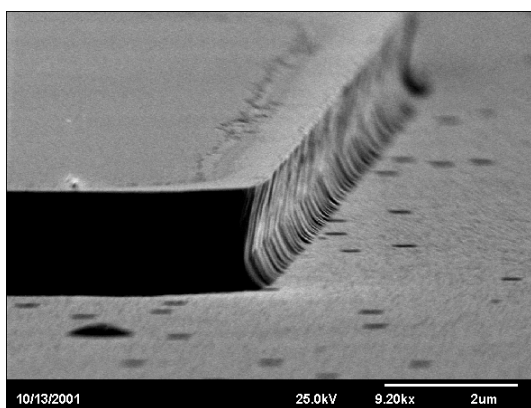
(b) Ar flow: 10 sccm



(c) Ar flow: 15 sccm



(d) Ar flow: 20 sccm



(e) Ar flow: 25 sccm

Fig. 3-4 SEM images of the sidewall profile after ICP etching was performed under different Ar flow rates.

Table 3-2 Etching condition where the bias power was modulated.

No.	1	2	3	4
ICP power (w)	300	300	300	300
Bias power (w)	5	10	20	30
Pressure (mtorr)	15	15	15	15
Cl <sub>2</sub> flow (sccm)	50	50	50	50
Ar flow (sccm)	5	5	5	5
Time (min.)	4	4	4	4
Etch depth (Å)	450	2181	6247	10518
Etch rate (Å/min.)	113	545	1562	2630

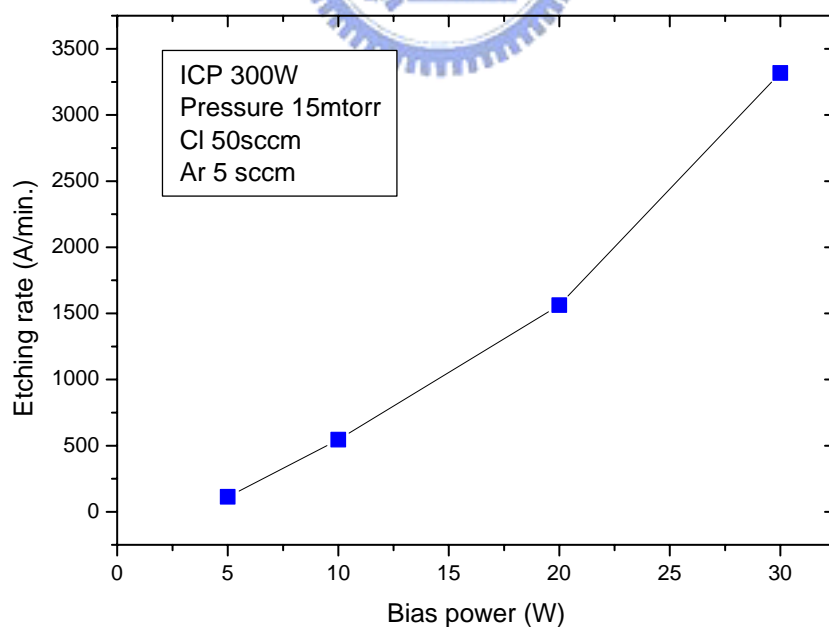
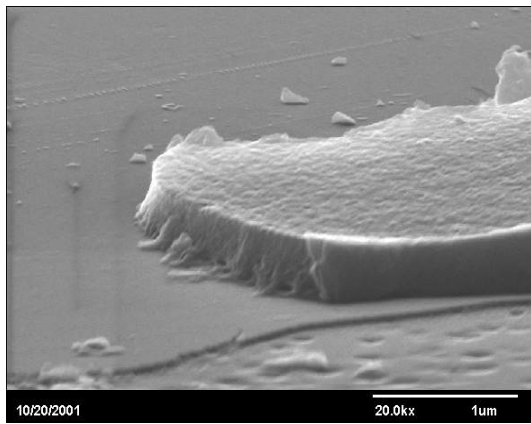
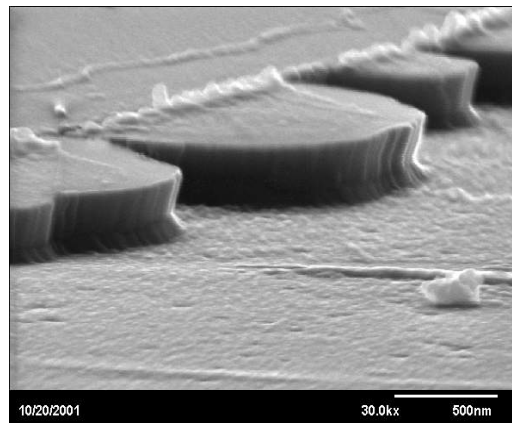


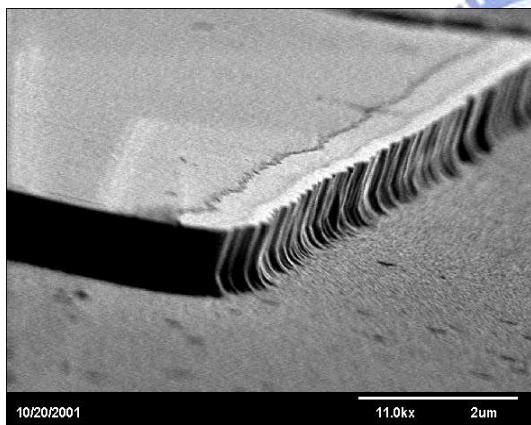
Fig. 3-5 Etching rate under different bias powers.



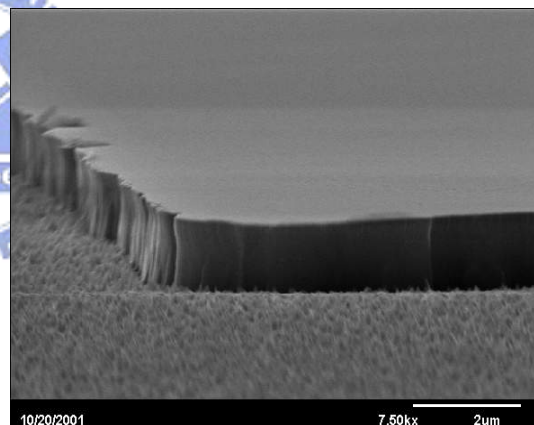
(a) Bias power: 5 w



(b) Bias power: 10 w



(c) Bias power: 20 w



(d) Bias power: 30 w

Fig. 3-6 SEM images of the sidewall profile after ICP etching was performed under different bias power.

Table 3-3 Etching condition where the Cl<sub>2</sub> flow was modulated.

No.	1	2	3	4	5
ICP power (w)	300	300	300	300	300
Bias power (w)	30	30	30	30	30
Pressure (mtorr)	15	15	15	15	15
Cl <sub>2</sub> flow (sccm)	10	20	30	40	50
Ar flow (sccm)	5	5	5	5	5
Time (min.)	4	4	4	4	4
Etch depth (Å)	10820	11359	11695	13251	13728
Etch rate (Å/min.)	2705	2840	2924	3313	3432

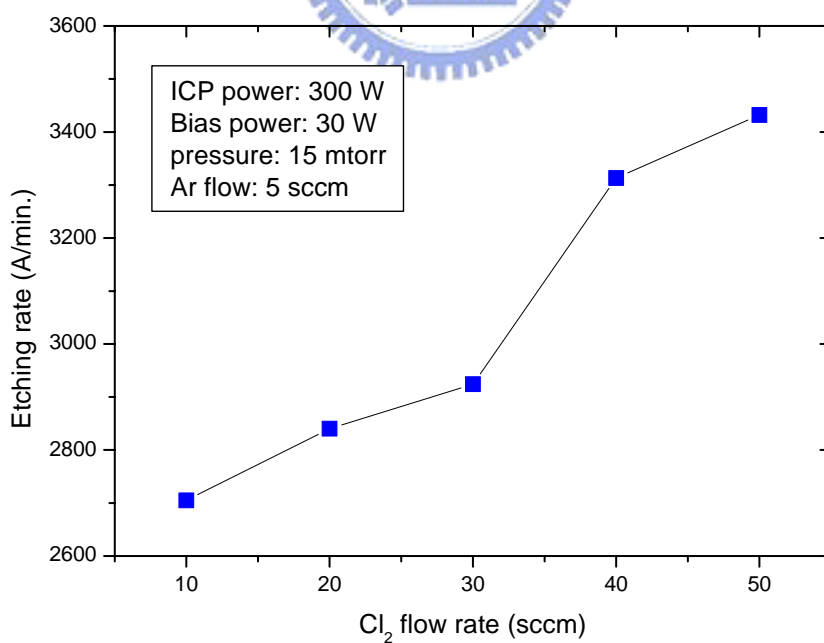
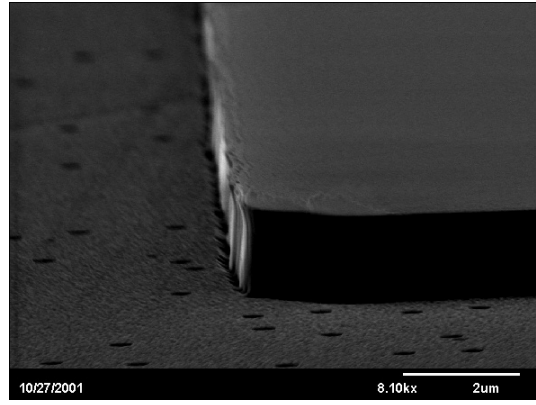
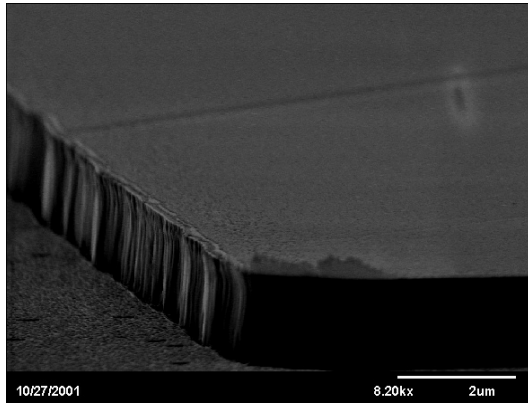
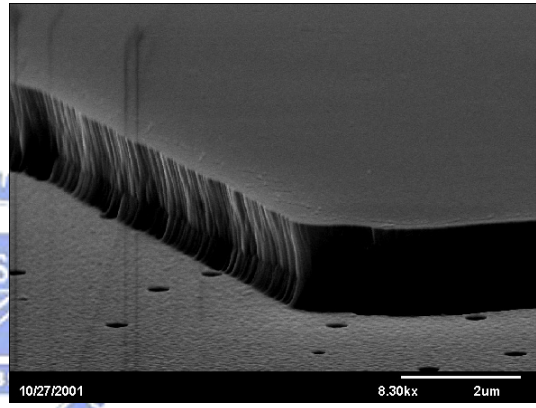
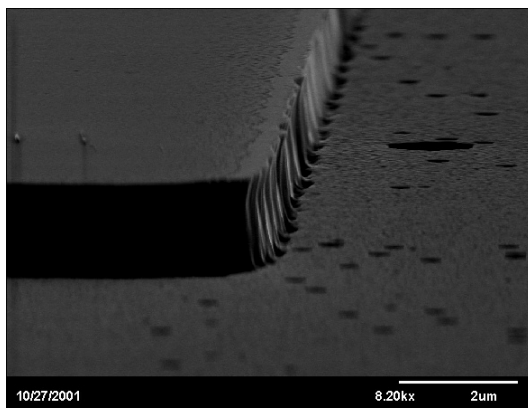


Fig. 3-7 Etching rate as a function of the Cl<sub>2</sub> flow rate.

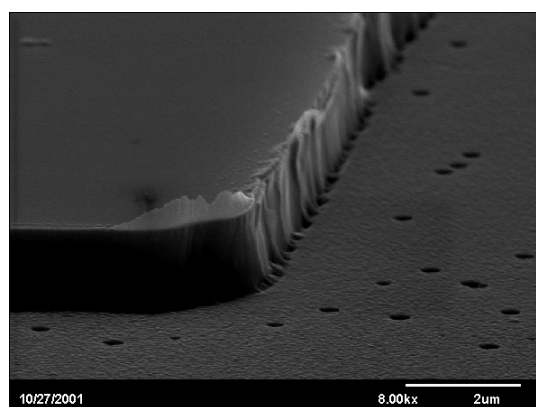
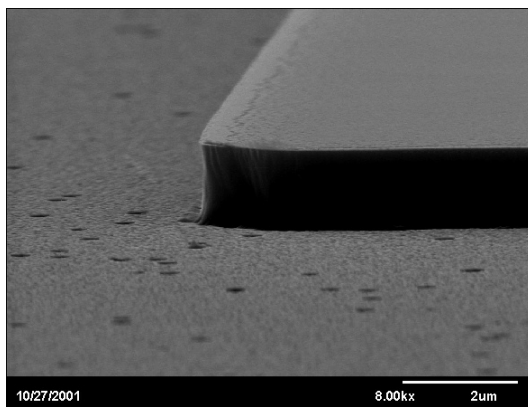




(a) Cl<sub>2</sub> flow rate: 10 sccm

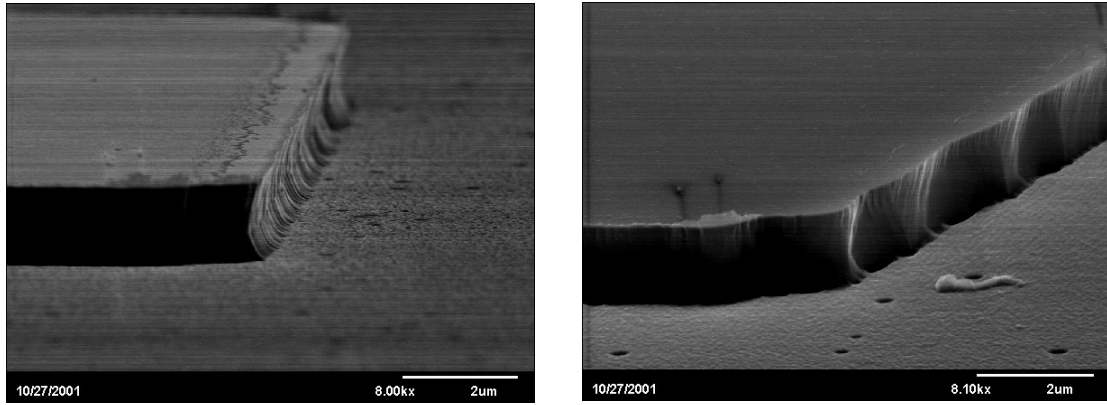


(b) Cl<sub>2</sub> flow rate: 20 sccm

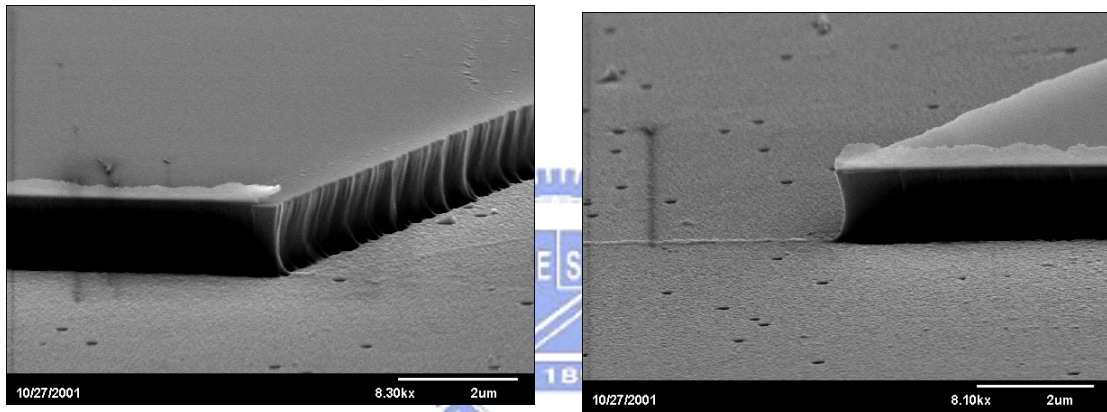


(c) Cl<sub>2</sub> flow rate: 30 sccm

Fig. 3-8 SEM images of the sidewall profile after ICP etching was performed under different Cl<sub>2</sub> flow rates.



(d)  $\text{Cl}_2$  flow rate: 40 sccm



(e)  $\text{Cl}_2$  flow rate: 50 sccm

Fig. 3-8 SEM images of the sidewall profile after ICP etching was performed under different  $\text{Cl}_2$  flow rates.



## Chapter 4

### Low resistance Ohmic contacts to n-GaN

#### 4-1 Introduction

Nitride-based electronic devices, such as heterostructure field-effect transistors (HFETs) and heterostructure bipolar transistors (HBTs), are potentially very useful for high-power and high-temperature applications due to their excellent material properties. To use these devices for such applications, good Ohmic contacts with low contact resistance and good thermal stability are very important. In general, Ohmic contacts to n-GaN with low contact resistance are not easily obtainable because of its wide bandgap. The contact resistance could be improved by various approaches, such as the selection of right contact metal [1-7], the surface treatments [8-9] and the plasma treatments [10-16]. In particular, proper surface plasma treatment has been shown to be very effective in the improvement of contact resistance. Several studies on the thermal stability of Ohmic contacts to GaN have been performed [17-20], however, the thermal stability of the plasma-treated Ohmic contacts has not been studied. Whether the damages created or the defects generated by plasma treatment have any effect on the reliability of the device contacts needs to be answered. In addition, thermal annealing is also very important. Thermal annealing in N<sub>2</sub> gas ambient was usually employed to obtain low resistance Ohmic contacts. The main reason for using nitrogen gas as the

annealing ambient instead of hydrogen containing gas, as commonly used by most III-V compounds, is to avoid the effect of hydrogen passivation of dopants in GaN [5]. In this work, we carried out extensive investigations on the Ohmic contacts to n-GaN. Various plasma treatments using Cl<sub>2</sub>/Ar or Ar species were employed to improve the contact resistance of n-GaN. Additionally, thermal aging tests were performed to further observe the thermal stability of the plasma-treated Ohmic contacts. Moreover, we compared the contact resistance of the samples annealed in forming gas ambient with those in N<sub>2</sub> ambient so as to observe if forming gas ambient is applicable to the thermal annealing process of n-GaN. We found that proper plasma treatment can significantly improve the contact resistance. No obvious degradation of contact resistance was observed after aging at 600°C for 2 h in N<sub>2</sub> and air ambient. Furthermore, the forming gas was shown to further improve the contact resistance of n-GaN.

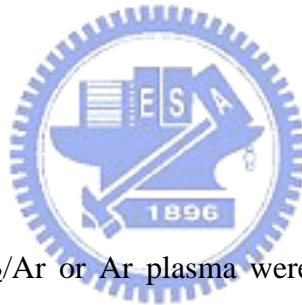
## 4-2 Experiments

The 2- $\mu\text{m}$ -thick n-GaN films for this study were grown by metalorganic chemical vapor deposition (MOCVD) on c-plane sapphire substrates. Samples with different doping concentrations,  $8.7 \times 10^{16} \text{ cm}^{-3}$  and  $3.3 \times 10^{18} \text{ cm}^{-3}$ , were used. After layer growth, mesa patterns for transmission line measurement (TLM) were defined by photolithography. Prior to contact metal deposition, the samples were treated by Cl<sub>2</sub>/Ar or Ar plasma using an inductive coupled

plasma (ICP) system and then dipped in the solution of 1:1 HCl:H<sub>2</sub>O for 1 min. Contact metal, Ti/Al/Ti/Au (200/1500/450/550 Å), was deposited and lifted-off to form the contact pads. The dimension of contact pad was 100×100 μm<sup>2</sup>. The samples were annealed at 750°C for 30 s in N<sub>2</sub> ambient or forming gas ambient. Aging tests were carried out at temperatures ranging from 400 to 600°C for 2 h in N<sub>2</sub> or air ambient to observe the thermal stability of plasma-treated Ohmic contacts. The TLM measurement was then performed for the determination of the contact resistance.

## 4-3 Results and Discussion

### 4-3-1 Plasma treatments



Various treatments using Cl<sub>2</sub>/Ar or Ar plasma were employed to improve the contact resistance of n-type GaN. Samples with different doping concentrations, 8.7×10<sup>16</sup> and 3.3×10<sup>18</sup> cm<sup>-3</sup>, were used to observe the strength of plasma treatments.

#### *Part 1. n-GaN with $N_D=8.7\times 10^{16}$ cm<sup>-3</sup>*

The conditions of the plasma treatment and the TLM results are shown in Table 4-1. It should be noted that a very low bias power of 5 W was used in the plasma treatment to ensure a very slow etching rate for GaN. For the conditions used here, only about 100-200 Å was etched during the plasma treatment. After annealing at 750°C for 30 s in a N<sub>2</sub> ambient, all

samples showed Ohmic behavior. For Cl<sub>2</sub>/Ar plasma treated samples, the contact resistances were 0.638, 0.614, and 0.28 Ω·mm for treatment times of 0, 1 and 2 min. (sample Nos. 1, 2, and 6), respectively. As expected, samples with a longer treatment time have better contact resistances. We also found that Ar flow rate has a significant influence on the contact resistance. Sample No. 5, which was treated with a flow rate ratio of Cl<sub>2</sub>/Ar = 50/20 for 2 min., has the best result. Its contact resistance and specific contact resistance are 0.21 Ω·mm and 6.8x10<sup>-7</sup> Ω·cm<sup>2</sup>, respectively. For samples treated with Ar plasma only, the contact resistance and specific contact resistance decrease with the Ar flow rate. The best results are obtained for an Ar flow of 50 sccm. The contact resistance and specific contact resistance are 0.3 Ω·mm and 8.7x10<sup>-7</sup> Ω·cm<sup>2</sup>, respectively.



*Part 2. n-GaN with  $N_D=3.3 \times 10^{18} \text{ cm}^{-3}$*

The conditions of the plasma treatment are shown in Table 4-2. Figure 4-1 shows the current-voltage characteristics of the as-deposited Ohmic contacts under different Ar flow rates. With the increase of Ar flow, the current-voltage characteristics of these contacts became more linear. Fig. 4-2 shows the dependence of the contact resistance and the specific contact resistance on the Ar flow rate. Both the contact resistance and specific contact resistance decreased as the Ar flow rate was increased. For samples without Ar plasma treatment, the contact resistance and the specific contact resistance were too high to be

extracted via the TLM measurement. Samples treated with an Ar flow rate of 50 sccm showed the best result. Their contact resistance and specific contact resistance were  $0.362 \Omega\cdot\text{mm}$  and  $3.9\times 10^{-5} \Omega\cdot\text{cm}^2$ , respectively. After annealing, all samples showed linear current-voltage characteristics, as shown in Fig. 4-3. Similar dependences of the contact resistance and the specific contact resistance of the alloyed contacts on Ar flow rate were obtained as well, as shown in Fig. 4-4. All alloyed contacts have low contact resistances. Samples treated with 50 sccm of Ar flow rate still exhibited the best electrical characteristics. Their contact resistance and specific contact resistance were  $0.103 \Omega\cdot\text{mm}$  and  $3.2\times 10^{-6} \Omega\cdot\text{cm}^2$ , respectively.

Apparently, the Ar flow rate has a significant influence on contact resistance. With the increase of Ar flow rate, the contact resistance is improved markedly. The mechanism of Ar plasma etching is physical ion bombardment. Higher Ar flow rate generates higher Ar ion density in the plasma, which enhances the effect of ion bombardment on wafer surface. Thus more lattice damage and crystalline defects are created on wafer surface. The increase of the nitrogen vacancies on wafer surface after plasma treatment has been shown by many researchers [10, 13, 15] and they are generally believed to be native donors [21-22]. Therefore, after plasma treatment with Ar, the improvement of contact resistance is attributed to the increase of nitrogen vacancies on the wafer surface.

Figure 4-5 shows the current-voltage characteristics of the as-deposited Ohmic contacts (before annealing) with different Ar treatment times. We found that Ar treatment improves the

Ohmic contact if the duration is less than 1 minute. But if it is too long, the Ohmic contact becomes worse. After a 3 min. of Ar plasma treatment, the current-voltage characteristics are even poorer than those without treatment. After thermal annealing, all samples show good Ohmic behavior, as shown in Fig. 4-6. Substantial improvement can be obtained for the samples treated with shorter times ( $t = 1, 2$  min.). Figure 4-7 shows the dependence of contact resistance and specific contact resistance of the alloyed contacts on the treatment time. As a whole, samples with different treatment times all have lower contact resistances and specific contact resistances than those without treatment. However, for the best result, the treatment time has to be kept no longer than 1 min. The sample with 1 min. of Ar plasma treatment has the lowest contact resistance ( $0.103 \Omega\text{-mm}$ ) and specific contact resistance ( $3.2 \times 10^{-6} \Omega\text{-cm}^2$ ).

Plasma treatment not only produces nitrogen vacancies on the surface, which is desirable for the improvement of contact resistance, but also causes crystalline defects, which can degrade the film quality and the contact resistance [12]. So to use such technique for contact improvement, one has to carefully choose the treatment time so that the damage it causes does not overwhelm the benefit it produces.

#### **4-3-2 Thermal stability issue**

Samples with an electron concentration of  $8.7 \times 10^{16} \text{ cm}^{-3}$  and treated with  $\text{Cl}_2/\text{Ar}$  or Ar plasma were used to study the thermal stability of the plasma-treated Ohmic contacts to

n-GaN. Figures 4-8 to 4-10 show the contact resistance and the specific contact resistance versus aging temperature ranging from 400 to 600°C in N<sub>2</sub> ambient. Figures 4-8 and 4-9 are for the Cl<sub>2</sub>/Ar treated samples and Fig. 4-10 is for the Ar treated samples. As a whole, there is no obvious electrical degradation after aging at 600°C for 2 h for samples either with or without the plasma treatment. The above results indicate that the TiN layer formed at the interface after thermal annealing is thermodynamically stable under this aging condition. Another notable issue is the thermal stability of plasma damage caused by plasma treatment. It is generally believed that the improvement of contact resistance after plasma treatment is mainly due to the formation of nitrogen vacancies on the wafer surface. High-temperature annealing would improve the crystal quality of the GaN epilayer and reduce the defect density on the wafer surface [23]. Although the effect of high-temperature aging on the recovery of the plasma-induced damages is largely unknown, the results obtained here indicate that this annealing effect does not lead to electrical degradation of plasma-treated Ohmic contacts. For samples that were aged in air ambient, similar results were obtained, as shown in Fig. 4-11. The plasma-treated Ohmic contacts were also measured at high temperatures. At 300°C, sample No. 5 still maintains a very low contact resistance (0.412 Ω·mm) and a low specific contact resistance ( $9.3 \times 10^{-7}$  Ω·cm<sup>2</sup>), which are lower than those measured at room temperature of samples without plasma treatment (sample No. 1). Thus, from the thermal

aging tests and their high-temperature characteristics, it is apparent that the plasma-treated Ohmic contacts exhibited excellent thermal stability.

#### 4-3-3 Forming gas ambient treatments

Samples with an electron concentration of  $3.3 \times 10^{18} \text{ cm}^{-3}$  and treated with  $\text{Cl}_2/\text{Ar}$  or Ar plasma were used to study the influence of the forming gas ambient treatment on the plasma-treated Ohmic contacts to n-GaN. Figure 5-8 shows the current-voltage characteristics of the Ohmic contacts after annealing in forming gas (15%  $\text{H}_2$ ). All samples showed good Ohmic behavior. In comparison with the samples without plasma treatment, substantial improvement in electrical characteristics was obtained as well. Fig. 5-9 shows the comparison of specific contact resistance of the Ohmic contacts annealed in  $\text{N}_2$  and in forming gas ambient. Similar to the results of those annealed in  $\text{N}_2$  gas, the specific contact resistance of the samples annealed in forming gas decreases with the Ar flow rate. It is apparent that the forming gas treated contacts have lower specific contact resistance than those annealed in  $\text{N}_2$  gas ambient. The lowest contact resistance and specific contact resistance obtained here are  $0.093 \text{ } \Omega \cdot \text{mm}$  and  $2.6 \times 10^{-6} \text{ } \Omega \cdot \text{cm}^2$ , respectively.

Obviously, from the results presented above, annealing in forming gas is better than annealing in  $\text{N}_2$ . The possible reason is the reduction capability of the forming gas because of the  $\text{H}_2$  content. It may reduce the oxidation reaction of metal at high temperatures and

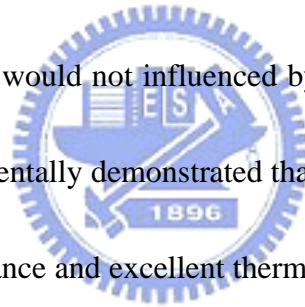


therefore help reduce the contact resistance. Similar results were also observed in the Al/n-GaN Ohmic contacts annealed in Ar/4% H<sub>2</sub> forming gas [24]. The H<sub>2</sub> content, however, may cause concerns in carrier concentration reduction because of hydrogen passivation. It is known that hydrogen passivation of p-type dopants in p-GaN would result in a large decrease of hole concentration [25-26]. Whether annealing in forming gas ambient would lead to similar reduction in electron concentration and increase in the contact resistance of n-GaN needs to be answered. During annealing process, H<sub>2</sub> could diffuse into the bulk n-GaN to form neutral complexes with dopants at annealing temperature higher than 500°C. On the other hand, high temperature annealing process would also result in the dissociation of neutral dopant-H complexes [27]. Although the effect of hydrogen passivation of n-type dopants in n-GaN during the annealing and subsequent cooling process is not completely known, the results obtained here indicate that annealing in forming gas ambient would not lead to electrical degradation of Ohmic contacts.

#### **4-4 Conclusions**

We extensively investigated the Ohmic contacts to n-GaN. Proper treatments using the Cl<sub>2</sub>/Ar or Ar plasma can effectively improve the contact resistance for n-GaN with a doping concentration ranging from  $8.7 \times 10^{16} \text{ cm}^{-3}$  to  $3.3 \times 10^{18} \text{ cm}^{-3}$ . Particularly, the Ar flow rate can have a significant effect on contact resistance. We also studied the high temperature thermal

stability of plasma-treated Ohmic contacts to n-GaN. Although the thermal treatment may have some annealing effect on the plasma-generated defects, which are known to be the reason for low contact resistance. No obvious degradation in contact resistance was observed after aging for 2 h in either N<sub>2</sub> or air ambient. Thus the thermal stability of plasma-treated Ohmic contacts is not affected by the recovery of plasma-induced damages on the wafer surface. Furthermore, we studied the influence of the forming gas ambient treatments. Even lower contact resistance and specific contact resistance were obtained for contacts annealed in forming gas ambient than those annealed in N<sub>2</sub> ambient. This indicates that the electrical characteristics of Ohmic contacts would not be influenced by the effect of hydrogen passivation of dopants in n-GaN. We experimentally demonstrated that the plasma-treated Ohmic contacts to n-GaN, with low contact resistance and excellent thermal stability, are highly applicable for the nitride-based electronic devices in high-power and high-temperature applications.



## References

- [1] J. S. Foresi and T. D. Moustakas, Appl. Phys. Lett. **62**, 2859 (1993).
- [2] M. E. Lin, Z. Ma, F. Y. Huang, Z. F. Fan, L. H. Allen, and H. Morkoc, Appl. Phys. Lett. **64**, 1003 (1994).
- [3] M. W. Cole, D. W. Eckart, W. Y. Han, R. L. Pfeffer, T. Monahan, F. Ren, C. Yuan, R. A. Stall, S. J. Pearton, Y. Li and Y. Lu, J. Appl. Phys. **80**, 278 (1996).
- [4] J. H. Chern, L. P. Sadwick, P. J. Hwu, High Temperature Electronics Conf., 114 (1998).
- [5] Q. Z. Liu and S. S. Lau, Solid-State Electron. **42**, 677, (1998).
- [6] L. L. Smith, R. F. Davis, R. J. Liu, M. J. Kim and R. W. Carpenter, J. Mater. Res. **14**, 1032, (1999).
- [7] C. T. Lee and H. W. Kao, Appl. Phys. Lett. **76**, 2364 (2000).
- [8] Y. Koyama, T. Hashizume, H. Hasegawa, Solid-State Electron. **43**, 1483 (1999).
- [9] Y. J. Lin and C. T. Lee, Appl. Phys. Lett. **77**, 3986 (2000).
- [10] Z. Fan, S. N. Mohammad, W. Kim, O. Aktas, A. E. Botchkarev and H. Morkoc, Appl. Phys. Lett. **68**, 1672 (1996).
- [11] H. S. Kim, Y. H. Lee, G. Y. Yeom, J. W. Lee and T. I. Kim, Mater. Sci. Eng. **B50**, 82 (1997).
- [12] A. T. Ping, Q. Chen, J. W. Yang, M. A. Khan and I. Adesida, J. Electron. Mater. **27**, 261 (1998).
- [13] J. Y. Chen, C. J. Pan and G. C. Ghi, Solid-State Electron. **43**, 649 (1999).

- [14] C. R. Eddy, JR. and B. Molnar, J. Electron. Mater. **28**, 314 (1999).
- [15] J. M. Lee, K. M. Chang, S. W. Kim, C. H., I. H. Lee, and S. J. Park, J. Appl. Phys. **87**, 7667 (2000).
- [16] H. W. Jang, C. M. Jeon, J. K Kim and J. L. Lee, Appl. Phys. Lett. **78**, 2015 (2001).
- [17] B. P. Luther, S. E. Mohny, J. M. Delucca and R. F. Karliceck, JR., J. Electron. Mater. **27**, 196 (1998).
- [18] J. H. Chern, L. P. Sadwick and P. J. Hwu, High Temperature Electronics Conf., p.114 (1998).
- [19] L. L. Smith, R. F. Davis, R. J. Liu, M. J. Kim and R. W. Carpenter, J. Mater. Res. **14**, 1032 (1999).
- [20] C. T. Lee and H. W. Kao, Appl. Phys. Lett. **76**, 2364 (2000).
- [21] H. P. Maruska and J. J. Tieyjen, Appl. Phys. Lett. **15**, 327 (1969).
- [22] R. J. Molnar, T. Lei and T. D. Moustakas, Appl. Phys. Lett. **62**, 72 (1993).
- [23] M. W. Cole, F. Ren and S. J. Pearton, Appl. Phys. Lett. **71**, 3004 (1997).
- [24] B. P Luther, S. E Mohny, T. N. Kackson, M. A. Khan, Q. Chen and J. W. Wang, Appl. Phys. Lett. **70**, 57 (1997).
- [25] S. Nakamura, T. Mukai, M. Senoh and N. Iwasa, Jpn. J. Appl. Phys. **31**, L139 (1992).
- [26] S. Nakamura, N. Iwasa, M. Senoh and T. Mukai, Jpn. J. Appl. Phys. **31**, 1258 (1992).
- [27] S. J. Pearton, J. C. Zolper, R. J. Shul and F. Ren, J. Appl. Phys. **86**, 1 (1999).

Table 4-1 Etching conditions and TLM data

No.	1	2	3	4	5	6	7	8	9
ICP power (w)	-	300	300	300	300	300	300	300	300
Bias power (w)	-	5	5	5	5	5	5	5	5
Pressure (mtorr)	-	15	15	15	15	15	15	15	15
Cl <sub>2</sub> flow (sccm)	-	50	50	50	50	50	-	-	-
Ar flow (sccm)	-	30	10	15	20	30	10	30	50
Time (min.)	-	1	2	2	2	2	1	1	1
Rc ( $\mu$ · mm)	0.638	0.614	0.48	0.45	0.21	0.28	0.87	0.57	0.3
s ( / )	621.0	656.3	692.2	696.3	668.3	671.5	673	649.3	803
c ( $\mu$ · cm <sup>2</sup> )	6.6	5.7	3.4	2.8	0.68	1.2	11	5.0	0.87

Table 4-2 The conditions of the plasma treatment

ICP power (W)	-	300	300	300	300	300
Bias power (W)	-	5	5	5	5	5
Pressure (mTorr)	-	15	15	15	15	15
Ar flow (sccm)	-	10	30	50	50	50
Time (min.)	-	1	1	1	2	3



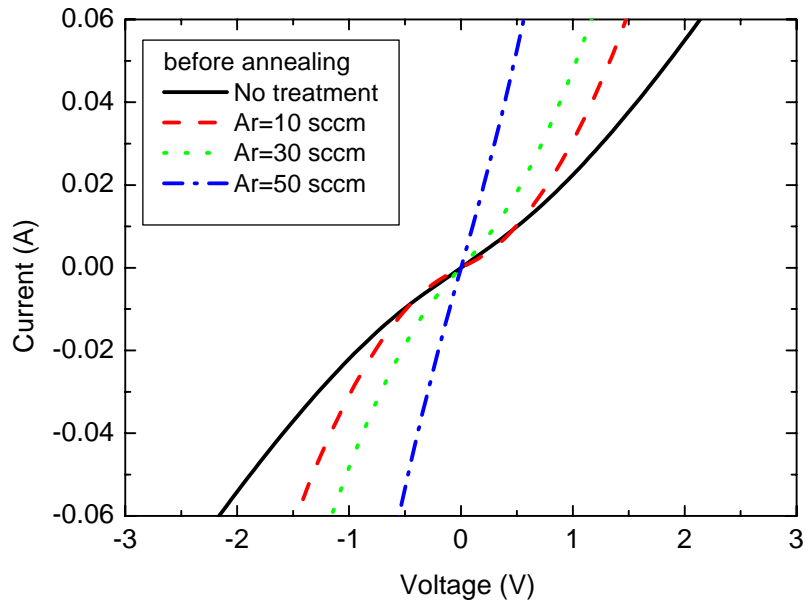


Fig. 4-1 Current-voltage characteristics of the as-deposited ohmic contacts treated with Ar plasma at different Ar flow rate.

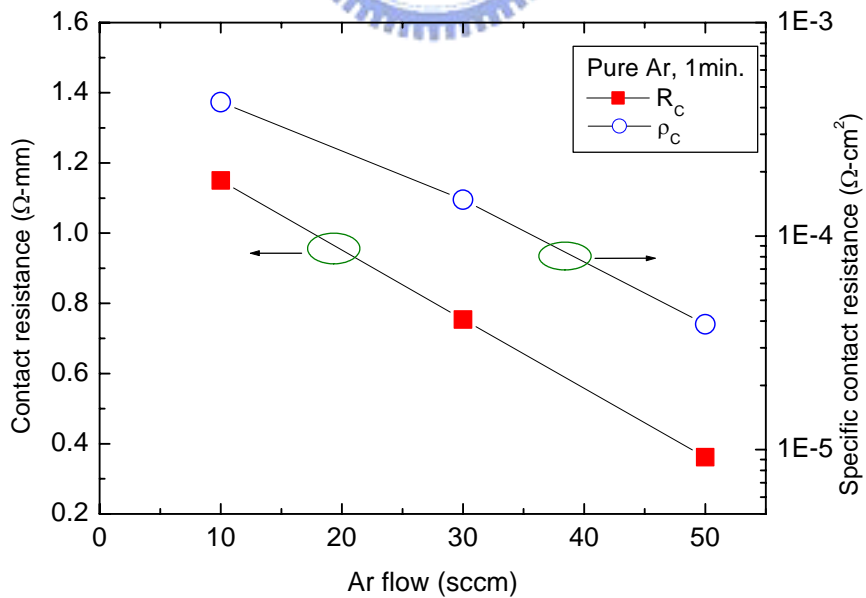


Fig. 4-2 The dependence of contact resistance and specific contact resistance of the as-deposited ohmic contacts on Ar flow rate.

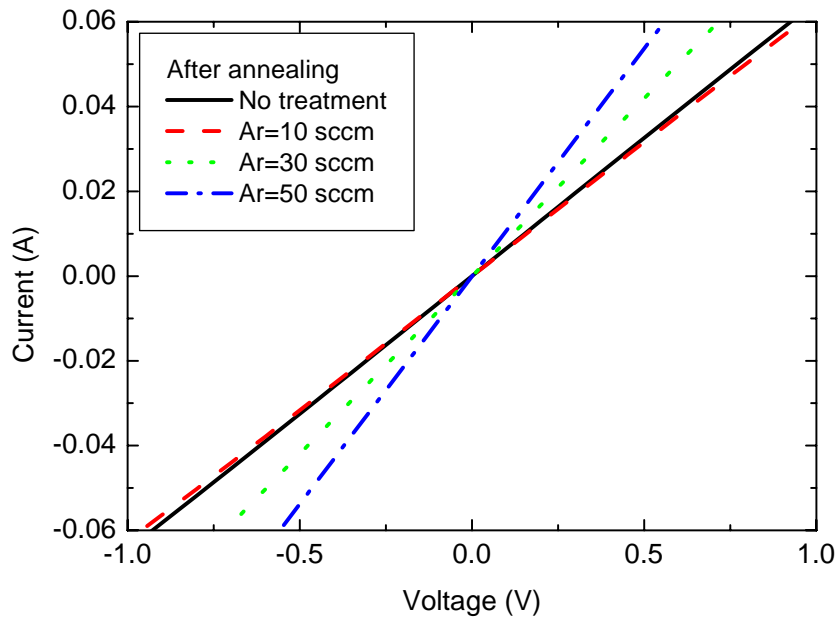


Fig. 4-3 Current-voltage characteristics of the alloyed ohmic contacts under different Ar flow rate.

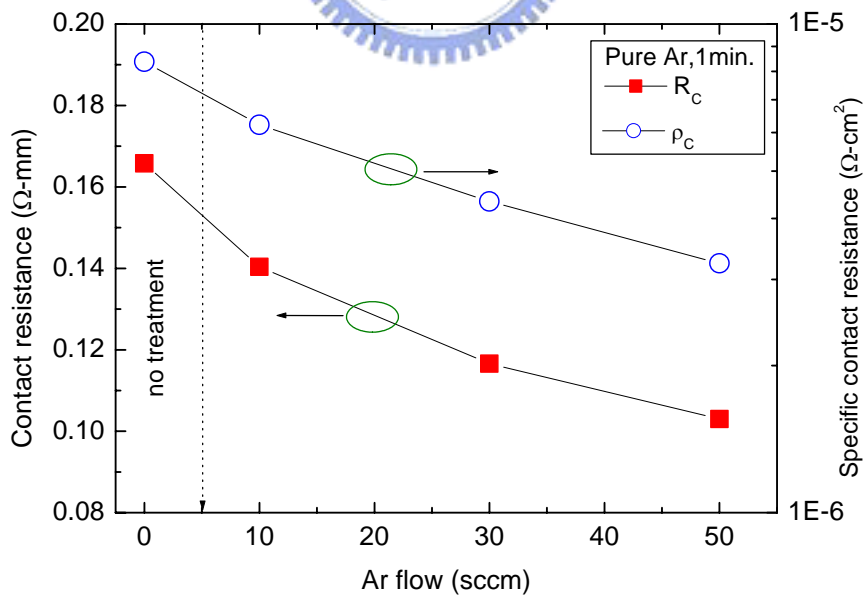


Fig. 4-4 The dependence of contact resistance and specific contact resistance of the alloyed ohmic contacts on Ar flow rate.



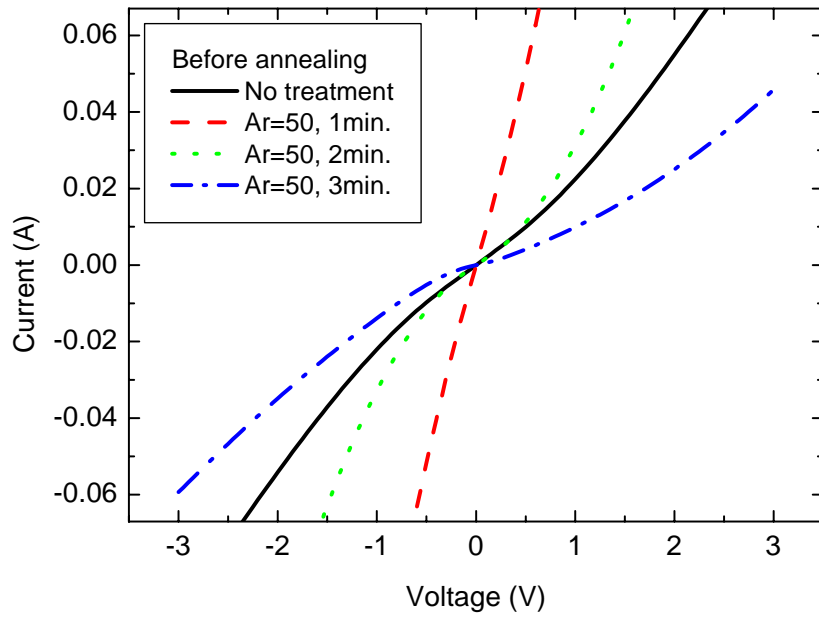


Fig. 4-5 Current-voltage characteristics of the as-deposited ohmic contacts under different Ar treatment time.

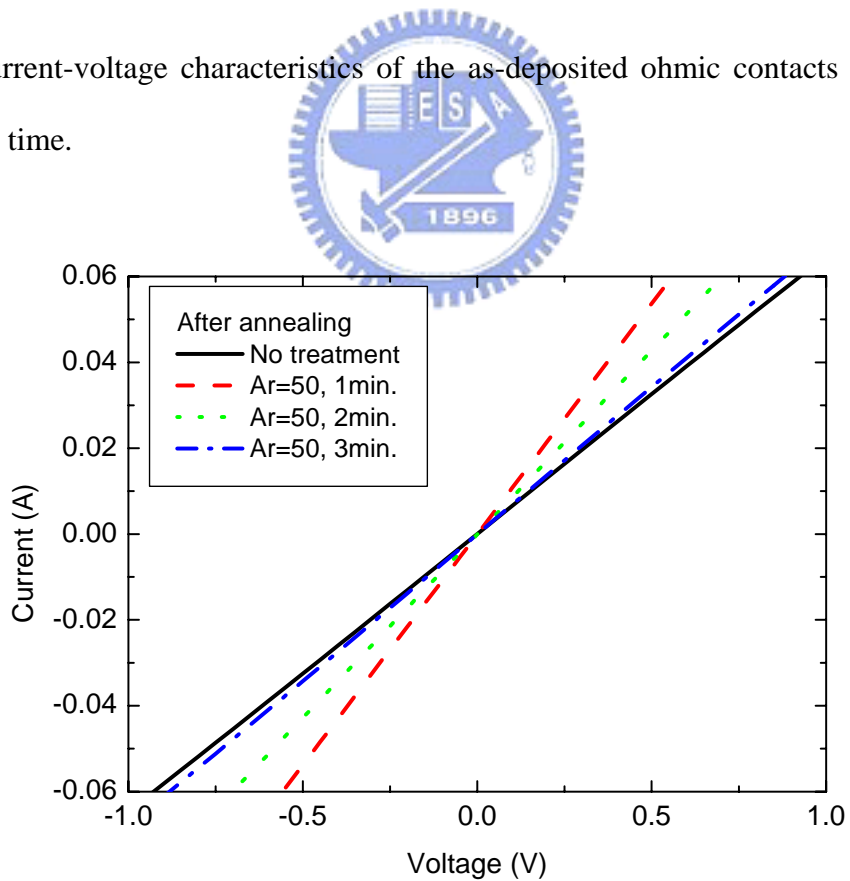


Fig. 4-6 Current-voltage characteristics of the alloyed ohmic contacts under different Ar treatment time.

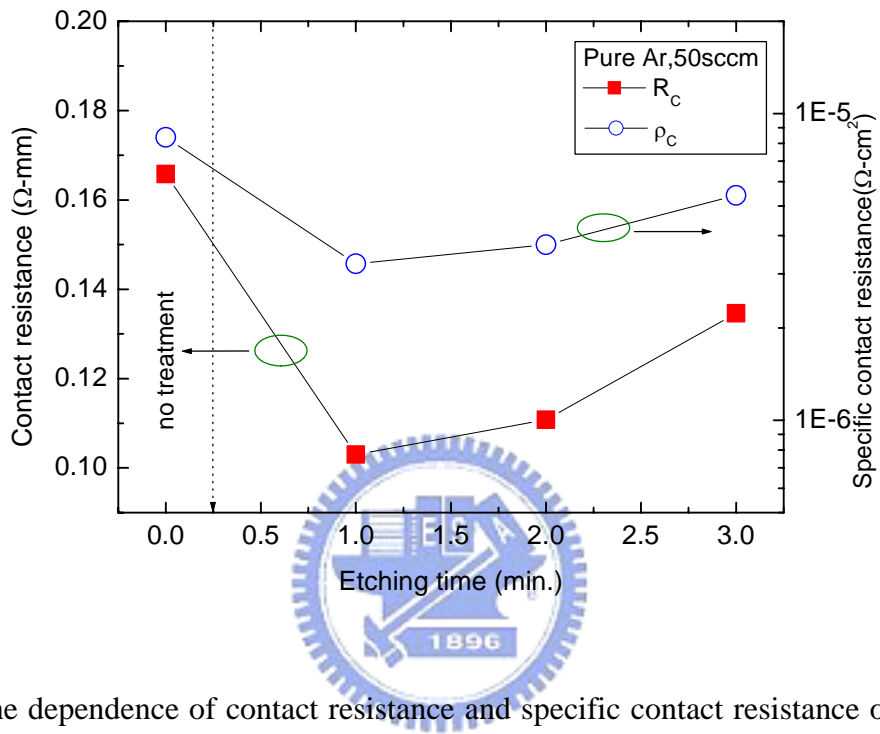


Fig. 4-7 The dependence of contact resistance and specific contact resistance of the alloyed ohmic contacts on Ar treatment time.

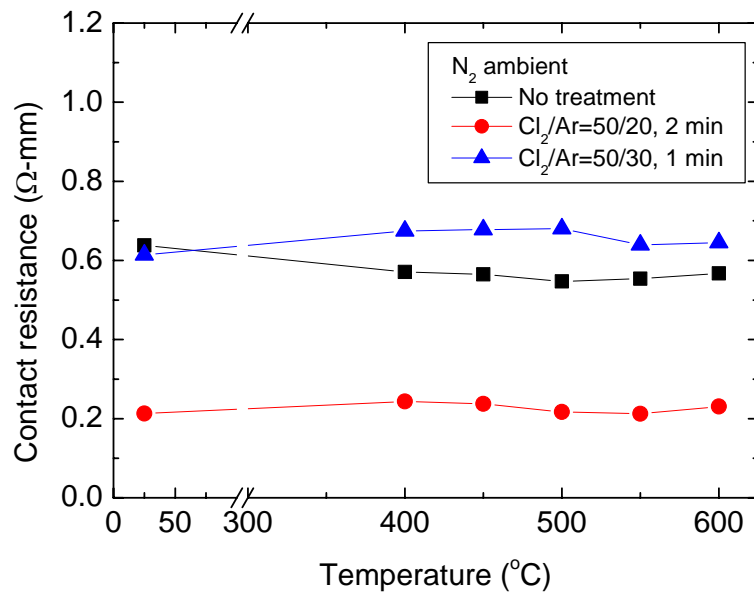


Fig. 4-8 Aging test results of contact resistance in N<sub>2</sub> ambient for samples with Cl<sub>2</sub>/Ar plasma treatment.

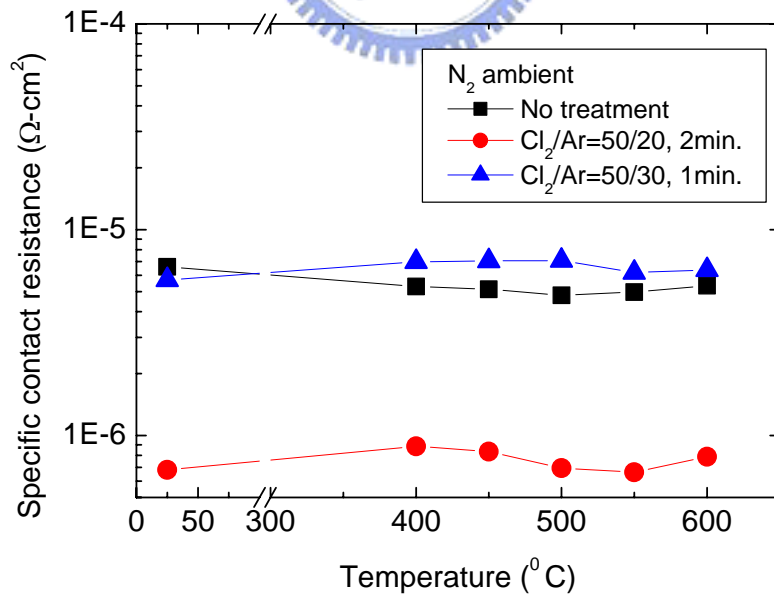


Fig. 4-9 Aging test results of specific contact resistance in N<sub>2</sub> ambient for samples with Cl<sub>2</sub>/Ar plasma treatment.

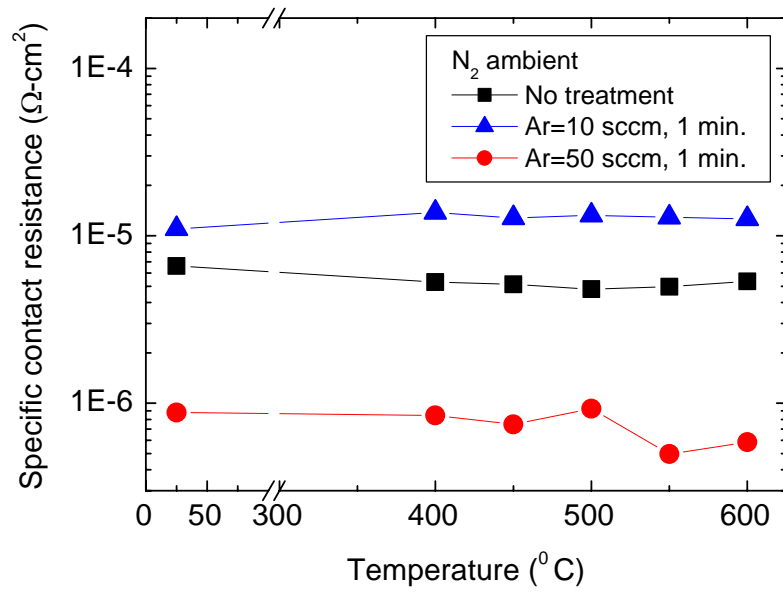


Fig. 4-10 Aging test results of specific contact resistance in N<sub>2</sub> ambient for samples with Ar plasma treatment.

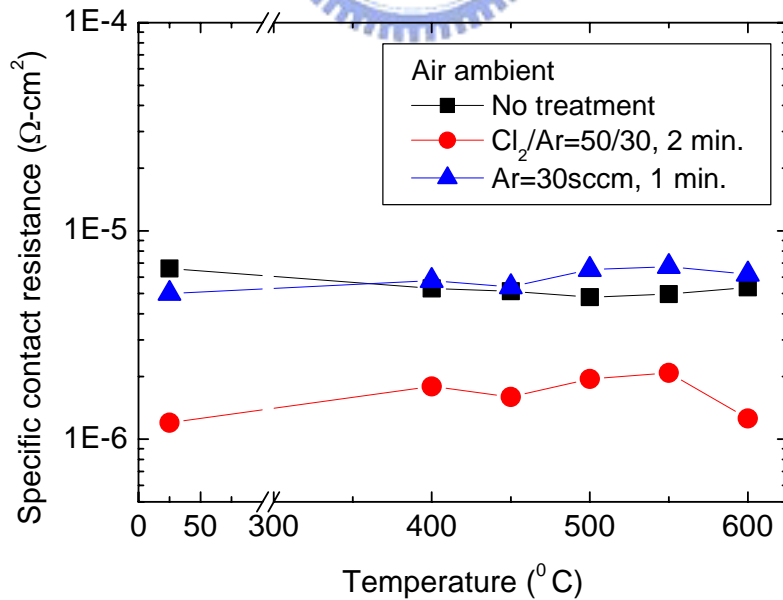


Fig. 4-11 Aging test results of specific contact resistance in air ambient.

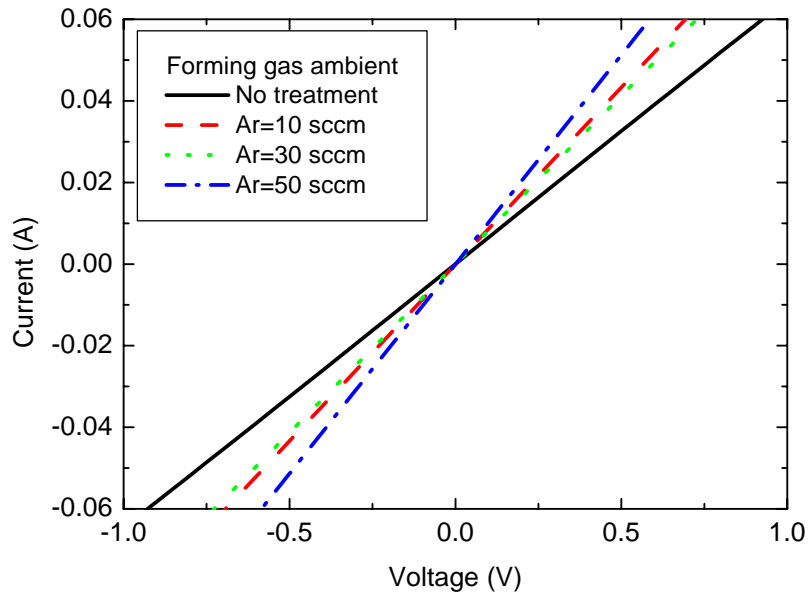


Fig. 4-12 Current-voltage characteristics of the ohmic contacts annealed in forming gas ambient.

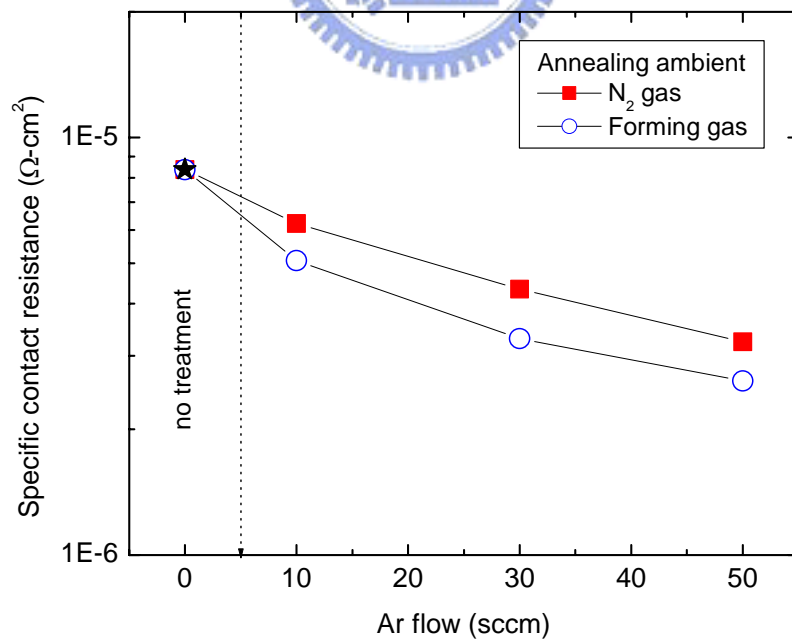


Fig. 4-13 A comparison of specific contact resistance of the ohmic contacts annealed in  $N_2$  gas and in forming gas ambient.

## Chapter 5

### Narrow T-gate fabrication on GaN

#### 5-1 Introduction

GaN-based heterostructure field effect transistors (HFETs) and high electron mobility transistors (HEMTs) are promising candidates for high temperature and high power device applications at high speed. To realize very high performance at high frequencies, a short gate is a necessity. Various methods to fabricate sub-100 nm T-gates have been developed using e-beam lithography, but mostly on GaAs [1-11]. Typically, a high acceleration voltage for the electron beam is required for defining small gate dimensions because of the forward scattering problems. On GaAs, it has been reported that for an 800 nm thick resist a minimum acceleration voltage of around 50 kV is needed [3]. Recently a higher accelerating voltage, 100 kV, was used to achieve a very small gate length [9-11]. However, a lower accelerating voltage for e-beam lithography has some advantages over high voltages, such as less backscattering from the substrate, lower doses and much reduced radiation damage in the underlying substrate [12]. In this work, we report a sub-100 nm T-gate process on GaN using an electron-beam lithography system with a low accelerating voltage of only 15kV. Conventional bi-layer PMMA/PMMA-MAA resist was used together with

a special designed exposure pattern for the gates. T-gates with length of only 40 nm were successfully fabricated.

## 5-2 Experiment

Our electron-beam lithography system consists of a JEOL JSM-6500F field emission scanning electron microscope and a Nanometer Pattern Generation System (NPGS). The electron emitter is a ZrO/W in-lens thermal field emission electron gun. The maximum acceleration voltage is 30 kV. The beam current ranges from 3 pA to 200 nA.



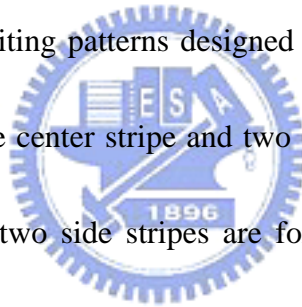
The sample used for this study was a 2  $\mu\text{m}$  thick n-GaN layer grown on a c-plane sapphire substrate by metalorganic chemical vapor deposition (MOCVD). The resist stack consisted of a low-sensitivity 495k PMMA layer of 120 nm thickness in the bottom and a high-sensitivity copolymer EL 12.5 PMMA-MAA (680 nm) on the top. After the first PMMA layer was coated, the sample was baked at 180  $^{\circ}\text{C}$  for 90 sec. Then the second PMMA-MAA layer was coated followed by another bake at 150  $^{\circ}\text{C}$  for 90 sec. The e-beam acceleration voltage used for this study was 15 kV. After e-beam exposure, the developer MIBK : IPA (1:3) was used to remove the exposed area. The developer temperature was kept at 25 $^{\circ}\text{C}$ . After development, the sample surface was treated with UV Ozone for 2 min. and then dipped in HCl: H<sub>2</sub>O (1:1)

solution for 60 sec to remove the residual resist. Metal deposition of Ni (20 nm)/Au (300 nm) was performed using e-beam evaporation. The temperature control during the metal deposition process is also important due to the poor heat tolerance of both PMMA and copolymer PMMA-MAA. Finally, the sample was soaked in acetone for metal lift-off.

### **5-3 Results and discussion**

#### **5-3-1 Writing pattern design**

Figure 5-1 shows the writing patterns designed to fabricate narrow T-gate. The writing pattern consists of one center stripe and two side stripes. The center stripe is for foot exposure, while the two side stripes are for the head exposure. The main design parameters include the width of the center stripe, the width of the side stripe and the spacing between them.

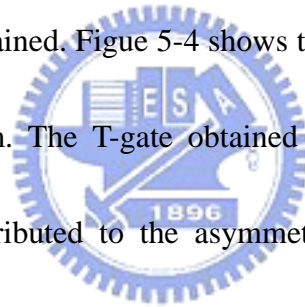


#### **5-3-2 40 nm narrow T-gate fabrication**

The writing pattern, shown in Fig. 5-1, consists of a 50 nm wide center stripe for foot exposure and two 75 nm wide side stripes for head exposure. A systematic evaluation of the footwidth as a function of the e-beam dose for the center stripe was carried out. The dependence is shown in Fig. 5-2. The footwidth increases linearly



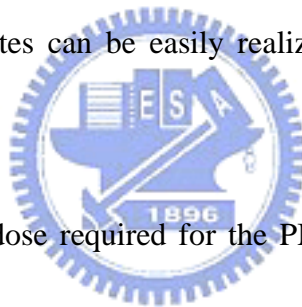
with the dose. The minimum dimension obtained is 40 nm. The average width is around 50 nm. The central dose required for the minimum footwidth is  $140 \mu\text{C}/\text{cm}^2$ , while a much lower dose of around  $40 \mu\text{C}/\text{cm}^2$  is used for the side patterns. These doses were optimized for the best result. After development, very good undercut profiles and narrow foot openings with dimensions less than 100 nm were obtained. The SEM microphotograph of a developed gate pattern is shown in Fig. 5-3. The resist profile shows a very nice undercut, better than those obtained by a conventional 50 kV e-beam lithography systems. After Ni/Au deposition and the lift-off process, very narrow T-gates were obtained. Figure 5-4 shows the SEM picture of a T-gate with a gate length of only 40 nm. The T-gate obtained shows a slightly asymmetrical feature, which is mainly attributed to the asymmetrical deformation of the resist profile during the metal deposition process.



In general, an electron-beam lithography system with a high acceleration voltage is preferred for the fabrication of narrow gates because of its smaller beam spot size and the much reduced forward scattering effect. Maile reported that the energy density profiles for low-energy e-beams broaden markedly with the increase of penetration depth [3]. For 20 keV exposures on a 600 nm and 800 nm bi-layer resist stack, the energy density profiles broaden to around 100 nm and 170 nm, respectively, at the bottom of the resist. It is therefore very difficult to fabricate sub 100 nm T-gates with

a thick multi-layer resist stack and an acceleration voltage below 20 kV. The reasons that we were able to achieve a very narrow gate with a very low-energy e-beam on a thick resist are probably from two sources. First, the backscattering of the e-beam from GaN is probably less than that from GaAs. Second, which is more important, is the design of the writing pattern.

We found that the exposure of the two side stripes significantly influences the final e-beam's energy density profile and the minimum footwidth achieved. If the gap spacing between the center stripe and side stripes is small compared to the width of the stripes, sub 100 nm T-gates can be easily realized even when the acceleration voltage is small.



We also found that the dose required for the PMMA/copolymer PMMA-MAA resist stack on GaN is much lower than that for conventional GaAs substrates. For the fabrication of T-gates on GaAs using a 50 kV e-beam, the dose needed is typically around  $600 \mu\text{C}/\text{cm}^2$  for a 100 nm footwidth and  $200 \mu\text{C}/\text{cm}^2$  for a 500 nm head. The dose ratio between the head and the foot is around 3-4 [6]. In this work, however, the central dose for the 50-200 nm footwidth ranges from 140 to  $200 \mu\text{C}/\text{cm}^2$  and the side exposure dose is around  $40 \mu\text{C}/\text{cm}^2$ . The lower dose needed here is due to the use of a lower acceleration voltage. Similar observations were also found in a previous report [12]. The dose ratio of the center to side exposures is around 3-5, which is slightly

higher than the case in GaAs using a 50 kV accelerating voltage. The higher dose ratio can reduce the influence of the exposure of the top copolymer PMMA-MAA on the bottom PMMA exposure and thus contributes to the footwidth control.

#### **5-4 Conclusion**

A new e-beam lithography process was developed for sub 100 nm T-gate formation on GaN. The e-beam exposure condition on a GaN substrate was found to be quite different from that on GaAs. We experimentally demonstrated that the fabrication of sub 100 nm T-gate on GaN using 15 keV electron beam energy is practical. This is due to the much reduced forward scattering effect in the PMMA/copolymer PMMA-MAA resist stack on GaN. With a proper writing pattern design, the forward scattering effect with a lower accelerating voltage can be significantly reduced. Moreover, with the lower accelerating voltage used, much lower doses for both the central and side exposures are needed, as compared to the case using a high accelerating voltage.

## References

- [1] N. Samoto, Y. Makino, K. Onda E. Mizuki and T. Itoh, *J. Vac. Sci. Technol.* B8 (1990) 1335.
- [2] K. Nummila, M. Tong, A. Ketterson and I. Adesida, *J. Vac. Sci. Technol.* B9 (1991) 2870.
- [3] B. E Maile, *J. Vac. Sci. Technol.* B11 (1993) 2502.
- [4] N. Samoto, I. Miura, Y. Makino and K. Yamanoguchi, *J. Vac. Sci. Technol.* B12 (1994) 3673.
- [5] A. S. Wakita, C. Y. Su, H. Rohdin, H. Y. Liu, A. Lee, J. Seeger and V. M. Robbibs, *J. Vac. Sci. Technol.* B13 (1995) 2725.
- [6] Y. Chen, D. Macintyre and S. Thoms, *J. Vac. Sci. Technol.* B17 (1999) 2507.
- [7] T. Suemitsu, T. Ishii, H. Yokoyama, T. Enoki, *Jpn. J. Appl. Phys.* 38 (1999) L154.
- [8] H. M. Lee, E. Y. Chang, S. H. Chen and C. Y. Chang, *Jpn. J. Appl. Phys.* 41 (2002) L1508.
- [9] Y. Chen, D. Edgar, X. Li, D. Macintyre and S. Thoms, *J. Vac. Sci. Technol.* B18 (2000) 3521.
- [10] Y. Chen, D. Macintyre and S. Thoms, *Microelectron. Eng.* 57 (2001) 939.
- [11] L. E Ocola, D. M. Tennant and P. D. Ye, *Microelectron. Eng.* 67 (2003) 104.

[12] P. A. Peterson, Z. J. Radzinski, S. A. Schwalm and P. E. Russell, J. Vac. Sci. Technol. B10 (1992) 3088.



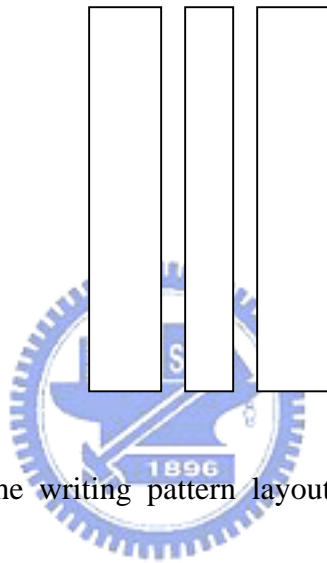


Fig. 5-1 The schematic of the writing pattern layout designed for narrow T-gate fabrication.

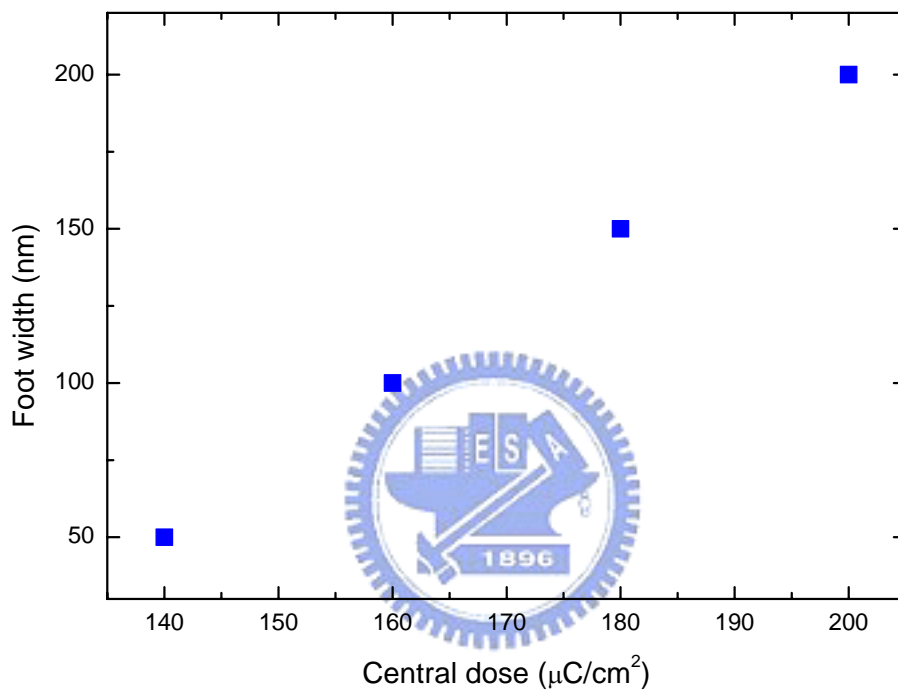


Fig. 5-2 The average footwidth of narrow T-gates as a function of the central dose.

The average minimum footwidth is 50 nm.

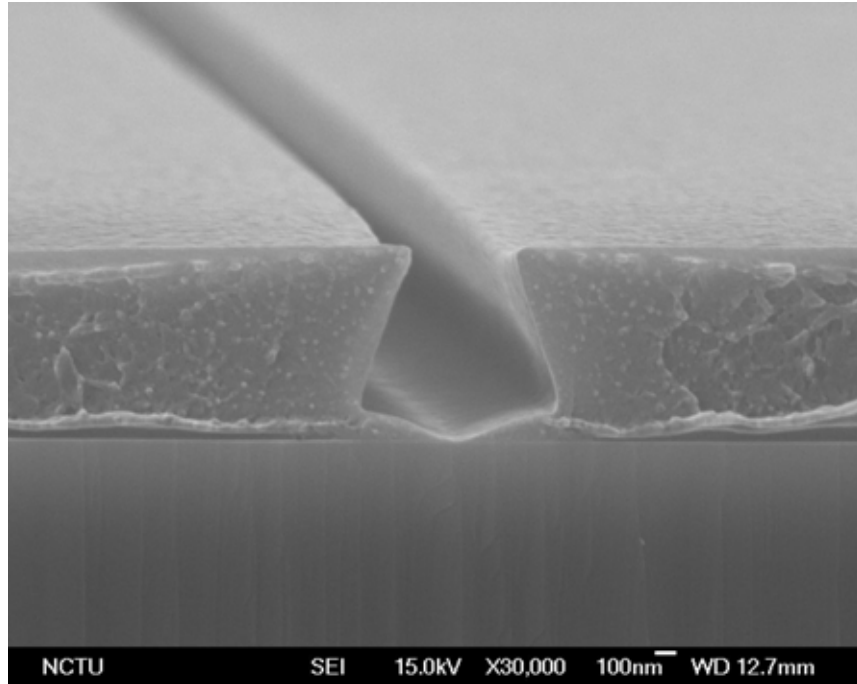


Fig. 5-3 The resist profile after development. A very good undercut profile and a narrow foot opening with dimensions of about 60 nm were obtained.

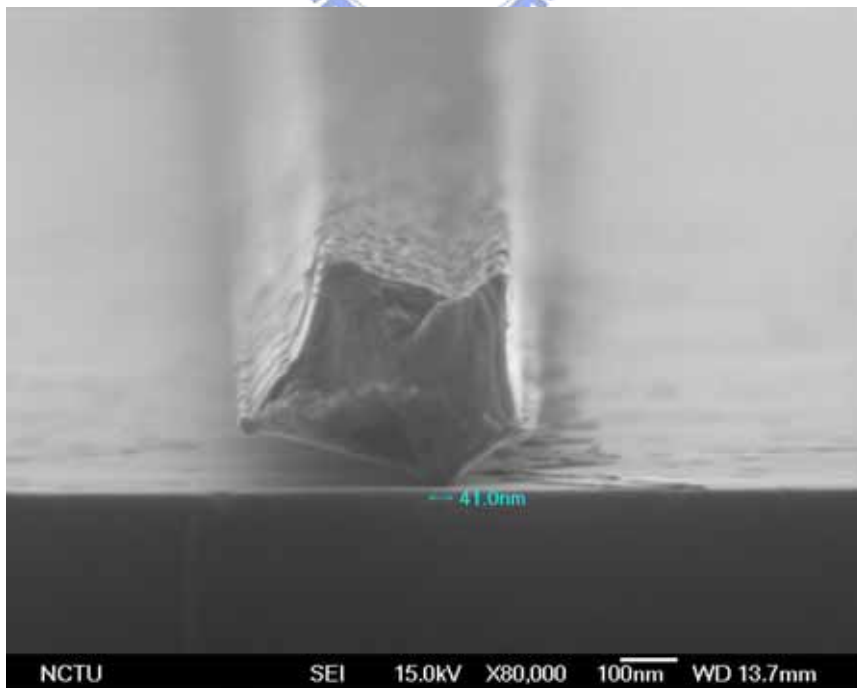
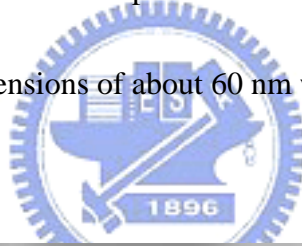


Fig. 5-4 A 40 nm narrow T-gate on a GaN substrate after metal deposition and lift-off.



## Chapter 6

### Polarization effect in AlGa<sub>N</sub>/Ga<sub>N</sub>

#### heterostructure Field Effect Transistors

##### 6-1 Introduction

GaN-based heterostructure field-effect transistors (HFETs) are promising candidates for high-temperature and high-power applications at high frequencies due to their superior material properties, such as high breakdown field, high saturation velocity and excellent thermal stability [1-3]. In particular, the spontaneous and piezoelectric polarization effects play a significant role in the device power performance. The strong polarization effect in the undoped AlGa<sub>N</sub>/Ga<sub>N</sub> heterostructures can produce two-dimensional electron gas (2DEG) of around  $1 \times 10^{13}$  cm<sup>-2</sup> at the AlGa<sub>N</sub>/Ga<sub>N</sub> interface [4-8]. Such a high electron concentration obtained in the undoped AlGa<sub>N</sub>/Ga<sub>N</sub> heterostructures is much higher than that available in the conventional AlGaAs/GaAs or other material systems. If additional modulation doping is used, even higher 2DEG concentration can be achieved in the AlGa<sub>N</sub>/Ga<sub>N</sub> heterostructures. In this work, we systematically investigated the polarization effect in the AlGa<sub>N</sub>/Ga<sub>N</sub> heterostructure FETs. Several structures including undoped and modulation-doped structures were designed. We compared the surface morphology

and the electron transport properties of the structures with different Al compositions, different AlGaN thicknesses and modulation doping. In addition, we fabricated AlGaN/GaN HFETs to further observe the polarization effect on the device characteristics. As a result, very high 2DEG concentration can be obtained in the  $\text{Al}_{0.3}\text{Ga}_{0.7}\text{N}/\text{GaN}$  heterostructures. Furthermore, the undoped and modulation-doped  $\text{Al}_{0.3}\text{Ga}_{0.7}\text{N}/\text{GaN}$  HFETs exhibited very high device output current.

## 6-2 Experiment

Several structures including three undoped structures and one modulation-doped structure were grown by metalorganic chemical vapor deposition (MOCVD) on c-plane sapphire substrates, as shown in Figs. 6-1 to 6-4. Sample No. 1 consists of a 3  $\mu\text{m}$  undoped GaN buffer layer and an 18 nm undoped AlGaN cap layer with Al composition of 0.17. Sample No. 2 consists of a 3  $\mu\text{m}$  undoped GaN buffer layer and a 50 nm undoped AlGaN cap layer with Al mole fraction of 0.17. Sample No. 3 consists of a 3  $\mu\text{m}$  undoped GaN buffer layer and a 28 nm undoped AlGaN cap layer with Al composition of 0.3. Sample No. 4 consists of a 3  $\mu\text{m}$  undoped GaN buffer layer and a 3 nm undoped AlGaN spacer, a 20 nm Si-doped AlGaN layer with a doping concentration of  $5 \times 10^{18} \text{ cm}^{-3}$  and a 5 nm undoped AlGaN cap layer, where the Al composition is 0.3 for all AlGaN layer.

Device fabrication process began with mesa isolation, followed by Ohmic contact and narrow T-gate fabrication. Mesa patterns for device active regions were defined by photolithography and dry etch with  $\text{Cl}_2/\text{Ar}$  plasma using an inductive coupled plasma (ICP) system. Prior to contact metal deposition, the samples were treated by Ar plasma. Contact metal, Ti/Al/Ti/Au (200/1500/450/550 Å), was then deposited and lifted-off to form the contact pads. The samples were annealed at 750°C for 30 s in  $\text{N}_2$  gas ambient. The source-drain spacing is 2  $\mu\text{m}$  for all samples. In the narrow T-gate fabrication, the resist stack consisted of a low-sensitivity 495k PMMA layer of 120 nm thickness in the bottom and a high-sensitivity copolymer EL 12.5 PMMA-MAA (680 nm) on the top. The e-beam acceleration voltage used here was 15 kV [9]. Metal deposition of Ni (20 nm)/Au (300 nm) was performed using e-beam evaporation.

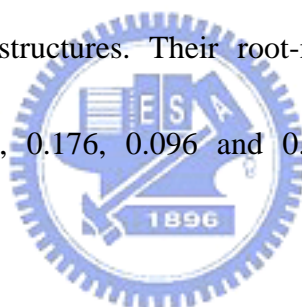
The surface morphology of the samples was observed using the atomic force microscope (AFM) operated in contact mode. Hall effect measurements with Van der Pauw geometry were performed to characterize the two-dimensional electron gas (2DEG) concentration and electron mobility in the temperature range from 100K to 500K. Capacitance-voltage (C-V) profiling technique using fat FET test patterns was employed to observe the carrier distribution at room temperature. Device dc characterizations and small-signal measurement was performed using the HP4142 dc

analyzer and the Anritsu37397 vector network analyzer (VNA).

### **6-3 Results and discussion**

#### **6-3-1 Surface morphology**

Several structures were designed to observe the polarization effect in AlGa<sub>0.2</sub>N/GaN heterostructures. The structures used in this work include three undoped structures and one modulation-doped structure, as shown in Figs. 6-1 to 6-4. Figures 6-5 to 6-8 show the AFM images of their surface morphologies. As a whole, all samples exhibited step-like structures. Their root-mean-square (RMS) values of surface roughness are 0.176, 0.176, 0.096 and 0.131 nm for sample No. 1-4, respectively.



Usually several problems arise in the growth of AlGa<sub>0.2</sub>N [10]. It is not easy to obtain atomically smooth surfaces, especially in the case of higher Al composition. In addition, the local variation in the alloy composition has been observed. As the Al mole fraction is above 0.2, the strain in the AlGa<sub>0.2</sub>N due to the lattice mismatch between the AlGa<sub>0.2</sub>N and GaN may cause the formation of structural defects and transition into the island growth mode, and will also influence the electrical properties of heterostructures. The surface roughness results obtained are around 0.15 nm, suggesting very smooth surface and thus good crystal quality of AlGa<sub>0.2</sub>N epitaxial layer.

Similar results are also observed in [10].

### 6-3-2 Electron transport properties

Figure 6-9 shows a comparison on the 2DEG concentration for the undoped samples with different Al compositions. Both structures showed nearly constant electron concentrations in the measured temperature range. The sample with Al composition of 0.17 showed an electron concentration of around  $3.8 \times 10^{12} \text{ cm}^{-2}$ , while the sample with Al composition of 0.3 exhibited a higher electron concentration of around  $1 \times 10^{13} \text{ cm}^{-2}$ . Apparently the samples with a higher Al composition have a higher 2DEG concentration formed at the AlGa<sub>x</sub>N/GaN interface. The reason for the results obtained is the strong spontaneous and piezoelectric polarization effect. As the Al mole fraction of the AlGa<sub>x</sub>N barriers increases, both the spontaneous and piezoelectric polarizations increase. Thus more 2DEG was generated to compensate the increase in the polarization induced sheet charge concentration.

Figure 6-10 shows a comparison on the electron mobility for the undoped samples with different Al compositions. The sample with Al composition of 0.17 showed a room-temperature mobility of  $1170 \text{ cm}^2/\text{Vs}$ . The sample with Al composition of 0.3 showed a slightly lower room-temperature mobility of  $1100 \text{ cm}^2/\text{Vs}$ . Both samples showed comparable electron mobility as the temperature is

above room temperature since the phonon scattering dominates the electron transport at elevated temperatures. As the temperature was reduced, the electron mobility improved dramatically as a result of the reduction of phonon scattering. At 100K, a much higher electron mobility of  $6240 \text{ cm}^2/\text{Vs}$  was obtained for the sample with Al mole fraction of 0.17, while a moderately high electron mobility of  $3030 \text{ cm}^2/\text{Vs}$  was obtained for the sample with Al composition of 0.3. Similar results were also observed in a previous report [11].

Apparently, a large difference in the electron mobility at 100K was observed for the two samples. The observed low temperature mobility value for the sample with Al composition of 0.3 is much lower than that for the sample with Al composition of 0.17. The main scattering mechanisms at low temperatures include ionized impurities and interface roughness. In general, the higher electron concentration formed at the AlGa<sub>N</sub>/Ga<sub>N</sub> interface can improve the screening of ionized impurities [11-12]. So the sample with Al mole fraction of 0.3 should have higher electron mobility. However, the results obtained here do not agree with such statements, thus it is obvious that the ionized impurity scattering is not the dominated scattering mechanism at low temperature. On the other hand, as the electron concentration in the channel increases, the carrier distribution becomes closer to the interface and thus the electron transport becomes more sensitive to the interface roughness [11-12]. Therefore for the sample

with higher Al composition, the lower electron mobility at low temperature is mainly attributed to the interface roughness scattering.

Figure 6-11 shows a comparison on the electron concentration for the undoped samples with different AlGa<sub>N</sub> thickness. Both structures exhibited nearly constant electron concentrations in the measured temperature range. The sample with AlGa<sub>N</sub> thickness of 18 nm showed an electron concentration of around  $3.8 \times 10^{12} \text{ cm}^{-2}$ , while the sample with AlGa<sub>N</sub> thickness of 50 nm showed a slightly higher electron concentration of around  $4 \times 10^{12} \text{ cm}^{-2}$ .

It is apparent that the samples with a thicker AlGa<sub>N</sub> layer show slightly higher 2DEG concentration formed at the AlGa<sub>N</sub>/Ga<sub>N</sub> interface. As the AlGa<sub>N</sub> thickness increases, the strain relaxation in the AlGa<sub>N</sub> may lead to the reduction of piezoelectric polarization. Based on the calculations of the critical thickness of hexagonal AlGa<sub>N</sub> grown on relaxed Ga<sub>N</sub> using the Matthews and Blakeslee, and Fischer *et al.* models [8], for a typical AlGa<sub>N</sub> thickness of about 30 nm, strain relaxation and thus the reduction in piezoelectric polarization has to be expected for Al composition above 0.14 and 0.25, respectively. Following this argument, for a larger AlGa<sub>N</sub> thickness of 50nm, strain relaxation would be expected for lower Al compositions of around 0.1 and 0.17, respectively. However, the actual strain relaxation was observed for barrier thickness well above the calculated critical thickness over a wide range of Al composition. For

the AlGaN barriers with Al composition of 0.17 and 0.3, the critical AlGaN thicknesses are around 700 nm and 60 nm, respectively, which are all much larger than that used in this work. Also, the observed 2DEG concentration increases with AlGaN barrier thickness. It is therefore that no obvious strain relaxation was observed for the sample with 50 nm  $\text{Al}_{0.17}\text{Ga}_{0.83}\text{N}$  cap layer. Similar results were obtained in a previous report [11].

Figure 6-12 shows a comparison on the electron mobility for undoped samples with different AlGaN thickness. The sample with AlGaN thickness of 18 nm showed a room-temperature mobility of  $1170 \text{ cm}^2/\text{Vs}$ . The sample with AlGaN thickness of 50 nm showed a slightly lower room-temperature mobility of  $1130 \text{ cm}^2/\text{Vs}$ . Both samples showed comparable electron mobility as the temperature is above room temperature since the phonon scattering dominates the electron transport at elevated temperatures. As the temperature was reduced, the electron mobility improved significantly as a result of the reduction of phonon scattering. At 100K, a much higher electron mobility of  $6240 \text{ cm}^2/\text{Vs}$  was obtained for the sample with AlGaN thickness of 18 nm, while a moderately high electron mobility of  $4080 \text{ cm}^2/\text{Vs}$  was obtained for the sample with AlGaN thickness of 50 nm. Similar to the case of the sample with a higher Al composition, the lower low temperature electron mobility observed in the sample with thicker AlGaN layer is mainly due to interface roughness scattering. Similar results



were also observed in previous reports [11].

Figure 6-13 shows the temperature dependence of electron concentration of the undoped and modulation-doped structures, where the Al composition is 0.3. For the undoped structure the sheet charge concentration of 2DEG is around  $1 \times 10^{13} \text{ cm}^{-2}$  and is nearly constant over the measured temperature range. For the modulation-doped structure, the electron concentration is temperature dependent. The sheet charge concentration increases from  $1.15 \times 10^{13} \text{ cm}^{-2}$  at 100K to  $1.33 \times 10^{13} \text{ cm}^{-2}$  at 500K.

At very low temperatures, because of the freeze-out of the Si donors in the AlGa<sub>0.3</sub>N layer, the channel conduction of the modulation-doped structure markedly decreases. As the temperature increases, the thermal activation process starts to release gradually the frozen electrons and thus the measured sheet carrier density increases.

Figure 6-14 shows the temperature dependence of the electron mobility of the two structures. As a whole, the electron mobilities of the two structures decrease with temperature as a result of the increased phonon scattering. The undoped structure has a low temperature electron mobility of  $3030 \text{ cm}^2/\text{Vs}$  at 100K and room-temperature electron mobility of  $1100 \text{ cm}^2/\text{Vs}$ . The modulation-doped structure has an electron mobility of  $2610 \text{ cm}^2/\text{Vs}$  at 100K and a room-temperature mobility of  $953 \text{ cm}^2/\text{Vs}$ . The lower mobility for the modulation-doped structure is due to the additional ionized

impurity scattering associated with the Si donors and possible parallel conduction in the doped AlGaN layer. As the temperature increased above 450K, the two structures showed comparable electron mobility. At 500K the mobilities are 537 cm<sup>2</sup>/Vs and 529 cm<sup>2</sup>/Vs for the undoped and modulation-doped structure, respectively. This is due to the enhanced phonon scattering that dominates over impurity scattering at high temperatures. Similar results were also observed in a previous report [13].

Figures 6-15 and 6-16 show the carrier distribution of the undoped and modulation-doped samples with Al composition of 0.3 measured by the C-V profiling technique. Test patterns with a dimension of 50 μm (gate length) by 100 μm (device width) were used. Carrier profiles were obtained using the junction capacitance approximation. As can be seen, most carriers are located at the AlGaN/GaN interface. The undoped sample exhibited a very narrow carrier distribution, where the peak electron concentration of around  $6.5 \times 10^{19} \text{ cm}^{-3}$  is near the interface. In contrast, the modulation-doped sample exhibited a wider carrier distribution. Its peak carrier concentration, around  $1.2 \times 10^{19} \text{ cm}^{-3}$ , is also near the AlGaN/GaN interface. In addition, the doping concentration of around  $5 \times 10^{18} \text{ cm}^{-3}$  in the Si-doped AlGaN layer was also clearly observed.

### 6-3-3 Device characteristics

The devices with the gate length of  $0.15\ \mu\text{m}$  and the width of  $75\ \mu\text{m}$  were used to further observe the polarization effect on the device characteristics of AlGaIn/GaN HFETs. The scanning electron microscope (SEM) images of the undoped  $\text{Al}_{0.3}\text{Ga}_{0.7}\text{N}/\text{GaN}$  HFET with a gate length of  $0.15\ \mu\text{m}$  are shown in Fig. 6-17. The contact resistance of  $0.59\ \text{ohm-mm}$  by the transmission line measurement (TLM) was obtained for the undoped  $\text{Al}_{0.3}\text{Ga}_{0.7}\text{N}/\text{GaN}$  HFET. Figure 6-18 shows the current-voltage characteristics of the undoped  $\text{Al}_{0.3}\text{Ga}_{0.7}\text{N}/\text{GaN}$  HFET. This undoped device exhibited good dc characteristics. The maximum drain current of around  $700\ \text{mA/mm}$  was obtained at  $V_{\text{gs}} = 2\ \text{V}$  and  $V_{\text{ds}} = 7\ \text{V}$ . As larger  $V_{\text{ds}}$  were applied, negative I-V slope was observed, which is known as the self-heating effect [14-15].

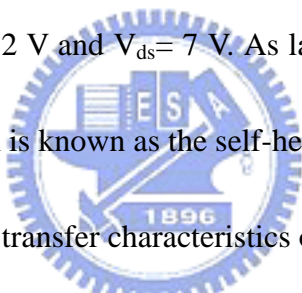


Figure 6-19 shows the dc transfer characteristics of the undoped  $\text{Al}_{0.3}\text{Ga}_{0.7}\text{N}/\text{GaN}$  HFET measured at  $V_{\text{ds}} = 5\ \text{V}$ . In particular, the measured extrinsic transconductance showed small variations over a wide gate bias range, which indicated a good linearity of the undoped device. This undoped device showed the maximum extrinsic transconductance,  $g_{\text{m, max}}$ , of  $113\ \text{mS/mm}$  at  $V_{\text{gs}} = -3.8\ \text{V}$ . The threshold voltage is around  $-7\ \text{V}$ . The source resistance and the intrinsic transconductance are  $3.4\ \text{ohm-mm}$  and  $183\ \text{mS/mm}$ , respectively.

Figure 6-20 shows the breakdown characteristics of the undoped  $\text{Al}_{0.3}\text{Ga}_{0.7}\text{N}/\text{GaN}$  HFET. The breakdown voltage is defined as the voltage where the

gate current  $> 1\text{mA/mm}$ . The device exhibited a very high breakdown voltage of above 100 V. Figure 6-21 shows the forward Schottky I-V characteristics of the undoped  $\text{Al}_{0.3}\text{Ga}_{0.7}\text{N/GaN}$  HFET. The calculated ideality factor is around 2, which is slightly large. Thus the Schottky barrier height could not be extracted correctly.

Figure 6-22 shows the small-signal characteristics of the undoped  $\text{Al}_{0.3}\text{Ga}_{0.7}\text{N/GaN}$  HFET. As the undoped device is biased at  $V_{\text{ds}}= 6\text{ V}$  and  $V_{\text{gs}}= -3.5\text{ V}$ , it exhibited current gain cut-off frequency ( $f_{\text{T}}$ ) of 32 GHz and the maximum frequency of oscillation ( $f_{\text{max}}$ ) of around 64 GHz.

Figure 6-23 shows the current-voltage characteristics of the modulation-doped  $\text{Al}_{0.3}\text{Ga}_{0.7}\text{N/GaN}$  HFET. This modulation-doped device also exhibited good dc characteristics. Very high maximum drain current of around 1040 mA/mm was obtained at  $V_{\text{gs}}= 2\text{ V}$  and  $V_{\text{ds}}= 7\text{ V}$ . As larger  $V_{\text{ds}}$  were applied, the self-heating effect was also clearly observed. Figure 6-24 shows the dc transfer characteristics of the modulation-doped  $\text{Al}_{0.3}\text{Ga}_{0.7}\text{N/GaN}$  HFET measured at  $V_{\text{ds}}= 4\text{ V}$ . As can be seen, the measured extrinsic transconductance showed larger changes on the gate bias. This modulation-doped device showed the maximum extrinsic transconductance,  $g_{\text{m, max}}$ , of 150 mS/mm at  $V_{\text{gs}}= -7\text{ V}$ . The threshold voltage is around  $-9\text{ V}$ . The source resistance and the intrinsic transconductance are 2.7 ohm-mm and 271 mS/mm, respectively.

Figure 6-25 shows the breakdown characteristics of the modulation-doped

$\text{Al}_{0.3}\text{Ga}_{0.7}\text{N}/\text{GaN}$  HFET. The breakdown voltage is defined as the voltage where the gate current  $> 1\text{mA}/\text{mm}$ . The device exhibited a moderately high breakdown voltage of above 53 V. Figure 6-26 shows the forward Schottky I-V characteristics of the modulation-doped  $\text{Al}_{0.3}\text{Ga}_{0.7}\text{N}/\text{GaN}$  HFET. The ideality factor is somewhat large and thus the Schottky barrier height could not be extracted correctly.

Figure 6-27 shows the small-signal characteristics of the modulation-doped  $\text{Al}_{0.3}\text{Ga}_{0.7}\text{N}/\text{GaN}$  HFET. The modulation-doped device is operated at  $V_{\text{ds}}= 6\text{ V}$  and  $V_{\text{gs}}= -6\text{ V}$ . It exhibited the current gain cut-off frequency ( $f_{\text{T}}$ ) of around 75 GHz and the maximum frequency of oscillation ( $f_{\text{max}}$ ) of around 90 GHz.

From the above results, the undoped device exhibited a high drain current of  $\sim 700\text{ mA}/\text{mm}$ . Such a high drain current obtained is obviously attributed to the strong spontaneous and piezoelectric polarization effect in the high Al content undoped  $\text{AlGaIn}/\text{GaIn}$  heterostructures. The modulation-doped device exhibited an even higher drain current of  $\sim 1040\text{ mA}/\text{mm}$  due to the additional modulation doping. Thus it is apparent that the polarization effect plays a crucial role in the device output current. In addition, high breakdown voltages were also observed for the two devices as a result of the high breakdown field of nitride. The undoped device showed a very high breakdown voltage of above 100 V. The modulation-doped device showed a moderately high breakdown voltage of around 53 V. Figure 6-28 shows the gate

length dependence of the cut-off frequency for the undoped and modulation-doped  $\text{Al}_{0.3}\text{Ga}_{0.7}\text{N}/\text{GaN}$  HFETs. As the gate length was reduced, both devices show remarkable improvement in the cut-off frequency. The  $0.15\ \mu\text{m}$  undoped device showed a  $f_T$  of 32 GHz and a  $f_{\text{max}}$  of 64 GHz, while the  $0.15\ \mu\text{m}$  modulation-doped device showed a even higher  $f_T$  of 75 GHz and a  $f_{\text{max}}$  of 90 GHz. The lower  $f_T$  and  $f_{\text{max}}$  for the undoped device is mainly due to its larger parasitic source resistances. Therefore, these excellent characteristics obtained here including high drain currents, high breakdown voltages and high operating frequencies experimentally demonstrate that  $\text{AlGaN}/\text{GaN}$  HFETs are very excellent high power devices operating at high frequencies.



#### **6-4 Conclusion**

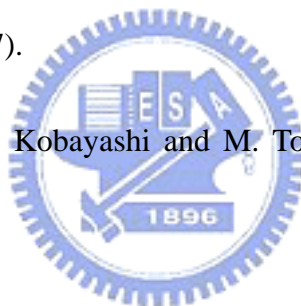
We systematically investigated the polarization effect in the  $\text{AlGaN}/\text{GaN}$  HFETs. The measured surface morphology of the  $\text{Al}_{0.3}\text{Ga}_{0.7}\text{N}/\text{GaN}$  heterostructures showed very smooth surface. The undoped structure showed a very high 2DEG concentration formed at the  $\text{Al}_{0.3}\text{Ga}_{0.7}\text{N}/\text{GaN}$  interface as a result of the strong spontaneous and piezoelectric polarization. Even higher 2DEG concentration can be achieved by additional modulation doping. The interface roughness dominated the electron scattering mechanism at low temperature, while the phonon scattering dominated the

electron transport at elevated temperatures. Both the undoped and modulation-doped devices exhibited very high drain current. Thus the polarization effect plays a crucially important role in the high power performance of AlGaIn/GaN HFETs. In addition, both devices exhibited high breakdown voltages and excellent small-signal characteristics. These excellent device characteristics obtained experimentally demonstrated that AlGaIn/GaN HFETs are indeed very excellent high power devices operating at high frequencies.



## References

- [1] S. Keller, Y. F. Wu, G. Parish, N. Ziang, J. J. Xu, B. P. Keller, S. P. DenBaars and U. K. Mishra, IEEE Trans. Electron Devices, **48**, 552 (2001).
- [2] L. F. Eastman and U. K. Mishra, IEEE spectrum, 28, May (2002).
- [3] U. K. Mishra, P. Parikh and Y. F. Wu, Proceeding of the IEEE **90**, 1022 (2002).
- [4] P. M. Asbeck, E. T. Yu, S. S. Lau, G. J. Sullivan, J. Van Hove and J. Redwing, Electron. Lett., **33**, 1230 (1997).
- [5] E. T. Yu, G. J. Sullivan, P. M. Asbeck, C. D. Wang, D. Qiao and S. S. Lau, Appl. Phys. Lett., **71**, 2794 (1997).
- [6] N. Maeda, T. Nishida, N. Kobayashi and M. Tomizawa, Appl. Phys. Lett., **73**, 1856 (1998).
- [7] O. Ambacher, J. Smart, J. R. Shealy, N. G. Weimann, K. Chu, M. Murphy, W. J. Schaff, L. F. Eastman, R. Dimitrova, L. Wittmer, M. Stutzmann, W. Rieger and J. Hilsenback, J. Appl. Phys., **85**, 3222 (1999).
- [8] O. Ambacher, B. Foutz, J. Smart, J. R. Shealy, N. G. Weimann, K. Chu, M. Murphy, A. J. Sierakowski, W. J. Schaff, L. F. Eastman, R. Dimitrova, A. Mitchell and M. Stutzmann, J. Appl. Phys., **87**, 334 (2000).
- [9] C. C. Lee, C. P. Lee and C. T. Kuo, submitted to Microelectronics engineering for publication.





- [10] S. Keller, G. Parish, P. T. Fini, S. Heikman, C. H. Chen, N. Zhang, S. P. DenBaars, U. K. Mishra and Y. F. Wu, *J. Appl. Phys.*, **86**, 5850 (1999).
- [11] I. P. Smorchkova, C. R. Elsass, J. P. Ibbetson, R. Vetury, B. Heying, P. Fini, E. Haus, S. P. DenBaars, J. S. Speck and U. K. Mishra, *J. Appl. Phys.*, **86**, 4520 (1999).
- [12] Y. Zhang and J. Singh, *J. Appl. Phys.*, **85**, 587 (1999).
- [13] N. Maeda, K. Tsubaki, T. Saitoh and N. Kobayashi, *Appl. Phys. Lett.* **79**, 1634 (2001).
- [14] Y. F. Wu, B. P. Keller, S. Keller, D. Kapolnek, P. Kozodoy, S. P. DenBaars and U. K. Mishra, *Solid State Electron.*, **41**, 1569 (1997).
- [15] R. Gaska, J. Yang, A. Osinsky, M. F. Khan and M. S. Shur, *IEDM Tech. Dig.*, 565 (1997).

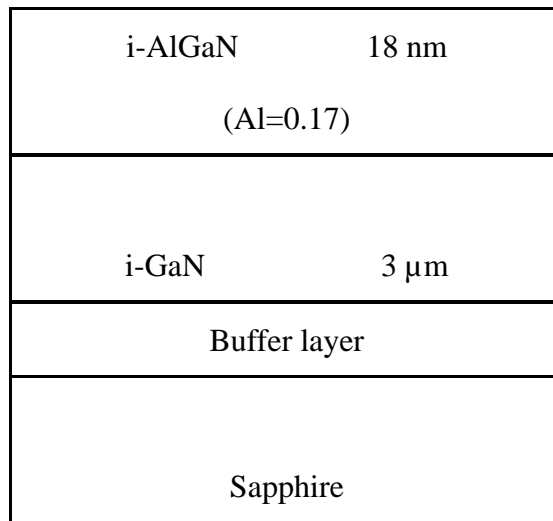


Fig. 6-1 The schematic of undoped structure (sample No. 1), where Al composition is 0.17 and the top AlGaN layer thickness is 18 nm.

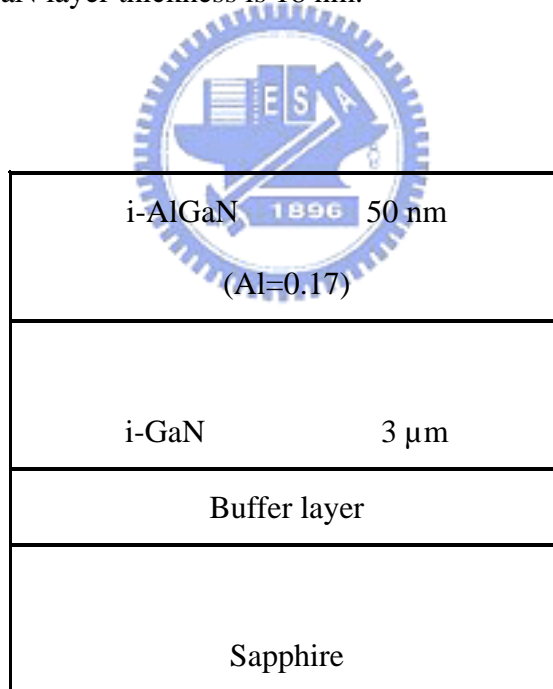
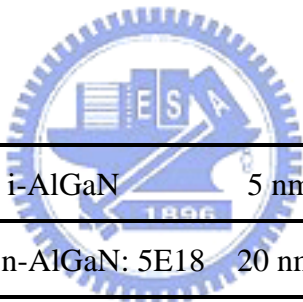


Fig. 6-2 The schematic of undoped structure (sample No. 2), where Al composition is 0.17 and the top AlGaN layer thickness is 50 nm.

i-AlGaN (Al=0.3)	28 nm
i-GaN	3 μm
Buffer layer	
Sapphire	

Fig. 6-3 The schematic of undoped structure (sample No. 3), where Al composition is 0.3 and the top AlGaN layer thickness is 28 nm.



i-AlGaN	5 nm
n-AlGaN: 5E18	20 nm
i-AlGaN	3 nm
i-GaN	3 μm
Buffer layer	
Sapphire	

Fig. 6-4 The schematic of modulation-doped structure (sample No. 4), where Al composition is 0.3 and the AlGaN layer consists of a 3 nm undoped AlGaN spacer, a 20 nm AlGaN with Si doping concentration of  $5 \times 10^{18} \text{ cm}^{-3}$  and a 5 nm undoped AlGaN cap layer.

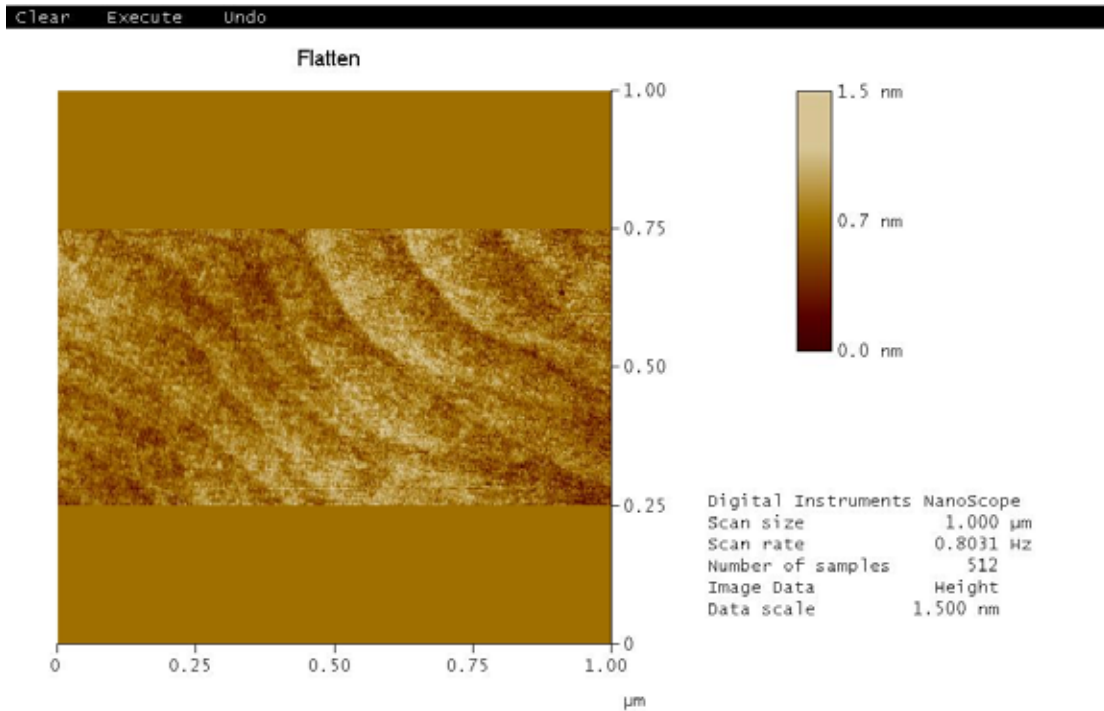


Fig. 6-5 The surface morphology of undoped structure (sample No. 1), where Al composition is 0.17 and the top AlGa<sub>N</sub> layer thickness is 18 nm.

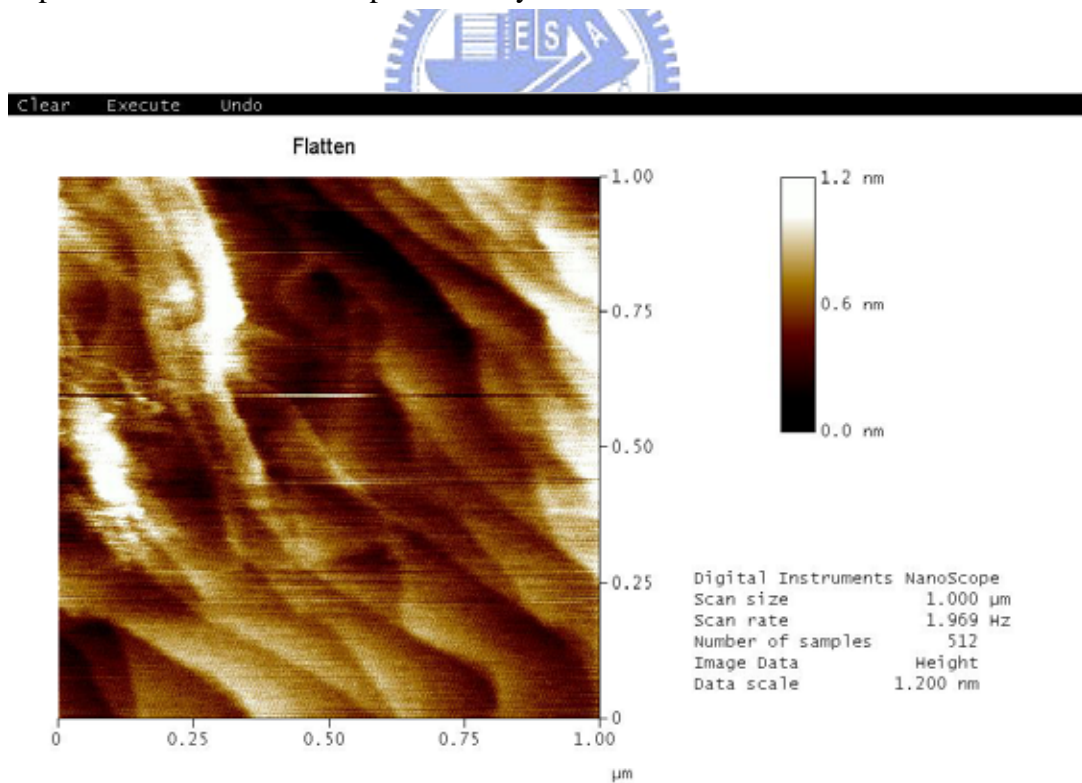


Fig. 6-6 The surface morphology of undoped structure (sample No. 2), where Al composition is 0.17 and the top AlGa<sub>N</sub> layer thickness is 50 nm.

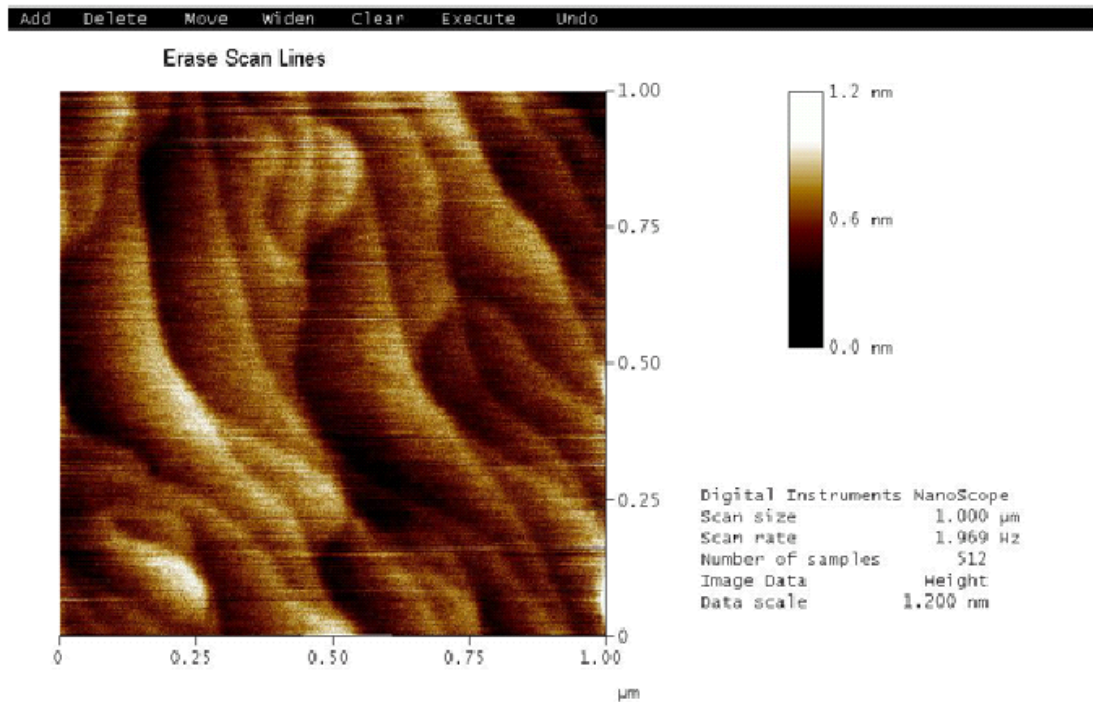


Fig. 6-7 The surface morphology of undoped structure (sample No. 3), where Al composition is 0.3 and the top AlGa<sub>N</sub> layer thickness is 28 nm.

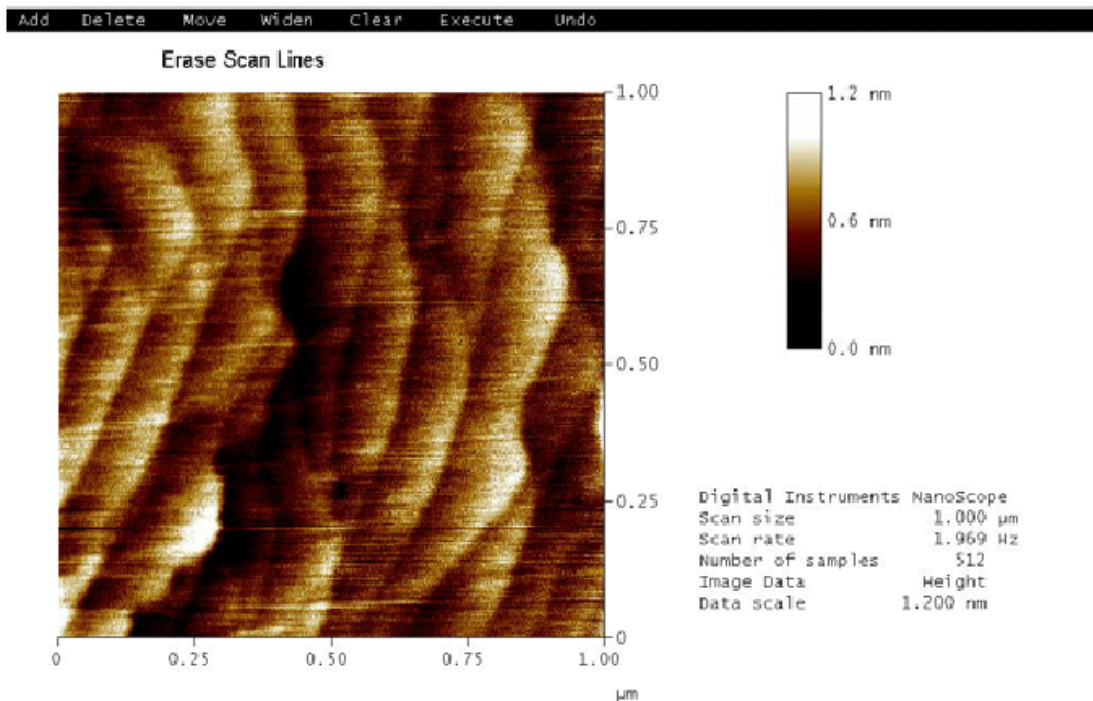


Fig. 6-8 The surface morphology of modulation-doped structure (sample No. 4), where Al composition is 0.3 and the total AlGa<sub>N</sub> layer thickness is 28 nm.

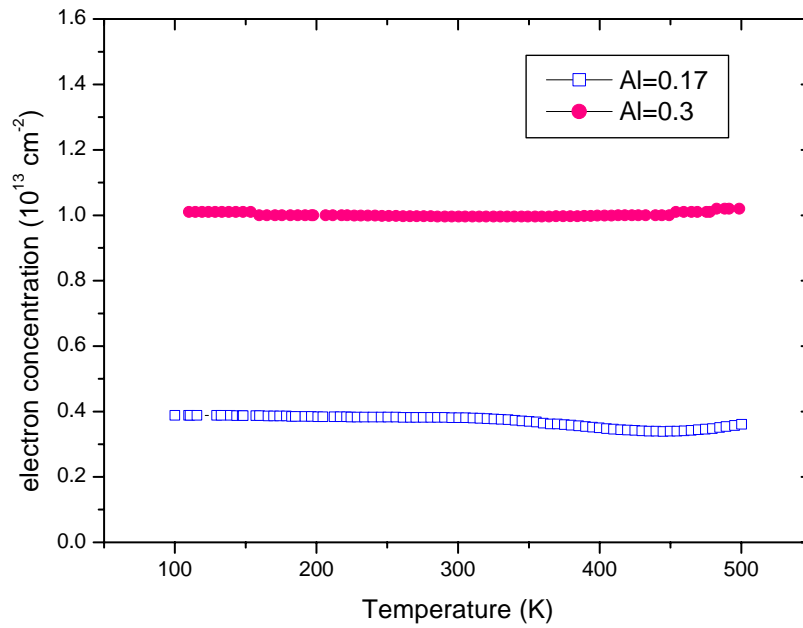


Fig. 6-9 A comparison on the electron concentration, where blank square ( $\square$ ) represents the sample with Al=0.17 (sample No. 1) and circle ( $\bullet$ ) represent the sample with Al=0.3 (sample No. 3).

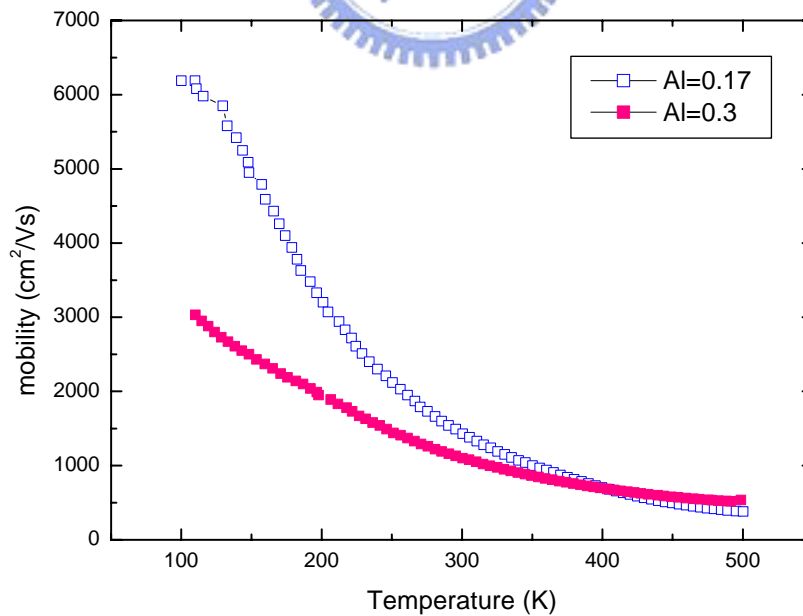


Fig. 6-10 A comparison on electron mobility, where blank square ( $\square$ ) represents the sample with Al=0.17 (sample No. 1) and circle ( $\bullet$ ) represents the sample with Al=0.3 (sample No. 3)

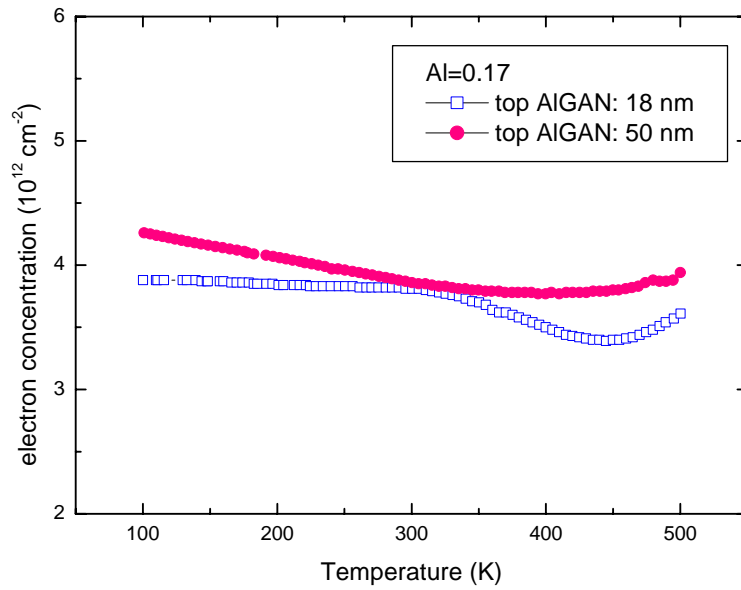


Fig. 6-11 A comparison on electron concentration, where blank square ( $\square$ ) represents the sample with AlGaN thickness of 18 nm (sample No. 1) and circle ( $\bullet$ ) represents the sample with AlGaN thickness of 50 nm (sample No. 2)

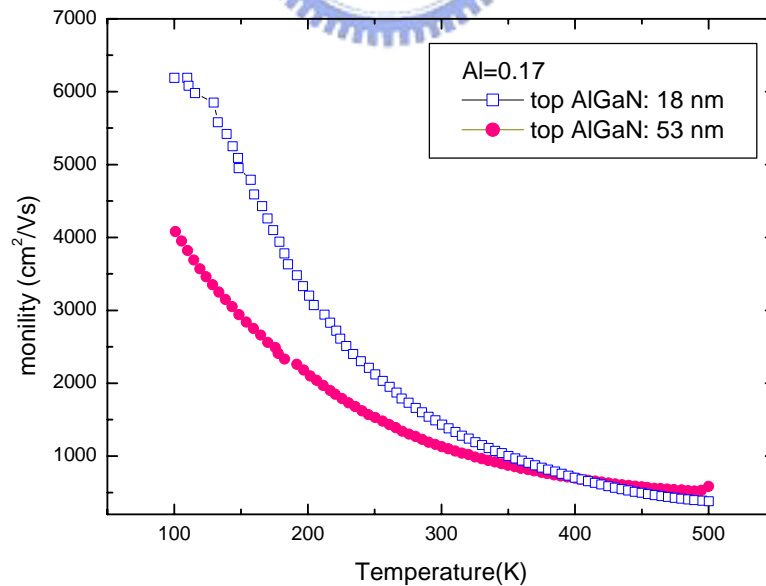


Fig. 6-12 A comparison on electron mobility, where blank square ( $\square$ ) represents the sample with AlGaN thickness of 18 nm (sample No. 1) and circle ( $\bullet$ ) represents the sample with AlGaN thickness of 50 nm (sample No. 2).

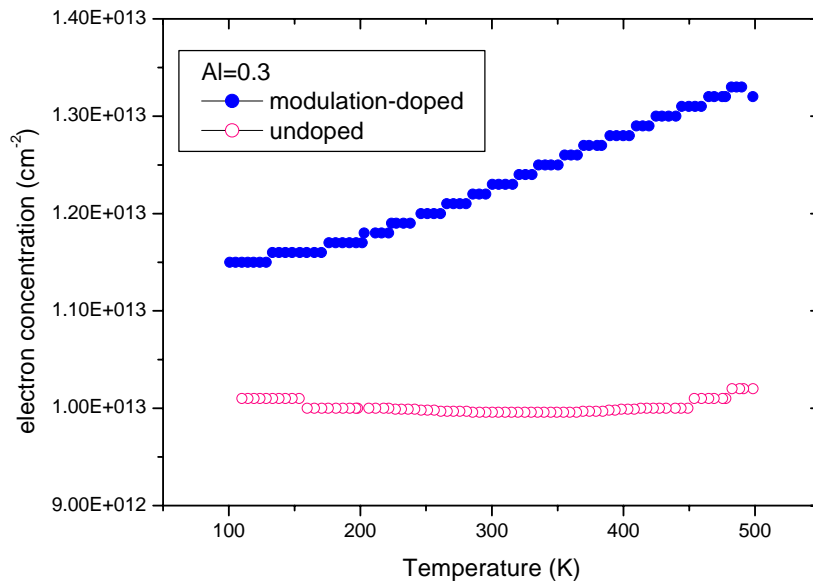


Fig. 6-13 A comparison on electron concentration, where blank circle ( $\square$ ) represents the undoped structure (sample No. 3) and circle ( $\bullet$ ) represents modulation-doped structure (sample No. 4).

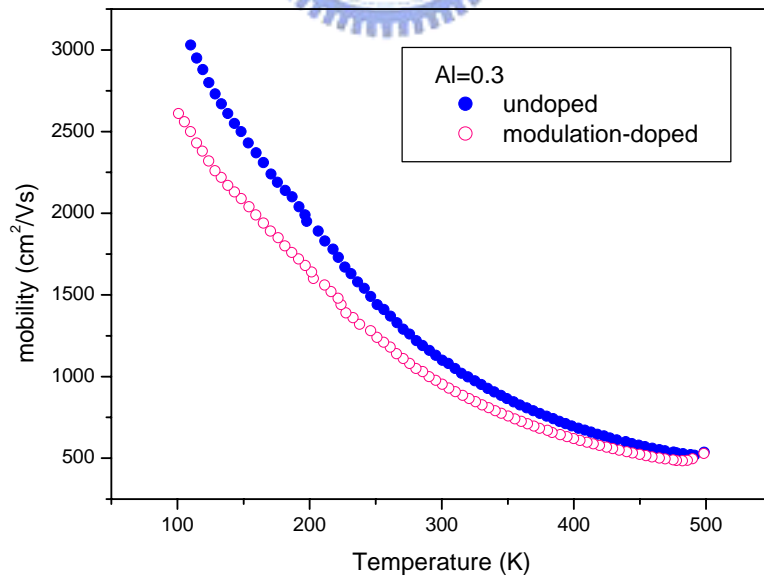
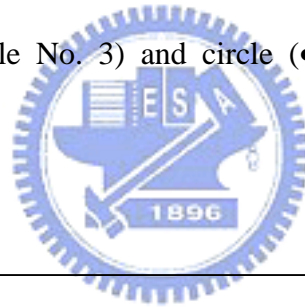


Fig. 6-14 A comparison on electron mobility, where blank circle ( $\square$ ) represents the undoped structure (sample No. 3) and circle ( $\bullet$ ) represents modulation-doped structure (sample No. 4)



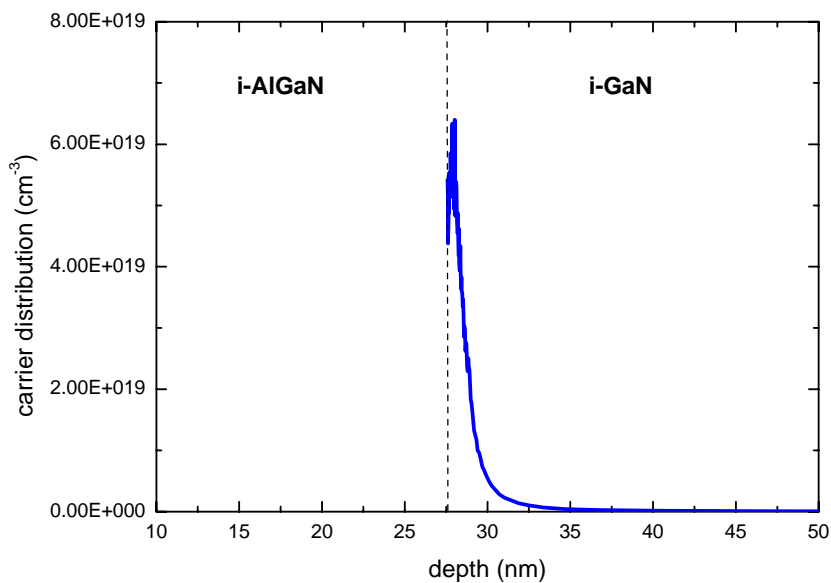


Fig. 6-15 The carrier profile of the undoped structure (sample No. 3) by C-V measurement. The dash line represents the location of AlGaN/GaN interface.

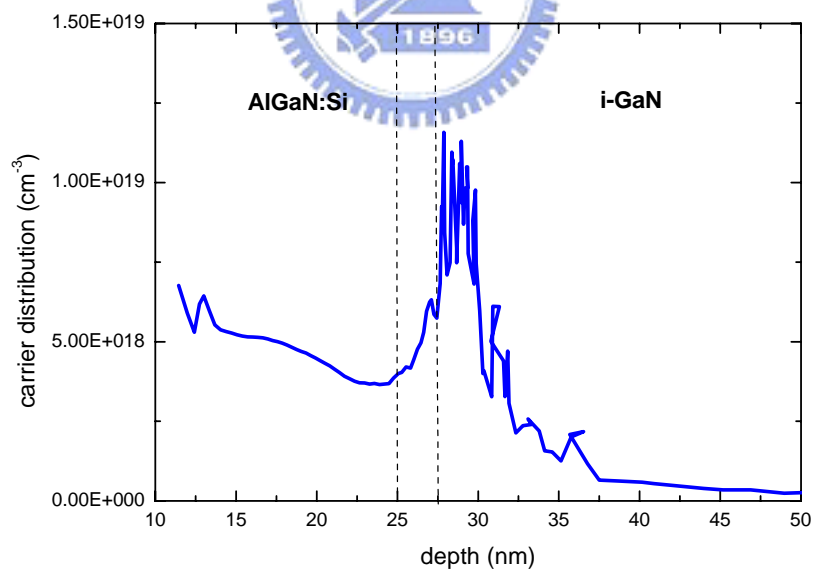


Fig. 6-16 The carrier profile of the modulation-doped structure (sample No. 4) by C-V measurement. The dash line represents the locations of AlGaN/GaN interface and undoped AlGaN spacer/Si-doped AlGaN interface, respectively.

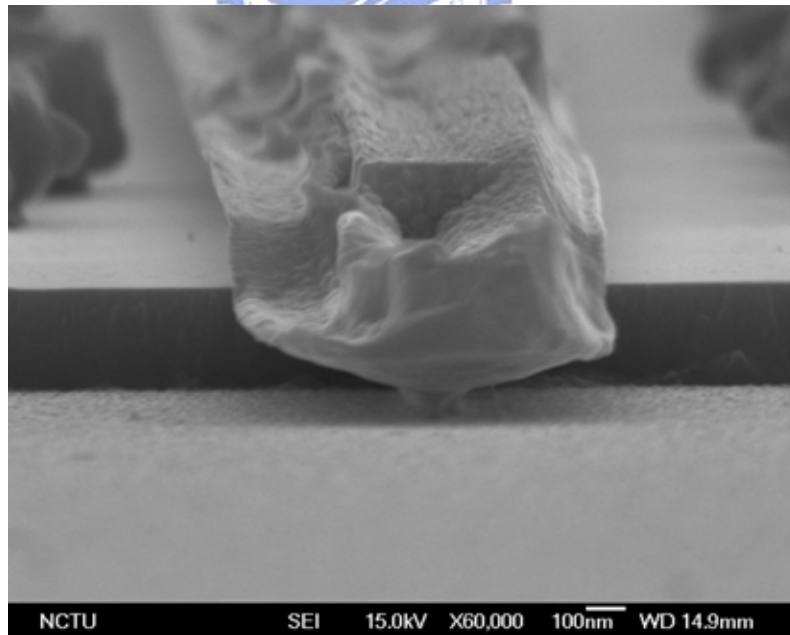
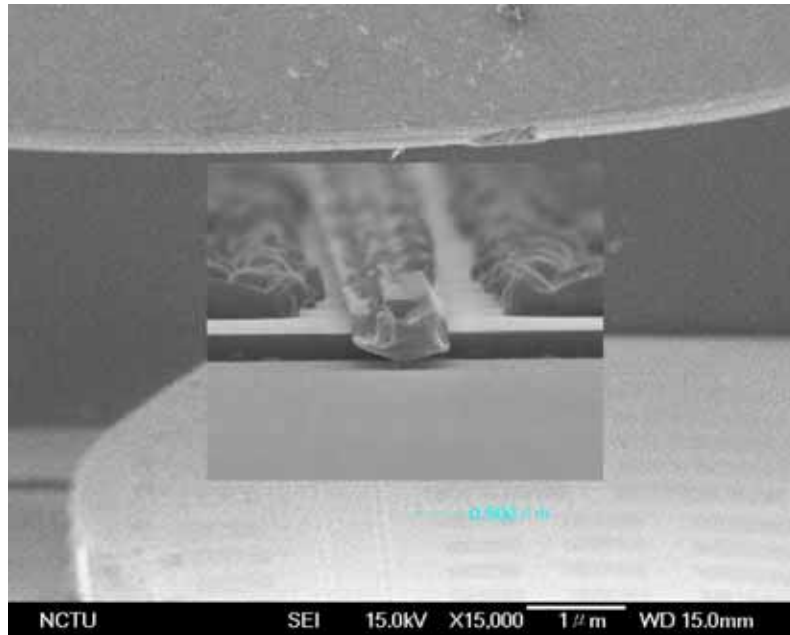


Fig. 6-17 The SEM images of an undoped  $\text{Al}_{0.3}\text{Ga}_{0.7}\text{N}/\text{GaN}$  HFET with a gate length of  $0.15 \mu\text{m}$  (top) and the enlarged picture of a  $0.15 \mu\text{m}$  long narrow T-gate.

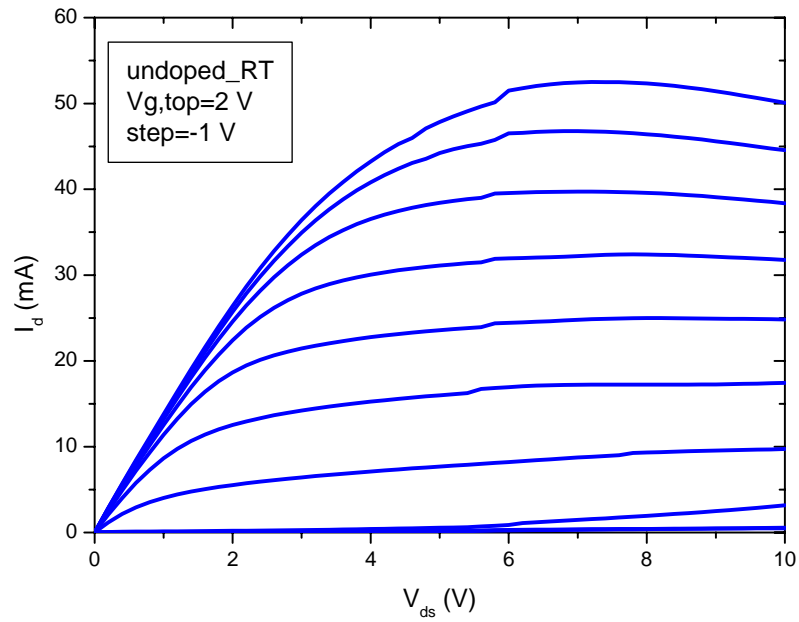


Fig. 6-18 Current-voltage characteristics of the undoped  $\text{Al}_{0.3}\text{Ga}_{0.7}\text{N}/\text{GaN}$  HFET. The gate length is  $0.15 \mu\text{m}$  and the device width is  $75 \mu\text{m}$ .

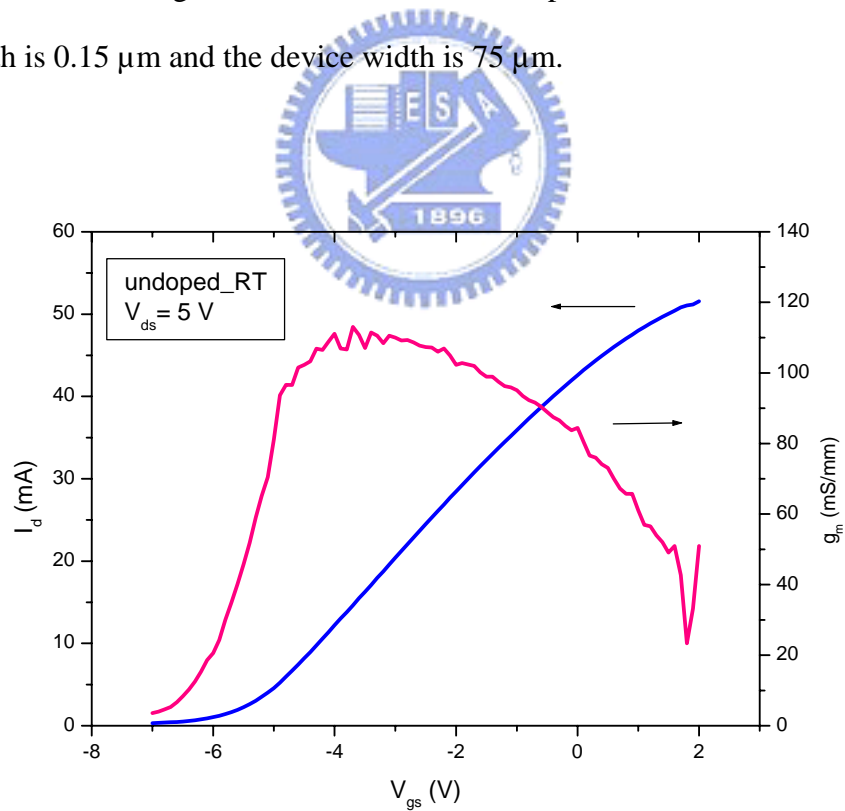


Fig. 6-19 DC transfer characteristics of the undoped  $\text{Al}_{0.3}\text{Ga}_{0.7}\text{N}/\text{GaN}$  HFET measured at  $V_{ds} = 5 \text{ V}$ . Its gate length is  $0.15 \mu\text{m}$  and device width is  $75 \mu\text{m}$ .

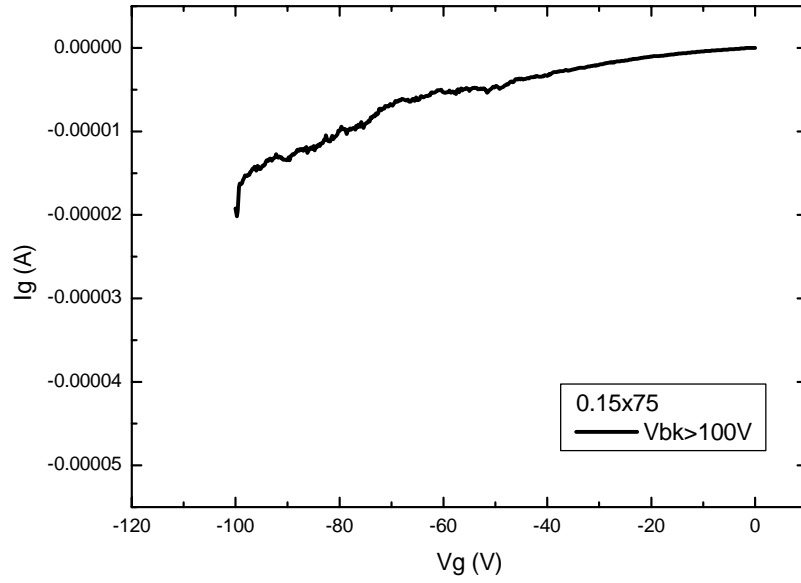


Fig. 6-20 Breakdown characteristics of the undoped  $\text{Al}_{0.3}\text{Ga}_{0.7}\text{N}/\text{GaN}$  HFET. Its gate length is  $0.15\ \mu\text{m}$  and device width is  $75\ \mu\text{m}$ .

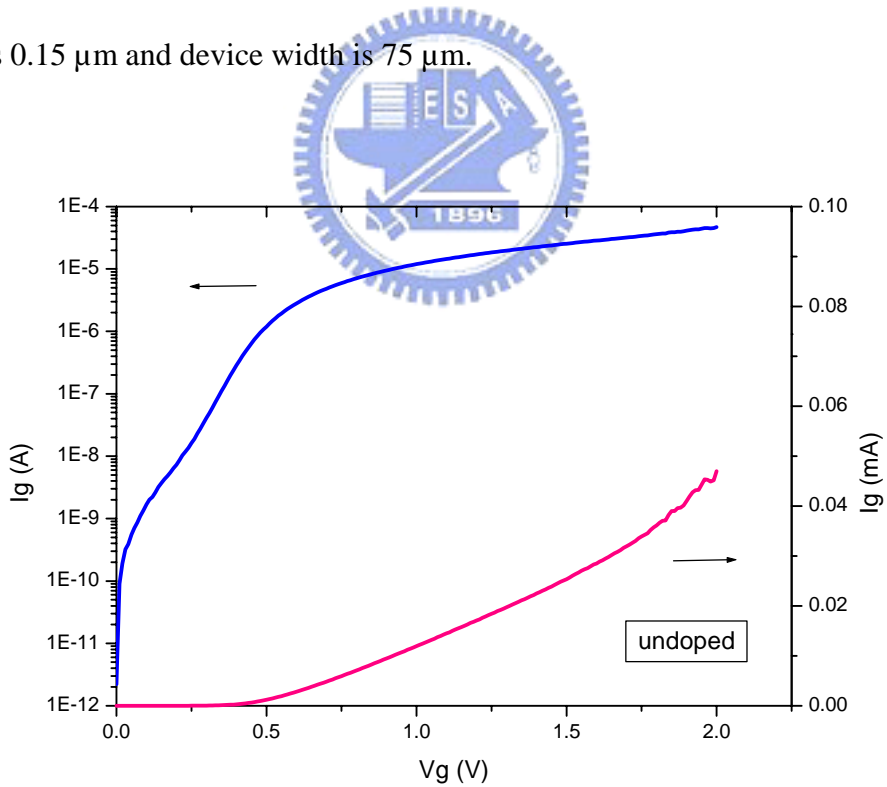


Fig. 6-21 Forward Schottky I-V characteristics of the undoped  $\text{Al}_{0.3}\text{Ga}_{0.7}\text{N}/\text{GaN}$  HFET.

Its gate length is  $0.15\ \mu\text{m}$  and device width is  $75\ \mu\text{m}$ .

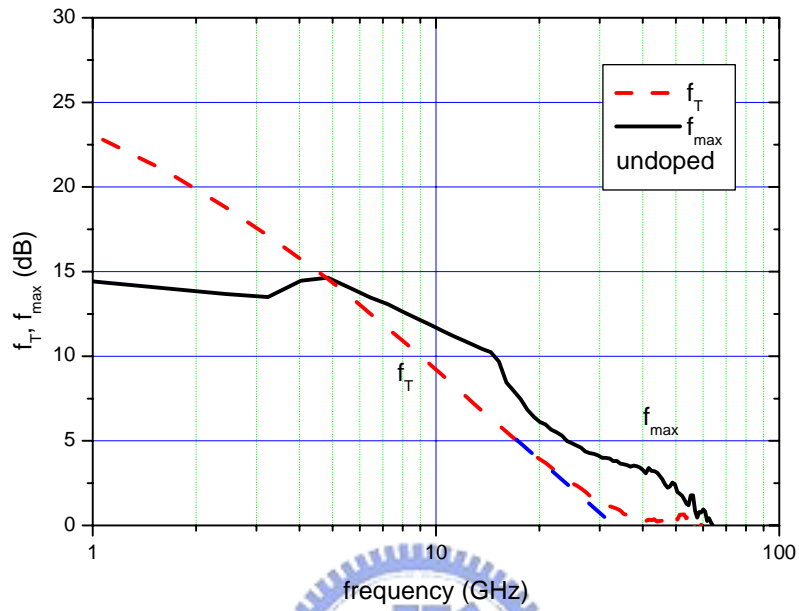


Fig. 6-22 Small-signal characteristics of the undoped  $\text{Al}_{0.3}\text{Ga}_{0.7}\text{N}/\text{GaN}$  HFET. Its gate length is  $0.15 \mu\text{m}$  and device width is  $75 \mu\text{m}$ .

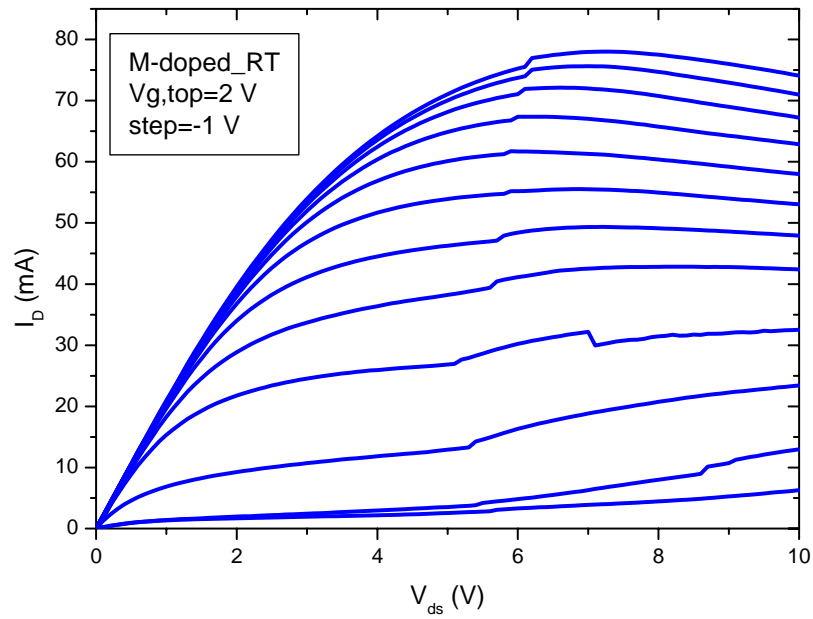


Fig. 6-23 Current-voltage characteristics of the modulation-doped  $\text{Al}_{0.3}\text{Ga}_{0.7}\text{N}/\text{GaN}$  HFET. The gate length is  $0.15 \mu\text{m}$  and the device width is  $75 \mu\text{m}$ .

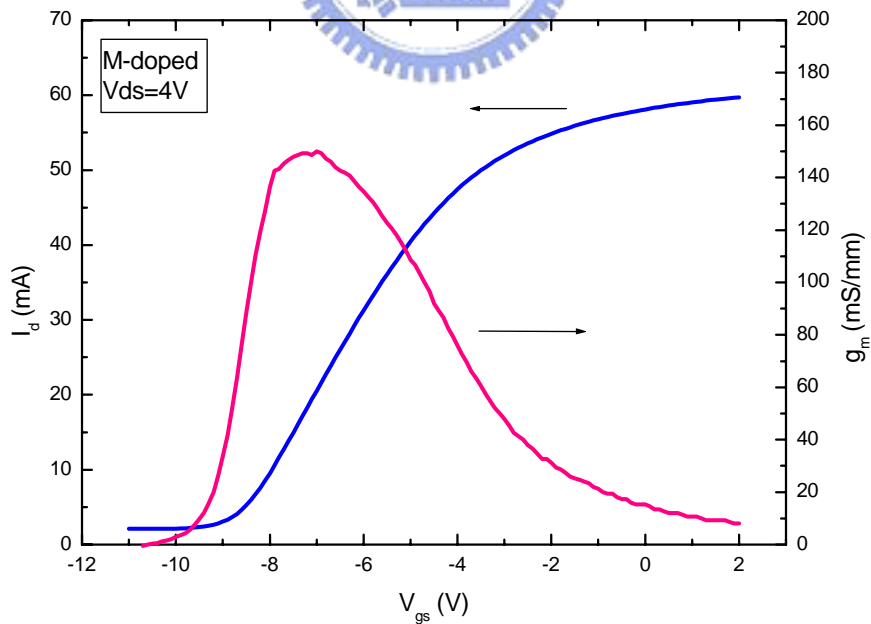


Fig. 6-24 DC transfer characteristics of the modulation-doped  $\text{Al}_{0.3}\text{Ga}_{0.7}\text{N}/\text{GaN}$  HFET. The gate length is  $0.15 \mu\text{m}$  and the device width is  $75 \mu\text{m}$ .

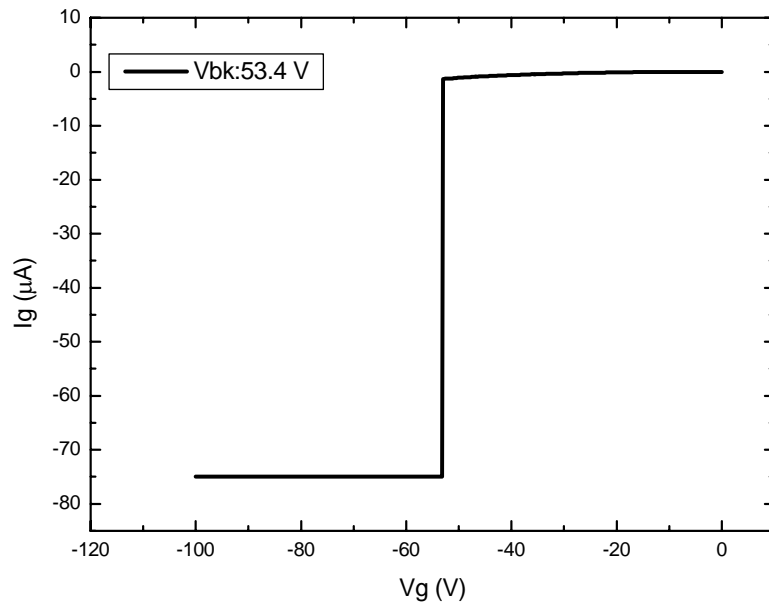


Fig. 6-25 Breakdown characteristics of the modulation-doped  $\text{Al}_{0.3}\text{Ga}_{0.7}\text{N}/\text{GaN}$  HFET. Its gate length is  $0.15 \mu\text{m}$  and device width is  $75 \mu\text{m}$ .

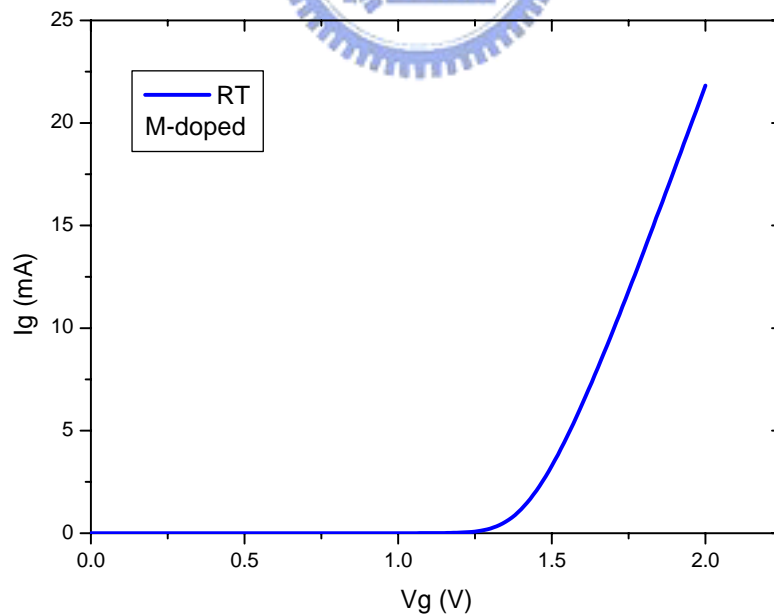


Fig. 6-26 The forward Schottky I-V characteristics of the modulation-doped  $\text{Al}_{0.3}\text{Ga}_{0.7}\text{N}/\text{GaN}$  HFET. Its gate length is  $0.15 \mu\text{m}$  and device width is  $75 \mu\text{m}$ .

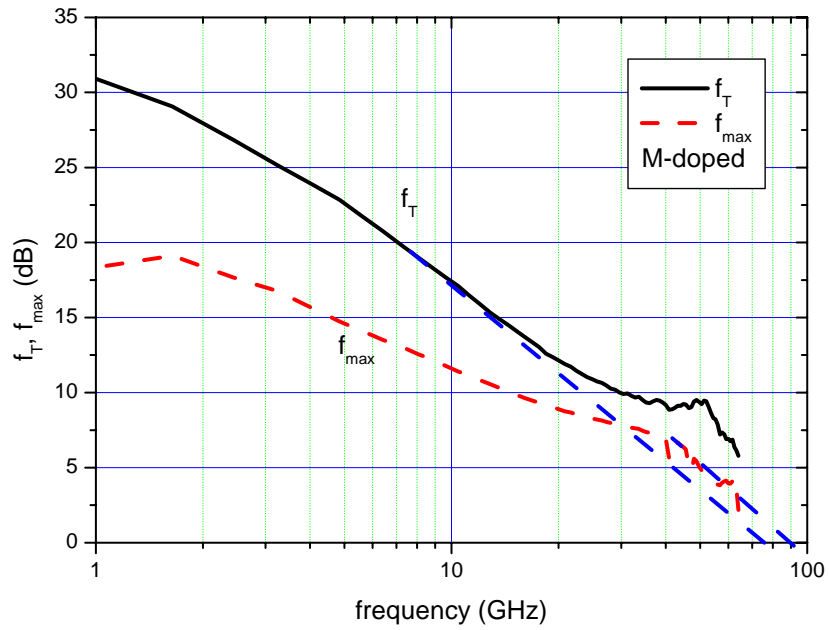


Fig. 6-27 Small-signal characteristics of the modulation-doped  $\text{Al}_{0.3}\text{Ga}_{0.7}\text{N}/\text{GaN}$  HFET. Its gate length is  $0.15 \mu\text{m}$  and device width is  $75 \mu\text{m}$ .

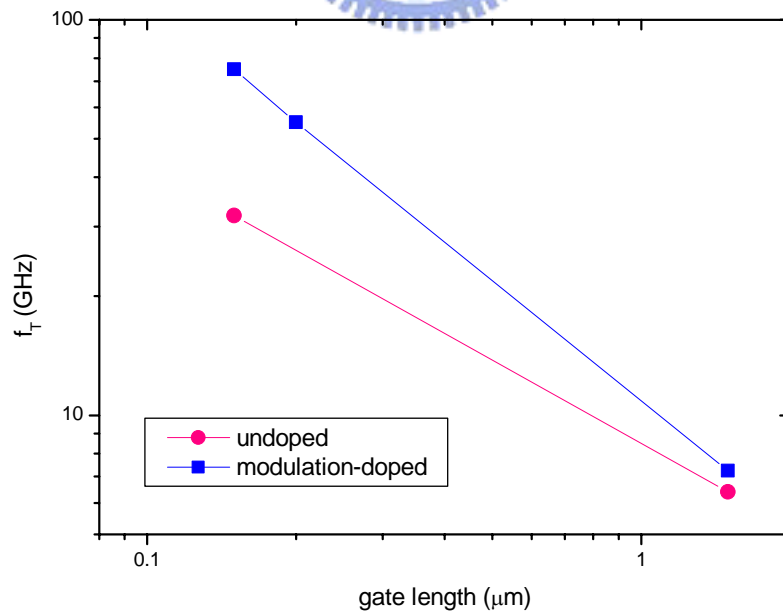


Fig. 6-28 The gate length dependence of the cut-off frequency for the undoped and modulation-doped  $\text{Al}_{0.3}\text{Ga}_{0.7}\text{N}/\text{GaN}$  HFETs.



## Chapter 7

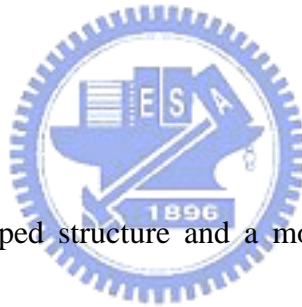
### Thermal effect of AlGaN/GaN heterostructure Field Effect Transistors

#### 7-1 Introduction

GaN-based heterostructure field-effect transistors (HFETs) are promising candidates for high-temperature and high-power applications at high frequencies due to their superior material properties, such as high breakdown field, high saturation velocity and excellent thermal stability [1-3]. For such operations, the stability of devices over temperature is extremely important. In addition to the commonly known problem in the thermal conductivity of substrates [4-5], the device structure plays a crucial role in realizing GaN-based HFETs for high-temperature applications. So far, several device structures, such as the undoped structure [6], the modulation-doped structure [7] and the channel-doped structure [8-9], have been used to realize high-performance GaN-based HFETs. Obviously devices with different structures may exhibit different electrical behaviors at high temperatures due to their different electron transport properties. In this article, we report a comparison on the temperature dependence of the electron transport properties and device characteristics of the undoped and modulation-doped AlGaN/GaN HFETs. The results obtained

indicate that the device structure has a significant influence on the electron transport properties of devices and the device performance at high temperatures. By the analysis of the activation energy, we identify that the increase in electron concentration in the modulation-doped structure at high temperatures is dominated by the thermal activation of Si donors. The modulation-doped devices, with a higher electron concentration, comparable mobility and lower parasitic source resistance at high temperatures, exhibited better dc and RF performance than the undoped devices over temperatures.

## 7-2 Experiments



Two structures, an undoped structure and a modulation-doped structure, were grown by metalorganic chemical vapor deposition (MOCVD) on c-plane sapphire substrates. The undoped structure consists of a 3  $\mu\text{m}$  undoped GaN buffer layer and a 28 nm undoped AlGa<sub>0.3</sub>N cap layer. The modulation-doped structure consists of a 3  $\mu\text{m}$  undoped GaN buffer layer, a 3 nm undoped AlGa<sub>0.3</sub>N spacer, a 20 nm Si-doped AlGa<sub>0.3</sub>N layer with a doping concentration of  $5 \times 10^{18} \text{ cm}^{-3}$  and a 5 nm undoped AlGa<sub>0.3</sub>N cap layer. The Al composition is 0.3 for all samples. Contact metal, Ti/Al/Ti/Au (200/1500/450/550 Å), was deposited and annealed at 750°C for 30 s in N<sub>2</sub> gas ambient to form ohmic contact pads. Hall effect measurements with Van der Pauw

geometry were performed to characterize the electrical properties of two-dimensional electron gases (2DEG) in the temperature range from 100K to 500K. Capacitance-voltage (C-V) profiling revealed that most carriers were located at the AlGa<sub>N</sub>/Ga<sub>N</sub> interface.

Device fabrication process began with mesa isolation, followed by Ohmic contact and narrow T-gate fabrication. Mesa patterns for device active regions were defined by photolithography and dry etch with Cl<sub>2</sub>/Ar plasma using an inductive coupled plasma (ICP) system. Prior to contact metal deposition, the samples were treated by Ar plasma. Contact metal, Ti/Al/Ti/Au (200/1500/450/550 Å), was then deposited and lifted-off to form the contact pads. The samples were annealed at 750°C for 30 s in N<sub>2</sub> gas ambient. The contact resistances of 0.59 ohm-mm for the undoped devices and of 0.38 ohm-mm for modulation-doped devices by the transmission line measurement (TLM) were obtained. The source-drain spacing is 2 μm for all samples. In the narrow T-gate fabrication, the resist stack consisted of a low-sensitivity 495k PMMA layer of 120 nm thickness in the bottom and a high-sensitivity copolymer EL 12.5 PMMA-MAA (680 nm) on the top. The e-beam acceleration voltage used here was 15 kV. Metal deposition of Ni (20 nm)/Au (300 nm) was performed using e-beam evaporation. Finally, the sample was soaked in acetone for metal lift-off.

Device dc and small-signal s-parameter measurements were performed using

HP4142 dc analyzer and Anritsu37397 vector network analyzer (VNA) at temperatures ranging from room temperature to 200°C to observe the device high temperature performance. Before measurement, the actual temperature of the surface of the hot chuck was checked carefully by a thermocouple. During high temperature measurement, a 15 minutes delay for probe stability was performed for a reliable high temperature s-parameter measurement.

### 7-3 Results and discussion

#### 7-3-1 Electron transport properties

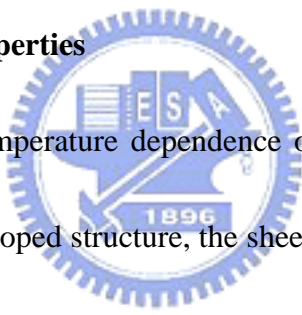


Figure 7-1 shows the temperature dependence of the electron concentration of the two structures. For the undoped structure, the sheet charge concentration of 2DEG is around  $1 \times 10^{13} \text{ cm}^{-2}$  and is nearly constant over the measured temperature range. This 2DEG is due to the strong spontaneous and piezoelectric polarization effect [10]. For the modulation-doped structure, the electron concentration is temperature dependent. The sheet charge concentration increases from  $1.15 \times 10^{13} \text{ cm}^{-2}$  at 100K to  $1.33 \times 10^{13} \text{ cm}^{-2}$  at 500K.

At very low temperatures, because of the freeze-out of Si donors in the AlGaIn layer, the channel conduction of the modulation-doped structure markedly decreases. As the temperature increases, the thermal activation process starts to release gradually

the frozen electrons and thus the measured sheet carrier density increases.

The activation energy of Si donors in the AlGaN layer was calculated using the temperature-dependent Hall data. The semi-log plot of the carrier density versus  $1/T$  is shown in Fig. 7-2. The fitted line based on the charge neutrality condition [11],

$$\frac{n(N_A + n)}{N_D - N_A - n} = \frac{N_c}{g_d} \exp\left(-\frac{E_d}{kT}\right), \quad (1)$$

is used to calculate the activation energy. In this equation,  $n$  is the increased electron concentration due to the thermal activation process;  $N_D$  and  $N_A$  are the donor and acceptor concentrations, respectively;  $N_c$  is the effective density of state in the conduction band;  $g_d$  is the donor spin-degeneracy factor; and  $E_d$  is the activation energy of Si donors in  $\text{Al}_{0.3}\text{Ga}_{0.7}\text{N}$ . In this calculation,  $n$  is obtained using

$$n = \frac{N_s(T) - N_s(100K)}{d_{\text{AlGaN}}}, \quad (2)$$

where  $N_s(T)$  is the sheet charge concentration measured at different temperatures, the numerator,  $N_s(T) - N_s(100K)$ , represents the increased sheet charge concentration due to the thermal activation process and  $d_{\text{AlGaN}}$  is the effective Si-doped AlGaN layer thickness, a fitting parameter. Based on the fitted result,  $d_{\text{AlGaN}}$  is estimated to be around 13 nm. This value is reasonable since part of the AlGaN layer is depleted due to the surface potential.  $N_D$  is  $5 \times 10^{18} \text{ cm}^{-3}$ ;  $N_A$  is assumed to be much smaller than  $N_D$  for the uncompensated condition;  $N_c$  is also temperature dependent and is proportional to  $T^{3/2}$ ; the donor spin-degeneracy factor,  $g_d$ , is 2; and  $E_d$  is the fitting

parameter. Also, a single-donor model was used for this calculation. As can be seen in Fig. 7-2, a good fitting can be obtained with the activation energy of 83.2 meV. This result is slightly lower than the previously reported Si donor level in  $\text{Al}_{0.3}\text{Ga}_{0.7}\text{N}$  [12-13]. Thus, it is apparent that the thermal activation process in the Si-doped AlGaN layer plays an important role in the temperature dependence of the device performance for the modulation-doped structure.

Figure 7-3 shows the temperature dependence of the electron mobility of the two structures. As a whole, the electron mobilities of the two structures decrease with temperature as a result of the increased phonon scattering. The undoped structure has a low-temperature electron mobility of  $3030 \text{ cm}^2/\text{Vs}$  at 100K and room-temperature electron mobility of  $1100 \text{ cm}^2/\text{Vs}$ . The modulation-doped structure has an electron mobility of  $2610 \text{ cm}^2/\text{Vs}$  at 100K and a room-temperature mobility of  $953 \text{ cm}^2/\text{Vs}$ . The lower mobility for the modulation-doped structure is due to the additional ionized impurity scattering associated with Si donors and possible parallel conduction in the doped AlGaN layer. As the temperature increased above 450K, the two structures showed comparable electron mobilities. At 500K, the mobilities are  $537 \text{ cm}^2/\text{Vs}$  and  $529 \text{ cm}^2/\text{Vs}$  for the undoped and modulation-doped structures, respectively. This is due to the enhanced phonon scattering that dominates over impurity scattering at high temperatures. Similar results were also obtained in a previous study [14].

### 7-3-2 Device high temperature performances

In this study, the actual temperature of the surface of the hot chuck is defined as the test temperature. Figure 7-4 shows the current-voltage characteristics of the undoped AlGaIn/GaN HFETs at room temperature and 200°C. The gate length and width are 0.15  $\mu\text{m}$  and 75  $\mu\text{m}$ , respectively. At room temperature, the undoped device showed good dc performance. The maximum drain current is 700 mA/mm at drain bias  $V_{\text{ds}}=7\text{ V}$  and gate bias  $V_{\text{gs}}=2\text{ V}$ . The reduction in the drain current at higher drain bias was due to the self-heating effect as a result of the poor thermal conductivity of the sapphire substrate. Good channel pinch-off and self-heating were also clearly observed at 200°C. The maximum drain current at 200°C was reduced to 567 mA/mm at  $V_{\text{ds}}=5.5\text{ V}$  and  $V_{\text{gs}}=2\text{ V}$ . The drain current reduction at high temperature is due to the 2DEG mobility degradation.

Figure 7-5 shows the dc transfer characteristics of the undoped AlGaIn/GaN HFETs at drain bias  $V_{\text{ds}}=5\text{ V}$  measured at different temperatures. In particular, the extrinsic transconductance showed small variation over a wide gate bias range, which indicated a good linearity of the undoped device. The maximum extrinsic transconductance at room temperature and 200°C is 113 mS/mm at  $V_{\text{gs}}=-3.8\text{ V}$  and 86 mS/mm at  $V_{\text{gs}}=-3\text{ V}$ , respectively. The lower extrinsic transconductance obtained

here is due to the high source resistance of the undoped device. The source resistance and the intrinsic transconductance at room temperature are 3.4 ohm-mm and 183 mS/mm, respectively. The threshold voltage is close to -7 V and is constant over the measured temperature range. This indicated the good thermal stability of the Schottky metal between the underlying undoped AlGaN in the undoped devices. Figure 7-6 shows the forward Schottky gate I-V characteristics of undoped  $\text{Al}_{0.3}\text{Ga}_{0.7}\text{N}/\text{GaN}$  HFETs at room temperature and 200°C. At 200°C, this device showed a slightly higher gate current than that at room temperature. The calculated ideality factor is around 2, which is slightly large. Thus the Schottky barrier height could not be extracted correctly. The gate resistance, which is extracted from the linear Schottky I-V, is very large, ~40000 ohm.

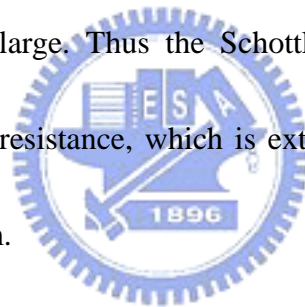


Figure 7-7 shows the current-voltage characteristics of the modulation-doped AlGaN/GaN HFETs at room temperature and 200°C. Device dimension is also  $0.15 \times 75 \mu\text{m}^2$ . At room temperature, a very high maximum drain current of 1040 mA/mm is obtained at drain bias  $V_{\text{ds}} = 7 \text{ V}$  and gate bias  $V_{\text{gs}} = 2 \text{ V}$ . The self-heating effect was also clearly observed at larger drain bias. The maximum drain current at 200°C is reduced to 678 mA/mm at  $V_{\text{ds}} = 7 \text{ V}$  and  $V_{\text{gs}} = 2 \text{ V}$ .

Figure 7-8 shows the dc transfer characteristics of the modulation-doped AlGaN/GaN HFET at drain bias  $V_{\text{ds}} = 5 \text{ V}$  under different temperatures. The measured



extrinsic transconductance at different temperatures showed larger changes over the gate bias than the undoped devices. The maximum extrinsic transconductance at room temperature and 200°C is 198 mS/mm at  $V_{gs} = -6.3$  V and 125 mS/mm at  $V_{gs} = -6.7$  V, respectively. The source resistance and the intrinsic transconductance at room temperature are 2.67 ohm-mm and 420 mS/mm, respectively. The threshold voltage is close to -9 V and no obvious threshold voltage shift was observed over the whole temperature range. This indicated the good thermal stability of the Schottky metal between the underlying undoped AlGa<sub>N</sub> in the modulation-doped devices. Figure 7-9 shows the forward Schottky gate I-V characteristics of modulation-doped Al<sub>0.3</sub>Ga<sub>0.7</sub>N/GaN HFETs at room temperature and 200°C. At 200°C, this device also showed a slightly higher gate current than that at room temperature. The excellent thermal stability of the metal/nitride Schottky contacts over wide temperature was also observed in previous reports [15]. The gate resistance of modulation-doped device is around 25 ohm at room temperature, which is much smaller than the undoped device.

Figure 7-10 shows the comparison of the temperature dependence of the maximum drain current at a gate bias  $V_{gs} = 2$  V. The undoped device showed the maximum drain current of 700 mA/mm at room temperature. At 200°C it reduced to 567 mA/mm. The modulation-doped device exhibited a larger maximum drain current.

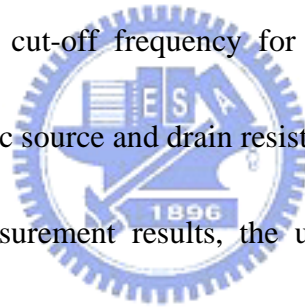
At room temperature, it was of 1040 mA/mm and at 200°C it became 678 mA/mm.

The larger change in the maximum drain current for the modulation-doped device can be attributed to the temperature dependent sheet carrier density. The undoped device showed a drain current changing rate of  $-5.8$  mA/mm per  $10^\circ\text{C}$ . The modulation-doped device, however, showed a drain current changing rate of  $-20.9$  mA/mm per  $10^\circ\text{C}$ .

Figure 7-11 shows the comparison of the maximum extrinsic transconductances measured at a drain bias  $V_{ds}=5$  V for both devices over temperature. In general, the modulation-doped devices had a higher transconductance than the undoped devices. But the undoped device had a smaller change in transconductance over temperature. For the modulation doped structure, the transconductance changed from 198 mS/mm at room temperature to 125 mS/mm at  $200^\circ\text{C}$ . For the undoped device, the transconductances ranged from 113 mS/mm to 86 mS/mm over the temperatures. The lower transconductance is due to the large source resistance, which was 3.4 ohm-mm, of the undoped channel in the undoped device. For the modulation-doped device it was 2.67 ohm-mm. The change rate of the transconductance for the modulation-doped device was  $-4.4$  mS/mm per  $10^\circ\text{C}$ .

Figure 7-12 shows the comparison of the temperature dependence of the current gain cut-off frequency ( $f_T$ ) for both devices. The undoped device was operated at  $V_{ds}=\text{---}$

6 V and  $V_{gs} = -3.5$  V. The modulation-doped device was operated at  $V_{ds} = 6$  V and  $V_{gs} = -6$  V. For the undoped device, the cut-off frequency was 32 GHz at room temperature, but degraded to 22 GHz at 200°C. The modulation-doped device had a room temperature  $f_T$  of 75 GHz and did not show obvious degradation until 100°C. Above 100°C, the cut-off frequency became lower and dropped to 52 GHz at 200°C. As a whole, both devices did not show obvious degradation for temperatures below 100°C. A similar result was also observed in the doped channel AlGaIn/GaN HFETs [8]. The main reason is the weak temperature dependence of electron transport property [16-17]. The lower cut-off frequency for the undoped device is mainly attributed to the larger parasitic source and drain resistances.



Based on the Hall measurement results, the undoped device had a constant two-dimensional electron gas (2DEG) concentration in the channel over a wide temperature range. The modulation-doped device had a higher electron concentration but it increased with temperature, due to the thermal activation of Si donors in the AlGaIn layer. Although lower electron mobility was observed in the modulation doped devices due to the additional ionized impurity scattering associated with the Si donors, the electron mobilities for both devices are similar at high temperatures where phonon scattering is the dominant scattering process. Because of the additional doping, the modulation-doped devices has lower parasitic source and drain resistances than the

undoped devices over temperatures. Putting all these factors together, we may conclude that the modulation-doped devices are superior to the undoped devices over the temperatures studied. The stability (the temperature dependence of device performance), however, is not as good as the undoped devices.

#### **7-4 Conclusion**

We investigated the thermal effect of the AlGa<sub>N</sub>/Ga<sub>N</sub> HFETs. We compared the temperature dependence of the electron transport properties and device characteristics of the undoped and modulation-doped AlGa<sub>N</sub>/Ga<sub>N</sub> HFETs. The results obtained indicate that the device structure has a significant influence on the electron transport properties of devices and device performance over temperature. The undoped structure has a constant 2DEG concentration over a wide temperature range, while the modulation-doped structure has a temperature-dependent electron concentration. The increase in electron concentration in the modulation-doped structure at high temperatures was caused by the thermal activation of Si donors in the AlGa<sub>N</sub> layer. Although the undoped structure has a higher mobility at low and moderate temperatures, both the modulation structure and the undoped structure have comparable mobilities at high temperatures. The modulation-doped devices are superior to the undoped devices over the temperatures studied due to the higher

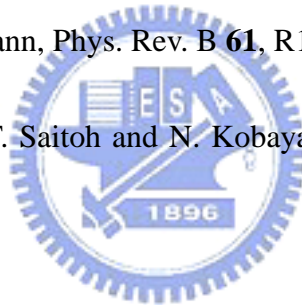
electron concentration together with comparable electron mobility obtained at high temperatures. The stability (the temperature dependence of device performance), however, is not as good as the undoped devices.



## References

- [1] S. Keller, Y. F. Wu, G. Parish, N. Ziang, J. J. Xu, B. P. Keller, S. P. DenBaars and U. K. Mishra, *IEEE Trans. Electron Devices* **48**, 552 (2001).
- [2] L. F. Eastman and U. K. Mishra, *IEEE spectrum*, May, 28 (2002).
- [3] U. K. Mishra, P. Parikh and Y. F. Wu, *Proc. of the IEEE* **90**, 1022 (2002).
- [4] Y. F. Wu, B. P. Keller, S. Keller, D. Kapolnek, P. Kozodoy, S. P. DenBaars and U. K. Mishra, *Solid-State Electron.* **41**, 1569 (1997).
- [5] R. Gaska, J. Yang, A. Osinsky, M. F. Khan and M. S. Shur, *IEDM Tech. Dig.*, 565 (1997).
- [6] L. F. Eastman, V. Tilak, J. Smart, B. M. Green, E. M. Chumbes, R. Dimitrova, H. Kim, O. Ambacher, N. Weimann, T. Prunty, M. Murphy, W. J. Schaff and J. R. Shealy, *IEEE Trans. Electron Devices* **48**, 479 (2001).
- [7] M. Akita, S. Kishimoto and T. Mizutani: *IEEE Electron Device Lett.* **22**, 376 (2001).
- [8] Q. Chen, R. Gaska, M. F. Khan and M. S. Shur, A. Ping, I. Adesida, J. Burm, W. J. Schaff and L. F. Eastman, *Electron Lett.* **33**, 637 (1997).
- [9] I. Daumiller, C. Kirchner, M. Kamp, K. J. Ebeling and E. Kohn, *IEEE Electron Device Lett.* **20**, 448 (1999).
- [10] O. Ambacher, J. Smart, J. R. Shealy, N. G. Weimann, K. Chu, M. Murphy, W. J.

- Schaff, L. F. Eastman, R. Dimitrova, L. Wittmer, M. Stutzmann, W. Rieger and J. Hilsenback, *J. Appl. Phys.* **85**, 3222 (1999).
- [11] N. Chand, T. Henderson, J. Klem, W. T. Masselink, R. Fischer, Y. C. Chang and H. Morkoc, *Phys. Rev. B* **30**, 4481 (1984).
- [12] M. Stutzmann, O. Ambacher, A. Cros, M. S. Brandt, H. Angerer, R. Dimitrova, N. Reinacher, T. Metzger, R. Höpler, D. Brunner, F. Freudenberg, R. Handschuh and C. Deger, *Mater. Sci. Eng.* **B50**, 212 (1997).
- [13] R. Zeisel, M. W. Bayerl, S. T. B. Goennenwein, R. Dimitrova, O. Ambacher, M. S. Brandt and M. Stutzmann, *Phys. Rev. B* **61**, R16283 (2000).
- [14] N. Maeda, K. Tsubaki, T. Saitoh and N. Kobayashi, *Appl. Phys. Lett.* **79**, 1634 (2001).
- [15] M. Akita, S. Kishimoto and T. Mizutani, *IEEE Electron Device Lett.*, **22**, 376 (2001).
- [16] N. S. Mansour, K. W. Kim and M. A. Littlejohn, *J. Appl. Phys.*, **77**, 2834 (1995).
- [17] U. V. Bhapkar and M. S. Shur, *J. Appl. Phys.*, **82**, 1649 (1997).



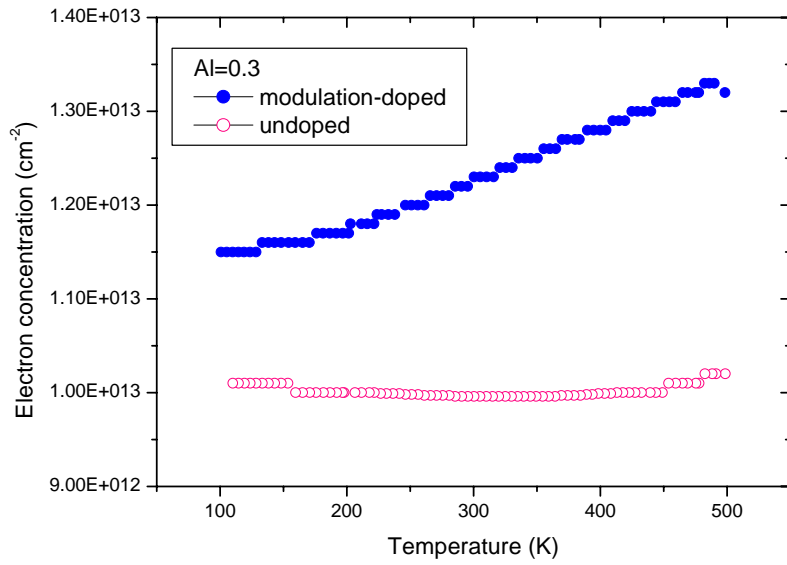


Fig. 7-1 Temperature dependence of the electron concentration of the undoped and modulation-doped structures.

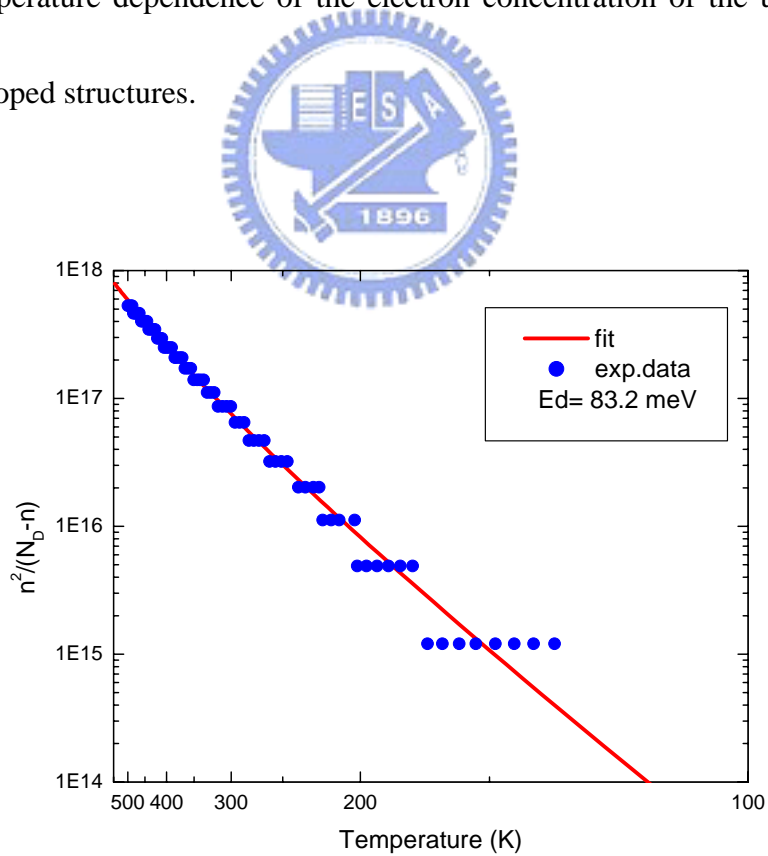


Fig. 7-2 Temperature dependence of the increased electron concentration due to the thermal activation process and the activation energy,  $E_d$ , of Si donors in  $Al_{0.3}Ga_{0.7}N$ .



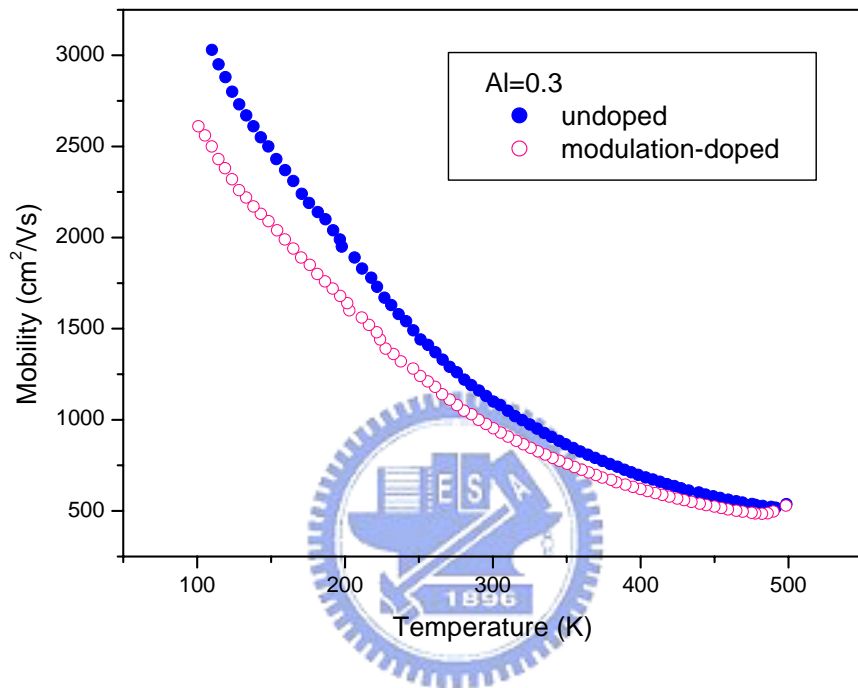


Fig. 7-3 Temperature dependence of the electron mobility of the undoped and modulation-doped structures.

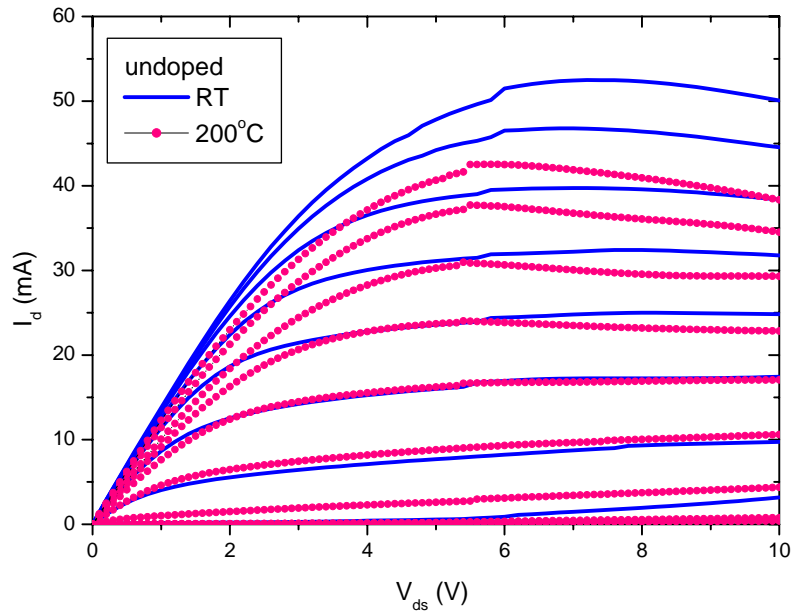


Fig. 7-4 Current-voltage characteristics of the undoped  $\text{Al}_{0.3}\text{Ga}_{0.7}\text{N}/\text{GaN}$  HFETs at room temperature and  $200^\circ\text{C}$ . ( $V_{\text{gs, top}} = 2 \text{ V}$  and step  $= -1 \text{ V}$ ).

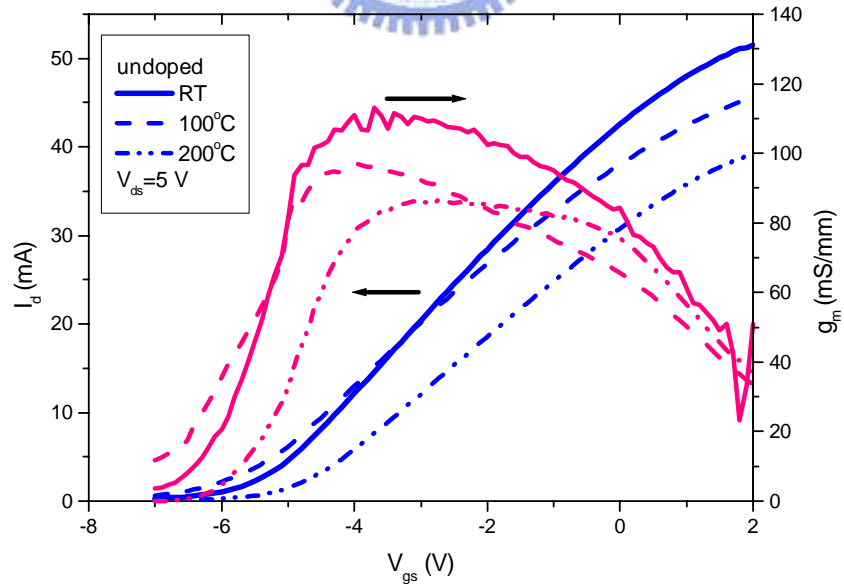


Fig. 7-5 DC transfer characteristics of the undoped  $\text{Al}_{0.3}\text{Ga}_{0.7}\text{N}/\text{GaN}$  HFETs at drain bias  $V_{\text{ds}} = 5 \text{ V}$  under different temperatures.

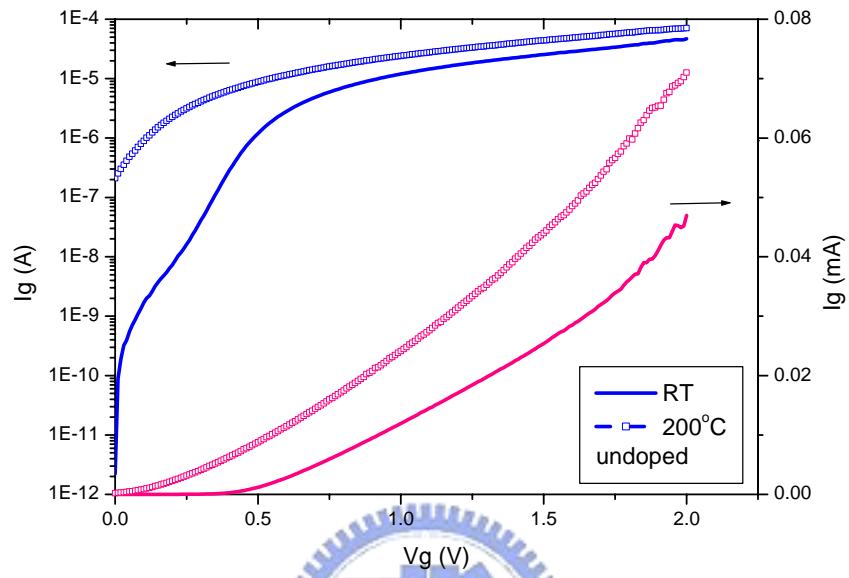


Fig. 7-6 Forward Schottky gate I-V characteristics of undoped  $\text{Al}_{0.3}\text{Ga}_{0.7}\text{N}/\text{GaN}$  HFETs at room temperature and  $200^\circ\text{C}$ .

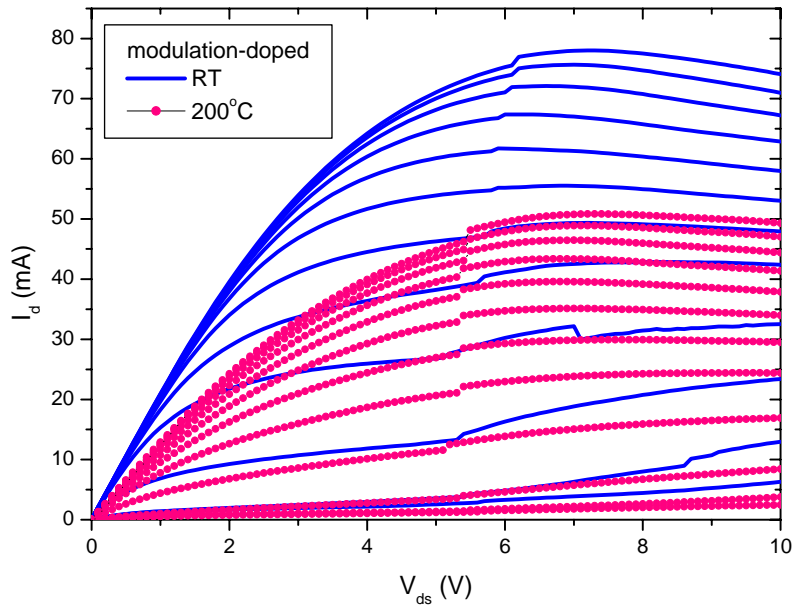


Fig. 7-7 Current-voltage characteristics of the modulation-doped  $\text{Al}_{0.3}\text{Ga}_{0.7}\text{N}/\text{GaN}$

HFETs at room temperature and  $200^\circ\text{C}$ . ( $V_{\text{gs, top}} = 2\text{ V}$  and step =  $-1\text{ V}$ ).

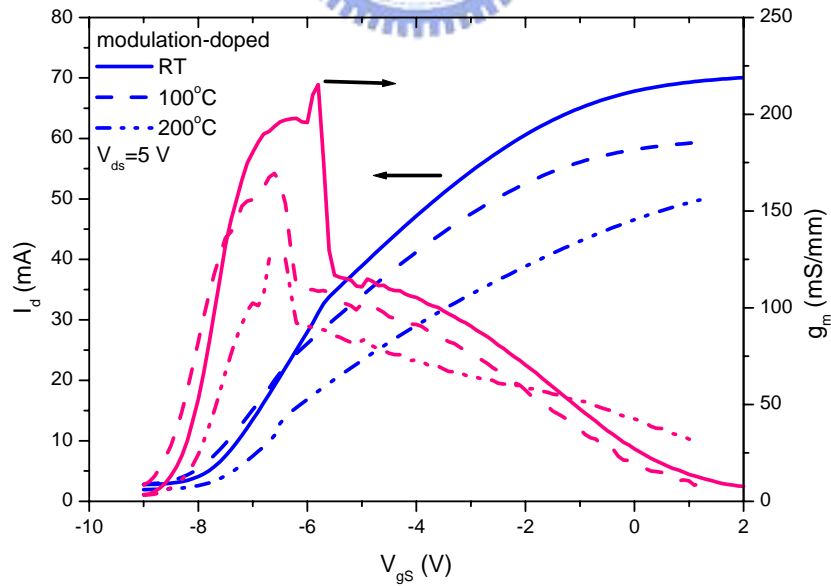


Fig. 7-8 DC transfer characteristics of the modulation-doped  $\text{Al}_{0.3}\text{Ga}_{0.7}\text{N}/\text{GaN}$  HFETs

at drain bias  $V_{\text{ds}} = 5\text{ V}$  under different temperatures.

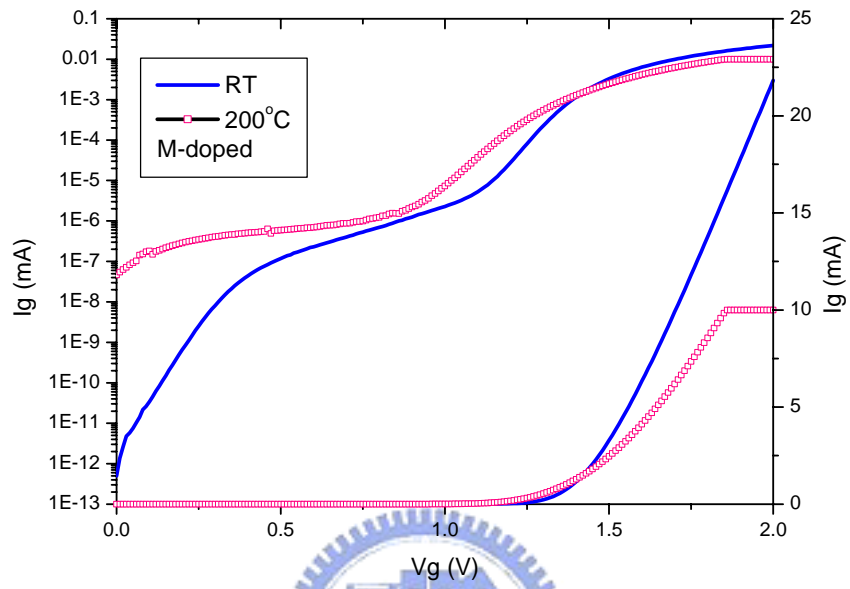


Fig. 7-9 Forward Schottky gate I-V characteristics of undoped  $\text{Al}_{0.3}\text{Ga}_{0.7}\text{N}/\text{GaN}$  HFETs at room temperature and 200°C.

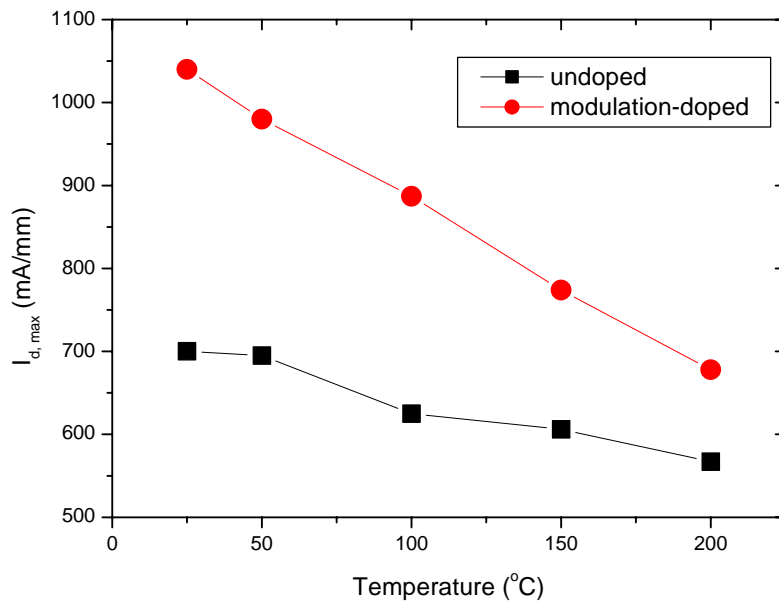


Fig. 7-10 A comparison on the temperature dependence of the maximum drain current,

$I_{d, \max}$  of the undoped and modulation-doped  $\text{Al}_{0.3}\text{Ga}_{0.7}\text{N}/\text{GaN}$  HFETs.

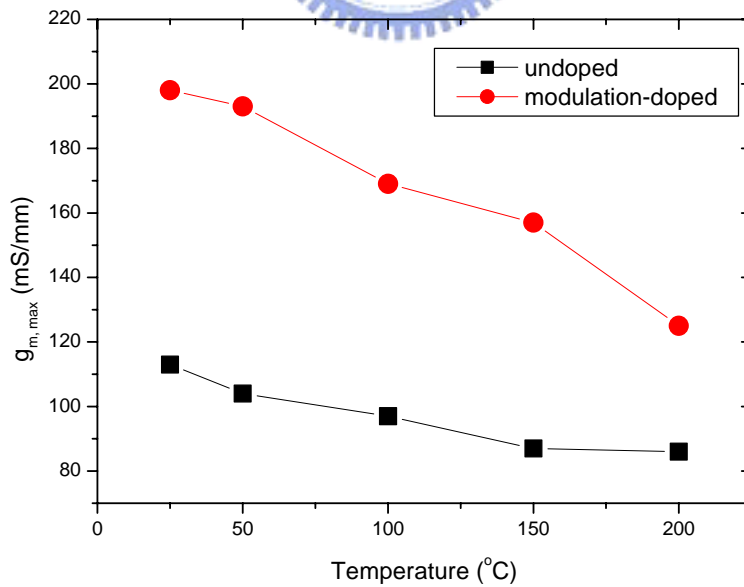


Fig. 7-11 A comparison on the temperature dependence of the maximum extrinsic

transconductance of the undoped and modulation-doped  $\text{Al}_{0.3}\text{Ga}_{0.7}\text{N}/\text{GaN}$  HFETs.

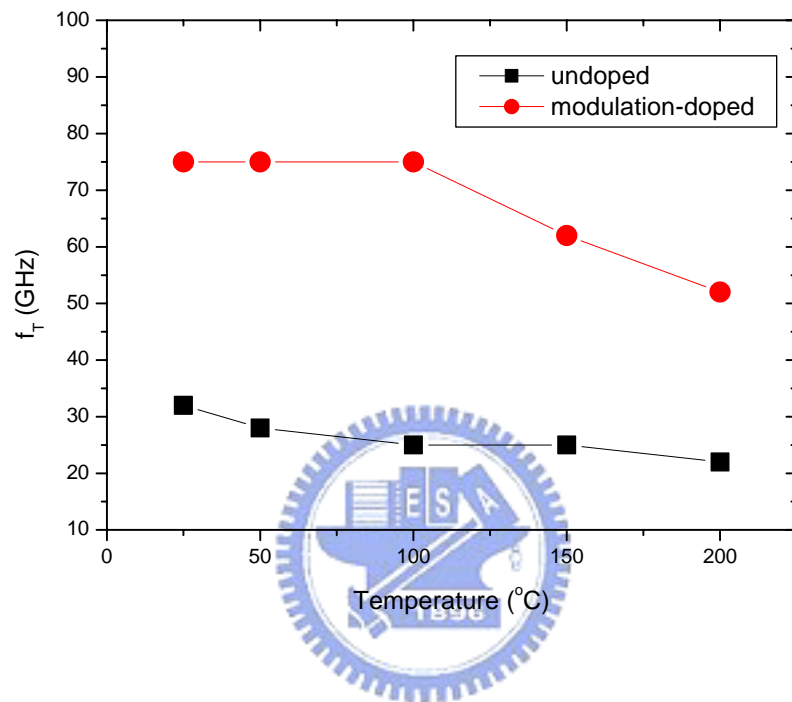


Fig. 7-12 A comparison on the temperature dependence of cut-off frequency ( $f_T$ ) of the undoped and modulation-doped  $\text{Al}_{0.3}\text{Ga}_{0.7}\text{N}/\text{GaN}$  HFETs.

## Chapter 8

### Conclusion and proposed future work

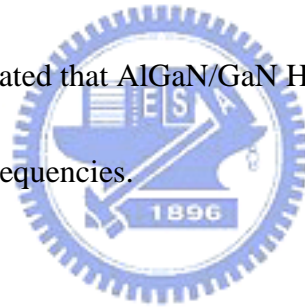
#### 8-1 Conclusion

We systematically investigated the AlGa<sub>N</sub>/Ga<sub>N</sub> HFETs. The research topics cover the development of basic device processing technologies and fundamental device issues. We successfully developed the technologies required for the fabrication of high-performance AlGa<sub>N</sub>/Ga<sub>N</sub> HFETs, including the ICP etching of Ga<sub>N</sub>, low resistance Ohmic contacts to n-Ga<sub>N</sub> and the narrow T-gate fabrication. A proper etching rate together with the vertical sidewall profile and smooth surface can be obtained in the ICP etching of Ga<sub>N</sub>. Plasma-treated Ohmic contacts exhibit low contact resistances and excellent thermal stability. With proper writing pattern design, narrow T-gates with the foot width of 40 nm were successfully obtained using a low accelerating voltage electron beam.

In addition, we studied the orientation effect, the polarization effect and the thermal effect of AlGa<sub>N</sub>/Ga<sub>N</sub> HFETs. For unpassivated devices, no obvious correlation was observed between the device orientation and the device characteristics. We experimentally demonstrated that the polarization effect plays a crucial role in both the electron transport properties and device characteristics of AlGa<sub>N</sub>/Ga<sub>N</sub> HFETs. The strong polarization effect in the undoped AlGa<sub>N</sub>/Ga<sub>N</sub> heterostructures leads to the formation of high-concentration 2DEG



at the AlGa<sub>0.3</sub>N/GaN interface and thus large output device current can be obtained. The thermal effect is particularly important for the high-temperature application of devices. We found that in addition to the commonly known problem in the thermal conductivity of substrate, the device structure also plays a significant role in the temperature-dependent electron transport properties and the device high temperature performance. Furthermore, we successfully fabricated high-performance submicron AlGa<sub>0.3</sub>N/GaN HFETs. Both the undoped and the modulation-doped Al<sub>0.3</sub>Ga<sub>0.7</sub>N/GaN HFETs exhibited very high output currents, high breakdown voltages and high cut-off frequencies. These excellent device characteristics obtained experimentally demonstrated that AlGa<sub>0.3</sub>N/GaN HFETs are indeed very excellent high power devices operating at high frequencies.



## **8-2 Proposed future work**

In this work, we have successfully developed the processing technologies required for device fabrication, studied device fundamental problems and fabricated the high-performance AlGa<sub>0.3</sub>N/GaN HFETs. Compared with the best device performance reported in the literatures, shown in Table 8-1 and 8-2 [1-8], there are still much that needs to be further improved.

First of all, the material quality of the AlGa<sub>0.3</sub>N/GaN heterostructures, especially in the cases of high Al content, needs to be improved. The material quality of the AlGa<sub>0.3</sub>N/GaN heterostructures plays a key role in realizing high-performance devices. The electron transport

properties obtained, especially the electron mobility, are still inferior to the highest value. This is a huge challenge in material growth.

Next, the trapping problem needs to be solved. The trapping effect is a very important issue since the surface traps lead to severe microwave output power degradation. Previous reports have shown that proper surface passivation can improve the surface trapping problem and the microwave power performance significantly [9].

In addition, the large-signal performances of devices need to be further characterized. The large-signal performance is an important figure of merit for microwave power transistors. In this work, device dc and small-signal characteristics were characterized. The large-signal performances such as the microwave power performance, the power-added efficiency and the large-signal gain have not been characterized yet.



## References

- [1] W. Lu, V. Kumer, R. Schwindt, E. Piner and I. Adesida, *IEEE Trans. Microwave Theory Tech.*, **50**, 2499 (2002).
- [2] V. Kumer, W. Lu, F. A. Khan, R. Schwindt, A. Kuliev, G. Simin, J. Yang, M. A. Khan and I. Adesida, *Electron. Lett.*, **38**, 252 (2002).
- [3] V. Kumer, W. Lu, F. A. Khan, R. Schwindt, A. Kuliev, J. Yang, M. A. Khan and I. Adesida, *IEDM Tech. Dig.*, 927 (2001).
- [4] V. Kumer, W. Lu, R. Schwindt, J. Van. Hove, P. Chow and I. Adesida, *Electron. Lett.*, **37**, 858 (2001).
- [5] J. A. Bardwell, Y. Liu, H. Tang, J. B. Webb, S. J. Rolfe and J. Lapointe, *Electron. Lett.*, **39**, 564 (2003).
- [6] V. Kumer, W. Lu, R. Schwindt, A. Kuliev, G. Simin, J. Yang, M. A. Khan and I. Adesida, *IEEE Electron Device Lett.*, **23**, 455 (2002).
- [7] W. Lu, J. Yang, M. A. Khan and I. Adesida, *IEEE Trans. Electron Devices*, **48**, 581 (2001).
- [8] M. Micovic, N. X. Nguyen, P. Janke, W. S. Wong, P. Hashimoto, L. M. McCray and C. Nguyen, *Electron. Lett.*, **36**, 358 (2000).
- [9] B. M. Green, K. K. Chu, E. M. Chumbes, J. A. Smart, J. R. Shealy and L. F. Eastman, *IEEE Electron Device Lett.*, **21**, 268 (2000).



Table 8-1 A comparison on the device performance of AlGaIn/GaN HFETs on sapphire substrates

	Ns Mobility	L <sub>g</sub> (um)	I <sub>d, max</sub> (mA/mm)	G <sub>m,ext</sub> (mS/mm)	f <sub>T</sub> (GHz)	f <sub>max</sub> (GHz)
2002 MTT [1]	1.3E13 1330	0.18	920	212	101	140
2002 EL [2]	1.2E13 1200	0.25	1400	401	85	151
2001 IEDM [3]	1.2E13 1200	0.15 recess	1310	402	107	148
2001 EL [4]	1.5E13 1170	0.25	1390	216	67	136
<b>Our best result</b>	<b>1.23E13 953</b>	<b>0.15</b>	<b>1060</b>	<b>200</b>	<b>75</b>	<b>90</b>

Table 8-2 A comparison on the device performance of AlGaIn/GaN HFETs on SiC substrates

	Ns Mobility	L <sub>g</sub> (um)	I <sub>d, max</sub> (mA/mm)	G <sub>m,ext</sub> (mS/mm)	f <sub>T</sub> (GHz)	f <sub>max</sub> (GHz)
2003 EL [5]	1.61E13 993	0.13	1250	250	103	170
2002 EDL [6]	1.1E13 1300	0.12	1230	314	121	162
2001 ED [7]	1.2E13 1200	0.12	1190	217	101	155
2000 EL [8]	1.1E13 1170	0.13	1200		110	140
<b>Our best result</b>	<b>1.23E13 953</b>	<b>0.15</b>	<b>1060</b>	<b>200</b>	<b>75</b>	<b>90</b>

## 簡 歷 (Vita)

姓名：李建騏 (Chien-Chi Lee)

性別：男

出生年月日：民國 60 年 1 月 23 日

籍貫：桃園縣

學歷：

大同大學 材料工程系學士 (78.9~82.6)

國立清華大學 材料科學及工程系碩士班 (82.9~85.6)

國立交通大學 電子研究所博士班 (88.9~93.6)



經歷：

中環公司 研發部工程師 (87.6~88.8)

博士論文題目：

氮化鎵異質結構場效電晶體

GaN-based heterostructure Field-Effect Transistors

## Publication List

- [1] **C. C. Lee**, M. H. Yeh, S. D. Lin, C. P. Lee, W. I. Lee and C. T. Kuo, “Thermal stability of plasma-treated Ohmic contacts to n-GaN.”, International Conference on Solid State Devices and Materials (SSDM), Nagoya, Japan, pp. 518-519 (2002).
- [2] **C. C. Lee**, S. D. Lin, C. P. Lee, M. H. Yeh, W. I. Lee and C. T. Kuo, “Thermal stability of plasma-treated Ohmic contacts to n-GaN.”, Jpn. J. Appl. Phys., **42**, pp. 2313-1315 (2003).
- [3] **C. C. Lee**, C. P. Lee, M. H. Yeh, W. I. Lee and C. T. Kuo, “Low resistance Ohmic contacts to n-GaN by Ar plasma and forming gas ambient treatments.”, J. Vac. Sci. Technol., **B21**, pp. 1501-1504 (2003).
- [4] **C. C. Lee**, C. F. Shih, C. P. Lee, R. C. Tu, C. C. Chou and J. Chi, “Temperature-dependent electron transport properties in AlGa<sub>N</sub>/Ga<sub>N</sub> heterostructures.”, Jpn. J. Appl. Phys., **43**, pp. L740 – L742, (2004).
- [5] **C. C. Lee**, C. P. Lee, and C. T. Kuo, “40 nm narrow T-gate fabrication on GaN.”, submitted to Microelectronic Engineering.
- [6] **C. C. Lee**, C. F. Shih, C. P. Lee, R. C. Tu, C. C. Chou and J. Chi, “Performance of AlGa<sub>N</sub>/Ga<sub>N</sub> heterostructure field effect transistors over temperatures.”, submitted to International Conference on Solid-State and Integrated-Circuit Technology (ICSICT 2004), Beijing, China.